Discrete Element Simulations on Granular Materials under Generalized Three-Dimensional Stress System

(個別要素法による一般的な 3 次元応力条件下での粒状体挙動に関する研究)

A dissertation submitted to the Graduate School of Science and Engineering, Saitama University to partial fulfillment of the requirements for the degree of Doctor of Philosophy majoring in Science and Engineering

by

Phusing Daraporn

(12DE057)

Supervisor

Prof. Suzuki, Kiichi

Graduate School of Science and Engineering

Saitama University, Japan

June, 2015

Acknowledgements

It is my pleasure to thank to my academic advisor, Prof. Kiichi Suzuki, for his advices. During the difficult time, his suggestions were not only useful for research study but also encouraged me to gain deeper and wider knowledge. In addition, I would love to give many thanks to my family for the warm support.

Besides, thanks to Japanese Government who kindly granted me Monbukagakusho scholarship (MEXT), I could finally attend Saitama University, the Graduate School of Science and Engineering (Ph.D. Program) from CY2012 to CY2015 in prder to be experienced academically until graduation.

At last, I would like to thank all of Professors, staffs, and friends at the Graduate School of Science and Engineering, Saitama University for some knowledge and good experiences in Japan.

Abstract

Most behaviors of granular materials have been studied under the limit conditions of stress paths, such as triaxial compression or extension tests where the intermediate principal stress σ_2 has not been involved. In reality, granular materials are under generalized stress system where the major, intermediate and minor principal stresses σ_1, σ_2 and σ_3 change continuously. The behavior of granular materials under generalized stress system is not well understood, particularly the relationships between the macro behavior and micro-scale response. Discrete Element Method (DEM), a numerical simulation, can simulate the macro behavior and explore the micromechanical behavior of granular materials. This study focused on the influence of intermediate stress ratio, specified by the *b* value [= $(\sigma_2-\sigma_3)/(\sigma_1-\sigma_3)$], on the mechanical behavior of granular materials under generalized stress system. There are three objectives of this research. The first is to simulate the macro behaviors and explore the micro characteristics of three-dimensional granular materials under continuously varying *b* value stress paths. The second one is to explain the relationship among the macro behaviors and microstructure parameters and load transmission in granular materials under continuously varying *b* value stress paths. And the third one is to describe the experimental phenomena of monotonic and cyclic loading tests on sand by using the micro variables. To this end, monotonic and cyclic loading under truly triaxial conditions, following the stress controlled method on 8,000 spheres, were simulated with continuously varying *b* value.

For this research, it is found that DEM shows qualitative results of the macro behaviors of experiments of sand under monotonic as well as cyclic loading under continuously varying *b* value stress paths. The macro behavior and micro response data were described by the relationship between the stress ratio and fabric structures representing contacts of all particles as well as the strong contact regardless of the varying *b* value. Moreover, this study found that changing the *b* values continuously shows different distributions of the fabric and contact forces evolutions. The increments of anisotropy coefficients of average fabric, normal contact forces, and tangential contact forces differ depending on the *b* value. Furthermore, the

continuously varying *b* value stress paths lead to change the increment directions of the stresses which cause some changes in the increment directions of those anisotropy coefficients. However, the differences in the directions of stress paths do not affect those anisotropy coefficients at the peak stress. Finally, the stress-force-fabric relationships under continuously varying *b* value stress paths were presented in terms of the anisotropy coefficients of fabric, normal contact forces, and tangential contact forces anisotropic. Regarding cyclic simulations, a qualitative comparison of the stress-strain-dilation between the DEM and experimental results under triaxial cyclic loading shows similarity tendency. Furthermore, micromechanical responses, indicated by coordination number and sliding contact fraction, can be used to explain the macro behavior in cyclic loading. Additionally, the macro-micro relationship is explained by using the relationship between stress ratio and fabric structures of all contacts, and only the strong ones. The study found that the unique macro-micro relationship does not depend on the more generalized cyclic stress path and the number of cycles.

Table of Contents

List of Tables

List of Figures

Chapter 1 : Introduction

1.1 Background

Granular materials like sand are made up of discrete particles without any cohesive forces between the particles. When a load is applied, the resulting forces are absorbed by the substrate. As a result of the applied load, the sand is compacted and micro contacts between particles occur, forcing them to change their orientations. The void between particles has changed continuously involving the particles orientation. The discontinuity between contacts also happens within granular materials. Consequently, the macro behavior changes. Many previous researches have studied the macro behavior and micromechanical response of granular materials under several conditions by experiments and numerical simulations. However, in general stress system where the major, intermediate and minor principal stresses σ_1, σ_2 and σ_3 change continuously, there are still many phenomenological and physical behaviors of granular materials which have not been clearly explained.

Several concepts of mathematical modelling have been established using the continuum subject in order to model the behavior of granular materials. Different concepts need different input parameters to approach the physical behavior of sand which are sometimes difficult for model users and developers. The validation of each modelling is normally done by comparing the results of the model and results of the laboratory testing. It is important for the geotechnical engineering to validate the existing models as well as to generate the new continuum approach.

Because sand is discrete by nature, numerical simulation for discrete particles is widely used to study the behavior of real sand. The behavior of granular material is mainly considered in macroscopic and micromechanical response. In order to clearly understand the macro behavior of granular materials, geotechnical engineers need to understand its behavior in the micro level. The relationship among the externally applied load, the macro response of the granular system, the microstructure or fabric, as well as the distribution of the contact force have been distributed a

qualitative considerate of the mechanism of load transfer in granular materials(e.g. Dantu 1957; De Josselin de Jong 1969; Oda et al. 1978; Oda and Konishi 1974). It is necessary to initiate the innovative continuum mechanic of granular behavior. More recently, the computer simulation has been used to model the granular assemblies of 2-dimentional discs under shearing and obtain some qualitative details of the microscopic feature (e.g. Cundall and Strack 1979, 1983; Rothenburg and Bathurst 1989, 1992; Thornton 2000; Thornton and Barnes 1986). Many years later, 3-dimentional simulation has been widely used because of the importance of simulation the real sand more closely (Bathurst 1985; Phusing et al. 2015; Sazzad et al. 2012; Sitharam et al. 2004). However, most behaviors of granular materials have been studied under the limit conditions of stress paths, such as triaxial compression or extension tests where the intermediate principal stress σ_2 has not been involved. In fact, granular materials are under generalized stress system where the major, intermediate and minor principal stresses σ_1, σ_2 and σ_3 change continuously. The behavior of granular materials under generalized stress system is not understandably described, particularly the relationships between the macro behavior and micro-scale response.

Discrete Element Method (DEM) is one of the numerical approach for studying the mechanical behavior of granular materials, the representative of sand. DEM is a numerical simulation tool, created by Cundall and Strack (1979). DEM has been widely used for simulating granular materials and investigating the mechanical behavior of granular materials (Thornton 2000; Ng 2004a; Ng 2004b; Sazzad et al., 2011; Barreto and O'Sullivan 2012).

This research focuses on using DEM simulating the macro behaviors and explore the micro characteristics of three-dimensional granular materials under more generalized stress systems. Furthermore, the microscopic data has been explored and explained the relationship between macro and micromechanical behavior for monotonic as well as cyclic loading of generalized stress systems. For monotonic loading simulation, the relationship among applied stress, contact forces between particles, and fabric distribution from DEM has been studied using the stress-force-fabric relationship developed by Rothenburg (1980). The validation of the existing stress-force-fabric relationship under the more generalized stress systems in this study has not been mentioned.

1.2 Objectives

Regarding the motivation mentioned in the background, there are three main objectives of this research.

i. To simulate the macro behaviors and explore the micro characteristics of three-dimensional granular materials under continuously varying *b* value stress paths.

ii. To explain the relationship between macro behaviors and microstructure parameters and load transmission in granular materials under continuously varying *b* value stress paths.

iii. To describe the experimental phenomena of monotonic and cyclic loading tests on sand by using the micro variables.

1.3 Organization of the dissertation

The organization of the dissertation is ordered as follow:

Chapter 1 describes the background/motivation, objectives and organization of this dissertation.

Chapter 2 explains the related literatures in experimental and DEM based studies, as well as the fundamental microscopic concepts.

Chapter 3 reviews the fundamental theory of DEM and some brief details of computer program OVAL.

Chapter 4 describes the macro-micro behaviors of granular materials under continuously varying *b* value. The preparation of the sample using spherical particles is explained. Macro behaviors and micro data of the sample under several constant *b* and continuously varying *b* stress paths are described. The relationship between macro-

and micro- behaviors of granular materials under continuously varying *b* value is presented.

Chapter 5 explains the evolution of microstructure parameters at the particle levels, as well as verification of fundamental microscopic description in chapter 2. The granular sample is simulated under continuously varying *b* value stress paths and this research explores the micro variables data. Microstructure parameters are found and used to plot the distribution diagrams of fabric tensors and contact forces at the particle level. The stress-strain curves using the stress-force-fabric relationship (Rothenburg 1980) is established and compared with the stress-strain curves from DEM results.

Chapter 6 explains the macro-micro behaviors of granular materials under cyclic loadings. The sample preparation is described corresponding to the experiment of Nakai et al. (2003) testing cemented-sand under several cyclic loadings in general stress systems. The stress-strain-dilation curves of compression and extension cyclic loading of DEM and the experiment are compared and discussed. The strain increment vectors of DEM and the experiment are shown. The micro data during cyclic loadings are explained.

Chapter 7 summarizes the major conclusions from the overall research and gives some recommendations for further studies.

Chapter 2 Literature Review

2.1 Introduction

The behavior of granular materials can be influenced by several factors. Literature has been researched and reported those influenced ones. Experimental methods and numerical simulation were used widely in geotechnical engineering to show great effects of these factors. In this study, the factors have influences on the macro behaviors and micromechanical response consists of the intermediated stress ratio *b* value, sample density, and interparticle friction angle. The other factors such as confining pressure, particle shape, inherent anisotropy, are strictly controlled. The fundamental of macro-micro relationship called stress-force-fabric relationship (Rothenburg 1980) is described in this chapter.

2.2 The Influential Factors on Macro Behaviors and Microscopic of Granular Materials

2.2.1 The intermediated stress ratio *b* value

The intermediated stress ratio *b* value shows in Eq. 2.1. Fig. 2.1 shows the principal stresses under triaxial loading. The intermediate principal stress σ_2 can significantly affect the stress-strain behavior of granular materials. A non-dimensional parameter *b* [= $(\sigma_2-\sigma_3)/(\sigma_1-\sigma_3)$] was introduced by Habib (1953) as a stress ratio to describe the influence of σ_2. Several experiments have been conducted to study the influence of σ_2 on the behavior of sand under different stress paths, with a constant *b* value (e.g., Lade and Duncan 1973; Matsuoka and Sun 1995; Lade 2006; Suzuki and Yanagisawa 2006; Sun et al., 2008; Kumruzzaman and Yin 2012; Rodriguez and Lade 2013). Most of these experiments examined the relationship between the *b* value and

the angle of shearing resistance ϕ [= $\sin^{-1}((\sigma_1-\sigma_3)/(\sigma_1+\sigma_3))$] at peak strength. For instance, Ko and Scott (1968) and Yamada and Ishihara (1979) reported that ϕ increases from b = 0 to a certain value (nearly b = 0.5) and then decreases slowly when approaching unity. Similar result was reported recently by Kumruzzaman and Yin (2012) as well as Rodriguez and Lade (2013). However, Green and Bishop (1969) and Lade and Duncan (1973) reported differently. According to their studies, after certain values of b (nearly b = 0.2), ϕ remains almost constant or decreases or even increases with increasing b, before it decreases when approaching unity. Matsuoka and Nakai (1974) reported differently. According to their study, after certain values of b (nearly b = 0.3), ϕ decreases with the increasing b value until b = 1. Also, Lade (2006) concluded that most experimental results on sand show that ϕ increases from b = 0, depending on particular types of sand. Different relationships between ϕ and b indicate that type of sand, sample preparation and loading conditions may influence these relations.

$$b = \frac{\sigma_{intermediate} - \sigma_{min}}{\sigma_{max} - \sigma_{min}} \tag{2.1}$$

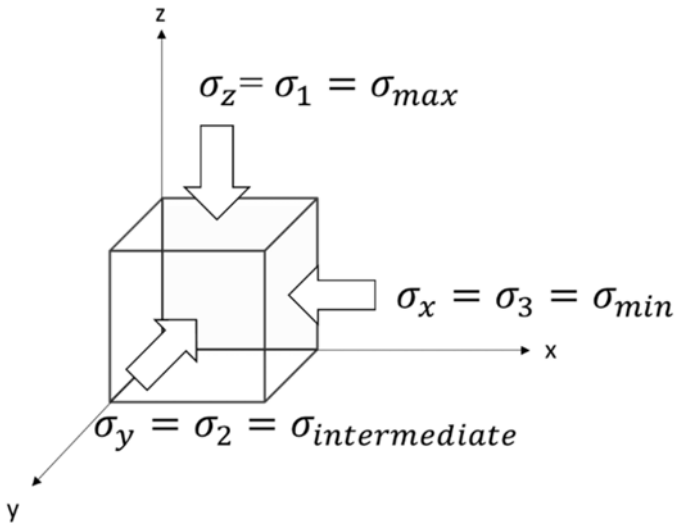

Fig. 2.1 Principal stresses under triaxial loading

Discrete Element Method (DEM) has been used to simulate granular materials and investigate the mechanical behavior of granular materials (Thornton 2000; Ng 2004a; Ng 2004b; Sazzad et al., 2011; Barreto and O'Sullivan 2012). Sand behavior of at the micro level in response to an applied load, including changing inter-particle friction angles and different b values, has been studied before. For example, Thornton (2000) used some disc particles to examine the effect of intermediate principle stress under constant mean stress condition, using Lade and Duncan's (1975) failure model. Ng (2004a) who used oval particles, reported the effect of intermediated principal stress and stress-strain behavior under constant b tests using the DEM. It was noted that the angle of shearing resistance ϕ from the DEM results supports the models of Lade (1977) and Ogawa et al. (1974) much more than the models of Stake (1975) and Matsuoka and Nakai (1978). Furthermore, Ng (2005) studied the effects of different densities under different stress paths of constant b test and concluded that the density of samples has no great influence on the relationship between ϕ and b. In the other study, Sazzad et al. (2011) used spherical particles of DEM to simulate the macro mechanical responses and explore the micro characteristics of granular materials under constant b tests. The relationship between ϕ and b by Sazzad et al. (2011) was similar to that of the experiment of Ko and Scott (1968). According to Sazzad et al. (2011), the evolution of the principal deviatoric strains, directions of stress increment vector and strain increment vector as well as dilatency from the DEM results at least shows good qualitatively consistency with the experimental observations. Comparing DEM simulations using spherical particles and experimental data, Barreto and O'Sullivan (2012) demonstrated that the b value can significantly influence the coefficient of inter-particle friction μ.

The previous literature shows that DEM simulations have generally been conducted with a constant b value. In fact, however, the stress path changes its direction continuously in the stress space, which causes some change in the b value. Experimentally, the relationship between a strain increment and stress increment direction, under more generalized stress paths, has been performed (Matsuoka and Sun 1995; Nakai et al., 2003). However, based on the author's assumption, DEM simulations of granular materials under a continuously varying b value have not been deeply explained yet.

In this study, the definition of the *b* value has been modified in order to follow the condition of continuously varying *b* value. The *b* value in this study is greater than 1 located in the area $1 \leq b \leq \infty$ as in Fig. 2.2(a). In Fig. 2.2(a) shows the stress path *b*=0, *b*=1 and *b*= ∞ corresponding to the diagram of stresses Figs. 2.2(b), 2.2(c), and 2.2(d). For example, Fig. 2.2(b) shows that the increment of σ_z is two times over the increment of σ_x and σ_y. The result of this diagram shows that *b*=0. Similar explanation is for *b*=1 and *b*= ∞ in Figs. 2.2(c), and 2.2(d). This method has been used in Phusing et al. (2015) and Phusing and Suzuki (2015)

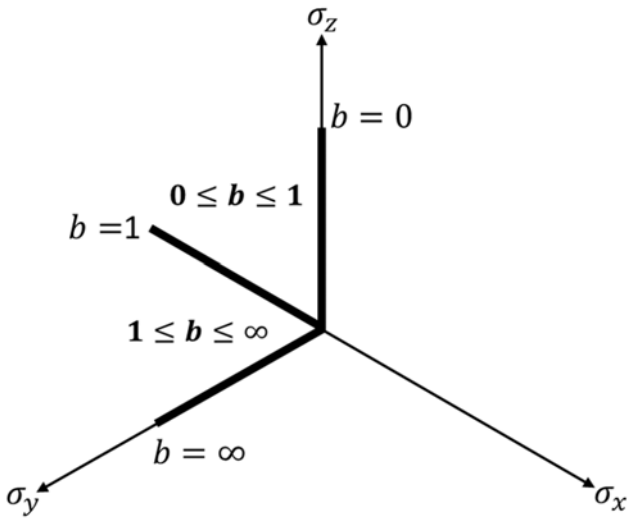

(a) Stress paths *b* = 0, *b* = 1, and *b* = ∞

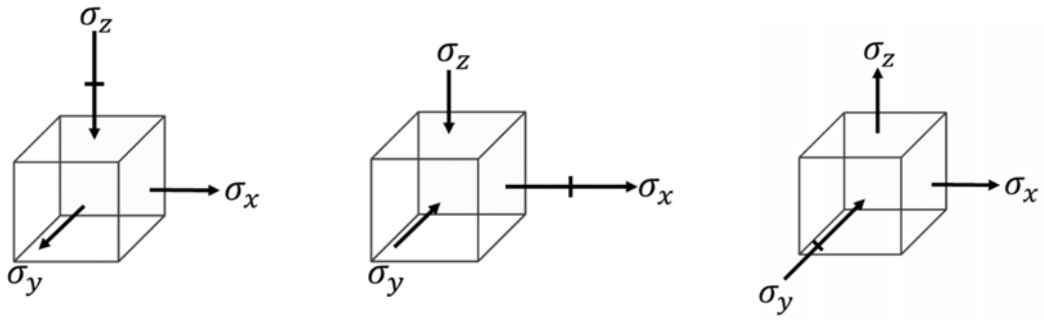

(b) *b* = 0 (c) *b* = 1 (d) *b* = ∞

Fig. 2.2 Stress paths and diagrams of *b* = 0, *b* = 1, and *b* = ∞

2.2.2 Sample Density

Sample density is one of the most factors affecting the behavior of sample while shearing. Granular materials have different density depending on stress-strain-dilation. The void ratio e, the porosity η and the relative density $D_r[= \frac{e_{max}-e}{e_{max}-e_{min}} = \frac{(\eta_{max}-n)(1-\eta_{min})}{(\eta_{max}-\eta_{min})(1-\eta)}]$ can be used to classify the density of granular sample where e_{max} , η_{max} , e_{min}, η_{min} are maximum and minimum void ratio and porosity. Experiments show that increasing the strain increases the deviatoric stress up to the peak and reduces to strain softening when sample is dense. However, the loose samples show some continuous increases in deviatoric stress but increasing the strain. These results were conducted the dense and loose sand under drained monotonic condition (Ergun 1981; Roscoe et al. 1958; Wang and Lade 2001). If considering numerical results using DEM, the influence of relative density is one important factor affecting the macro and micromechanical behavior of granular materials (Thornton 2000; Salot et al. 2009; Madhusudhan and Kumar 2010; Sazzad and Suzuki 2013). For instance, Sazzad and Suzuki (2013) conducted three-dimensional spherical granular materials of loose and dense samples under constant *b* value. Their results shows that behaviors of stress-strain-dilation in both loose and dense samples are the same as those reported in the experiments qualitatively, similar to Thornton (2000) and Sitharam et al. (2004) and Salot et al. (2009). Moreover, Salot et al. (2009) studied the influence of relative density on the macro and micromechanical response. The macro behavior is the porosity as well as the stress-strain curves whereas the micro data is the coordination number. It was reported that the maximum relative density sample shows minimum porosity whereas the minimum relative density sample shows maximum porosity when deviatoric stress increases. Finally, the curve merges together at the large strain. However, the coordination number of the maximum relative density sample shows the highest value where the minimum shows the lowest. This result explains the characteristic of dense and loose sand, similarity to Thornton (2000), Sitharam et al. (2004) and Sazzad and Suzuki (2013). In this study, the simulation of dense sample is used in the monotonic loading tests but the medium

dense is used for cyclic loading tests. The density was chosen based on the experimental references in each loading tests.

2.2.3 Interparticle Friction

Interparticle friction is a significant factor influencing the behavior of granular materials. Granular assemblies cannot resist the external forces without internal friction between particles. Since the interparticle friction is encountered the difficult examination of measuring the reliable value, only few researches have been conducted (Skinner 1969; Procter and Barton 1974; Konishi et al. 1983). An example of experiments by Skinner (1969) studied the influence of interparticle friction on the behavior of spherical particles explaining that when increasing the interparticle friction, the effective angle of shearing resistance does not increase uniformly at peak or even at constant volume states. The other experiment by Konishi et al. (1983) observed the physical behaviors of photoelastic oval shaped rods and the interparticle friction angle. It was summarized that the interparticle friction angle increases at peak friction angle. In term of the literature using DEM, more studies have been done on interparticle friction because of the easy access to the micro level data when numerical simulation was used (e. g., Oger et al. 1998; Thornton 2000; Kruyt and Rothenburg 2006; Sazzad and Suzuki 2011; Barreto and O'Sullivan 2012). For example, Barreto and O'Sullivan (2012) reported the independent between the influence of the interparticle friction and intermediate stress ratio on the behavior of granular materials. Regarding the micromechanical data, Barreto and O'Sullivan (2012) reported that strong force chains produce similar direction with the major principal stress orientation. To conclude, the interparticle friction and the intermediate stress ratio affected the macro- and micro-scale response. Sazzad and Suzuki (2011) using oval-shaped particles with DEM, conducted some different interparticle friction angles under cyclic loading tests. They reported that the width of stress-strain cyclic loops develops narrowly the interparticle friction angle increases. Additionally, the single relationship between macro once and microscopic data has been shown only in strong contacts under cyclic loading.

2. 3 Fundamental Microscopic Description

Granular materials are discrete particles whereas the interaction between particles are interparticle contacts between them. The interacting contacts are generated a contact forces network at the particle level. They respond corresponding the external load at the boundary of the assembly. Good understanding of the micromechanical behavior help geotechnical engineers to have deeper some knowledge on the macroscopic behavior which can be used to develop existing simulation concept or initiate a new one. The fundamental microscopic description in this study has been described as follows.

2.3.1 Micromechanical Data

One of the objectives of the study is to correlate the macro behavior with the micro response. The micro data is represented by the evolution of coordination number (Kuhn 1999; Rothenburg and Kruyt 2004) and the modified sliding contact fraction (Sazzad 2011). Both referred in those literature are defined as follows:

$$\text{Coordination number} = \frac{2 \times Nc}{Np} \tag{2.2}$$

$$\text{Sliding contact fraction (\%)} = \frac{N_s}{N_c} \times 100 \text{ (\%)} \tag{2.3}$$

where N_c , N_p and N_s are the number of contacts, particles, and sliding contacts. This study explored the evolution of coordination number and sliding contact fraction of granular materials under monotonic loadings using spherical dense sample in Chapter 4 and cyclic loadings using medium dense sample in Chapter 6.

2.3.2 Fundamental of Macro-Micro Relationship

The relationship between the macro behavior and micromechanical data with various stress amplitudes in generalized stress system is one of the objectives in this study. The studies on the macro-micro relationship were conducted by several approaches. Thornton and Antony (1998), using 2-dimentional simulation, reported the compression and extension simulations on a soft particle system and found that shear strength was mainly due to strong force network and that the weak network's contribution to shear strength was very small. As well as Ng (2004b), the experiment showed that the principal stress ratio σ_1/σ_3 correlates with the contact normal force more than with the unit contact normal force under different stress paths. In this study, the correlation between the macro-scale, represented by the stress ratio *q/p*, and a single parameter, related to the contact normal vector, is used to describe the macro-micro relationship (Antony et al. 2004; Sazzad et al. 2011). The contact normal vectors are represented by all contacts in major, intermediate, and minor directions (F_{11}, F_{22}, and F_{33}, respectively) and by the strong contacts ($F_{11}^s, F_{22}^s,$ and F_{33}^s, respectively). The unit normal vector for all contacts is described by Satake (1982) as follows:

$$F_{ij} = \frac{1}{N_c}\sum_{k=1}^{N_c} n_i^k n_j^k, \qquad i = j = 1,2,3 \tag{2.4}$$

where N_c is the number of contacts, n_i^k is the component of the unit vector n^k at a contact. The unit normal vector for the strong contacts is described by Kuhn (2006) as follows:

$$F_{ij}^s = \frac{1}{N_c}\sum_{s=1}^{N_c^s} n_i^s n_j^s, \qquad i = j = 1,2,3 \tag{2.5}$$

where N_c^s is the number of strong contacts, n_i^s is the component of unit vector n^s at a strong contact. If the normal contact force is greater than the average contact normal force f_{ave}^n, it can be defined as a strong contact. The average normal contact force is as follows:

$$f_{ave}^{n} = \frac{1}{N_c}\sum_{i=1}^{N_c} f_i^{n} \tag{2.6}$$

where $f_i^n$is a normal contact force.

The deviatoric fabrics ratio of all contacts F_d/F_m and of strong contacts F_d^s/F_m^s, respectively. F_d and F_d^s are the equivalent deviatoric fabrics of all contacts and of strong contacts. F_{m} and F_m^s are the mean fabrics of all contacts and of strong contacts. F_d, F_d^s, F_{m}, and F_m^s are explained as follow:

$$F_d = \sqrt{\frac{1}{2}((F_{11}-F_{22})^2 + (F_{11}-F_{33})^2 + (F_{22}-F_{33})^2)} \tag{2.7}$$

$$F_m = (F_{11} + F_{22} + F_{33})/3 \tag{2.8}$$

$$F_d^s = \sqrt{\frac{13}{2}((F_{11}^s-F_{22}^s)^2 + (F_{11}^s-F_{33}^s)^2 + (F_{22}^s-F_{33}^s)^2)} \tag{2.9}$$

$$F_m^s = (F_{11}^s + F_{22}^s + F_{33}^s)/3 \tag{2.10}$$

2.3.3 Stress-Force-Fabric Relationship and Anisotropic Parameters

The relationship in balancing between applied stresses and internal forces is the stress-force-fabric relationship proposed by Rothenburg (1980) and Rothenburg & Bathurst (1989). Details are described here. More details are referred to read Rothenburg (1980). This relationship describes the macroscopic stress σ_{ij} equal to statistical averages of fabric and inter-partical load connection as:

$$\sigma_{ij} = \frac{1}{V}\sum_{c\in V} f_i^c l_i^c \qquad i,j = 1,2,3 \tag{2.11}$$

Eq. (2.11) relates a sum with respect to all contact forces within a volume of the assembly V, with cartesian components contact force f_i^c multiplied by components of contact vector l_i^c. The superscript c indicates the set of contacts within assembly V. In order to understand the inter-partical load connection in granular materials, the discrete amount in Eq. (2.11) can be substituted by the distribution function using a spherical harmonics expansion $E(\Omega)$(see Eq. 2.14). The factor using in the spherical harmonics expansion is expressed in terms of some tensors as described by Rothenburg (1980):

$$\sigma_{ij} = m_v \bar{l}_0 \int_\Omega \bar{f}_i^c(\Omega) n_j E(\Omega) d\Omega \tag{2.12}$$

where σ_{ij} is the macroscopic stress in terms of microstructural parameters, m_v is the contact density which equals the total number of contacts (twice number of physical contacts) per unit volume of the assembly V, $\bar{l}_0$ is an average of all contact vector lengths, $\bar{f}_i^c$ is an average normal contact vector in the cartesian direction n_j . In Eq. (2.12), the macroscopic stress can be referred to as the stress–force–fabric relationship. Chantawarangul (1993) has defined in detail of Eq. (2.12) and expressed the Eq. as follow:

$$\sigma_{ij} = \frac{m_v \bar{f}_0^n \bar{l}_0}{3}\left\{\delta_{ij} + \frac{2}{5}\left(a_{ij}^r + a_{ij}^n + \frac{3}{2}a_{ij}^t\right) + \frac{2}{35}\left[(a_{kl}^n - a_{kl}^t)a_{kl}^r\delta_{ij} + (4a_{il}^n + 3a_{il}^t)a_{ij}^r\right]\right\} \tag{2.13}$$

where δ_{ij} is the Kronecker delta, $\bar{f}_0^n$ is the average normal contact forces in the assembly, a_{ij}^r is the symmetric second-order deviatoric tensor representing the contact normal anisotropy coefficient (fabric anisotropy coefficient) , a_{ij}^n is the symmetric second-order deviatoric tensor representing the normal contact force anisotropy coefficient, and a_{ij}^t is the symmetric second-order deviatoric tensor representing the tangential contact force anisotropy coefficient. Sitharam (2000) explained on Eq. (2.13) that the carrying capacity of a granular materials at the hydrostatic stress is mainly due to the contact density m_v and to the average normal contact force $\bar{f}_0^n$, while the carrying capacity under the deviatoric stress is due to the ability to develop anisotropy in contact normal orientations and contact forces. In Eq. (2.11), the contact normal

distribution is approximated with a spherical harmonic expansion then simplified to be the second-order tensors as follows:

$$E(\Omega) = \frac{1}{4\pi}\left[1 + a_{ij}^{r}\, n_i^c n_j^c\right] \tag{2.14}$$

The a_{ij}^{r} can be described as follow:

$$a_{ij}^{r} = \frac{15}{2} R'_{ij} \tag{2.15}$$

where

$$R'_{ij} = R_{ij} - \frac{R_{kk}}{2}\delta_{ij} \tag{2.16}$$

and

$$R_{ij} = \int_{\Omega} E(\Omega) n_i^c n_j^c d\Omega \tag{2.17}$$

The distributed shape of the average of normal contact forces can be approximated by the equation similar to the fabric distribution (Rothenburg 1980) which is:

$$\bar{f}^n(\Omega) = \bar{f}_0^n\left[1 + a_{ij}^n n_i n_j\right] \tag{2.18}$$

The a_{ij}^n can be described as follow:

$$a_{ij}^n = \frac{15}{2}\frac{F'^n_{ij}}{\bar{f}_0^n} \tag{2.19}$$

where

$$F_{ij}^n = \frac{1}{4\pi}\int_{\Omega} \bar{f}^n(\Omega)\, n_i n_j d\Omega \tag{2.20}$$

and

$$\bar{f}_0^n = \frac{1}{4\pi}\int_{\Omega} \bar{f}^n(\Omega)\, d\Omega \tag{2.21}$$

The distribution of the average of tangential contact forces is represented as follows:

$$\bar{f}_i^t(\Omega) = \bar{f}_0^n\left[a_{ij}^t n_j - (a_{kl}^t n_k n_i) n_i\right] \quad \text{and} \quad \bar{f}^t(\Omega) = \left(\bar{f}_i^t \bar{f}_i^t\right)^{1/2} \tag{2.22}$$

The a_{ij}^t can be described as follow:

$$a_{ij}^t = \frac{15}{3}\frac{F_{ij}^t}{\bar{f}_0^n} \tag{2.23}$$

where

$$F_{ij}^t = \frac{1}{4\pi}\int_\Omega \bar{f}_i^t(\Omega)\, n_j d\Omega \tag{2.24}$$

As for the microscopic coefficient anisotropy tensors, (a_{ij}^r, a_{ij}^n and a_{ij}^t) are produced from their invariants in the same way as the stress tensor (Bathurst 1985; Chantawarangul 1993; Sitaram 2000):

$$a^r = \sqrt{\frac{3}{2}a_{ij}^r a_{ij}^r},\ a^n = \sqrt{\frac{3}{2}a_{ij}^n a_{ij}^n},\ \text{and}\ a^t = \sqrt{\frac{3}{2}a_{ij}^t a_{ij}^t} \tag{2.25}$$

Chapter 3 Discrete Element Method and Program OVAL

3.1 Introduction

In order to understand the complex behavior of granular materials, the macro responses and the microstructure characteristics have to be described during the deformation evolution. Experimental tests are difficult to measure the internal stresses at the gain level. They may be estimated from the boundary conditions. The numerical technique is possibly a powerful method to model the behavior of granular materials. Since the numerical method can monitor physical inside data at any state of each discrete particles in granular systems during deformation, the numerical technique is possibly a powerful method to model the behavior of granular materials. Moreover, the numerical method is flexible because it can adjust input parameters regarding in what we are interested such as load conditions, particle sizes, particle shapes, and the particles distribution. Considering the available numerical method including all flexibilities, Discrete Element Method (DEM) by Cundall and Strack (1979) has been designed to model the macro behaviors and provide micro responses. A DEM program code named OVAL (Kuhn 2006) was created to simulate the macro behaviors and explore the micro characteristics of two- and three-dimensional granular materials. This study used OVAL code of three-dimensional spherical granular materials with periodic boundary. The following sections in this chapter explain in brief the fundamental of DEM and OVAL program.

3.2 Discrete Element Method (DEM)

In the Discrete Element Method (DEM) by Cundall and Strack (1979), the equilibrium contact forces and displacements of granular systems are discovered by a series of calculation following the movements of each particle by calculating Newton's law of motion. Particles are able to overlap

each other despite the rigid property. Even though the DEM calculation is the dynamic problems, particles are monitored closely in close to static equilibrium by controlling the deformation of assemblies to be as slow as possible. Furthermore, DEM can be used to implement a large number of particles under various stresses and interparticle interaction conditions which provide some different deformations of macro behaviors and microscopic responses.

3.2.1 DEM Calculation Cycle

In DEM, each particle is modeled to follow Newton's second law of motion and the force of displacement law in each time step. The results of law of motion give translational and rotational accelerations of particles. Then, these accelerations are integrated to obtain the velocities of particles. After that, the velocities are integrated to obtain the displacements of the particles. Then, the force-displacement is used in the contact displacement law to obtain the new contact forces which uses to be applied to the particles in the next time step and the cycle is repeated. The cycle is explained in Fig. 3.1. More details of DEM are referred in Cundall and Strack (1979). The short description is explained in next section.

3.2.2 Law of Motion Implementation

Fig. 3.2 shows two spherical particles A and B in contact. *n*, *t* and *s* are unit contacts in one normal and two tangential vectors respectively. r^A and r^B are the distance between the center of sphere A and B and the contact point. l^{AB} is the distance between the center of sphere A and B or branch vector. $\dot{\theta}^A$ and $\dot{\theta}^B$ are rotational velocities of spheres A and B.

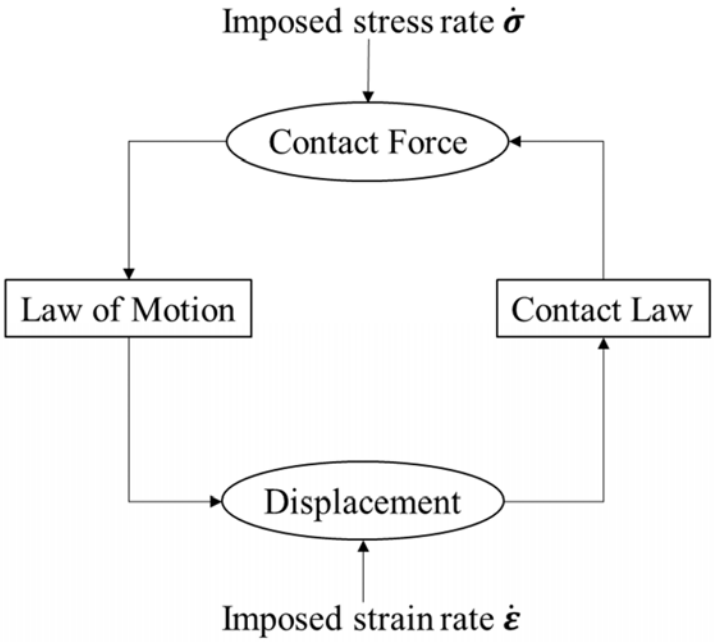

Fig. 3.1 Calculation cycle in DEM

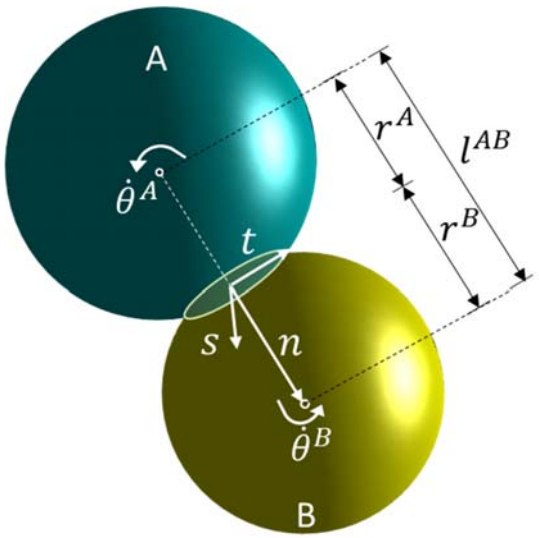

Fig. 3.2 Two contacting spheres and contact vectors

The translational and rotational accelerations of particle A are defined by the following incremented expressions:

$$m^A \ddot{x}_i^A = \sum F_i^A \quad i = 1,2,3 \tag{3.1}$$

$$I\ddot{\theta}^A = \sum M^A \tag{3.2}$$

where m^A is mass of particle A. $\ddot{x}_i^A$ and $\ddot{\theta}^A$ are the components of translational accelerations and rotational accelerations respectively. F_i^A is the components of forces acting on particle A, I is the moment of inertia and $M^A$is the moment on particle A. The velocity of particle A $\dot{\theta}^A$ can be solved by making the component of translational accelerations $\ddot{x}_i^A$ and rotational accelerations $\ddot{\theta}^A$ constant over a time interval Δt from $t - \frac{\Delta t}{2}$ to $t + \frac{\Delta t}{2}$ using the finite-difference procedure as shown in Eq. 3.3 and 3.4. Then, the velocities are integrated to obtain the displacement consisting of location and rotation of the particle at the end of time step $t + \frac{\Delta t}{2}$, using Eq. 3.5 and 3.6.

$$\dot{x}_i^A{}_{(t+\frac{\Delta t}{2})} = \dot{x}_i^A{}_{(t-\frac{\Delta t}{2})} + \frac{\left(\sum F_i^A\right)_{(t)} \times \Delta \mathrm{t}}{m^A} \tag{3.3}$$

$$\dot{\theta}^A{}_{(t+\frac{\Delta t}{2})} = \dot{\theta}^A{}_{(t-\frac{\Delta t}{2})} + \frac{(\sum M^A)_{(t)} \times \Delta \mathrm{t}}{I^A} \tag{3.4}$$

$$x_i^A{}_{(t+\frac{\Delta t}{2})} = x_i^A{}_{(t-\frac{\Delta t}{2})} + \dot{x}_i^A{}_{(t+\frac{\Delta t}{2})} \times \Delta \mathrm{t} \tag{3.5}$$

$$\theta^A{}_{(t+\frac{\Delta t}{2})} = \theta^A{}_{(t-\frac{\Delta t}{2})} + \dot{\theta}^A{}_{(t+\frac{\Delta t}{2})} \times \Delta \mathrm{t} \tag{3.6}$$

3.2.3 Force Displacement Law

The translational and rotational acceleration are integrated to obtain translational and rotational velocities of particle A $\dot{x}_i^A$, $\dot{\theta}^A$ and particle B $\dot{x}_i^B$, $\dot{\theta}^B$ (see Fig. 3.2 and Eq. 3.3 and 3.4). Then, the contact displacement is used to calculate following the finite difference procedure in Eq. 3.7 and 3.8.

$$\Delta_{n_{(t+\frac{\Delta t}{2})}} = \left[(\dot{x}_i^A - \dot{x}_i^B)_{(t+\frac{\Delta t}{2})}\right] n_i \times \Delta \mathrm{t} \tag{3.7}$$

$$\Delta_{s_{(t+\frac{\Delta t}{2})}} = \left[\left((\dot{x}_i^A - \dot{x}_i^B)_{(t+\frac{\Delta t}{2})}\right) t_i - (\dot{\theta}^A|r^A| - \dot{\theta}^B|r^B|)_{(t+\frac{\Delta t}{2})}\right] \times \Delta \mathrm{t} \tag{3.8}$$

where Δ_n and Δ_s are normal and shear displacements. Next, the incremental normal and shear forces can be solved by Eq.3.9 and 3.10.

$$\Delta F_{n_{(t)}} = k_n \Delta_{n_{(t+\frac{\Delta t}{2})}} \tag{3.9}$$

$$\Delta F_{s_{(t)}} = k_t \Delta_{s_{(t+\frac{\Delta t}{2})}} \tag{3.10}$$

where k_n and k_t are normal and tangential contact stiffness. The results of incremental normal and shear forces $\Delta F_{n_{(t)}}$ and $\Delta F_{s_{(t)}}$, the normal and shear forces are calculated from Eq.3.11 and 3.12 as follows:

$$F_{n_{(t+1)}} = F_{n_{(t)}} + \Delta F_{n_{(t)}} = F_{n_{(t)}} + k_n \Delta_{n_{(t+\frac{\Delta t}{2})}} \tag{3.11}$$

$$F_{s_{(t+1)}} = F_{s_{(t)}} + \Delta F_{s_{(t)}} = F_{s_{(t)}} + k_t \Delta_{s_{(t+\frac{\Delta t}{2})}} \tag{3.12}$$

A Coulomb friction law is applied to obtain the maximum shear force in order to allow particles to slip when a threshold shear force is reached. The maximum shear force is calculated as:

$$F_{s_{(max)}} = c + F_n \tan \emptyset_\mu \tag{3.13}$$

where c is cohesion. $\emptyset_\mu$ is coefficient of interparticle friction. When the absolute value of shear force $F_{s_{(t+1)}}$ is greater than $F_{s_{(max)}}$, the $F_{s_{(t+1)}}$ is ordered to equal to the limit value $F_{s_{(max)}}$. If the absolute value of shear force $F_{s_{(t+1)}}$ is smaller than $F_{s_{(max)}}$, no slippage happens.

3. 3 Computer program OVAL

Kuhn (2006) created a DEM program code called OVAL to simulate the macro behaviors and explore the micro characteristics of two- and three-dimensional granular materials. OVAL code has been written using fortran base language and distributed under general public license (GNU). This study used OVAL for three-dimensional simulation. Thus, the OVAL three-dimensional is described. In OVAL three-dimension, particles in shapes of spheres, ellipsoidal, bumpy can be used as granular materials. The simulation scheme can be chosen between stress and strain controlled. Stress controlled method is run by imposed stress rates whereas and strain controlled method is by imposed strain rates (see Fig. 3.1). Using three-dimensional simulation, three directions of imposed stress and strain rates are needed (one vertical and two horizontal). To compile fortran in this study, G77 was used. Some brief details of OVAL are described in the next section (Kuhn 2006).

3.3.1 Linear contact models

OVAL provides two contact models using in DEM. One is linear spring contact model and second is Hertz-Mindlin contact model. This study used linear spring contact model as shown in graphic diagram in Fig.3.3. The normal and tangential contact stiffness k_n and k_t are set constantly in linear spring contact model. In Fig.3.3, a shear slider is added in shear direction to allow slippage of particles. In OVAL, k_n and k_t are fixed value as input parameters in the run file. In this study, the ratio of $k_n/k_t = 1$ is used because there are more similar results of deviatoric stress – strain behavior even using small value of k_n/k_t (Chantawarangul 1993).

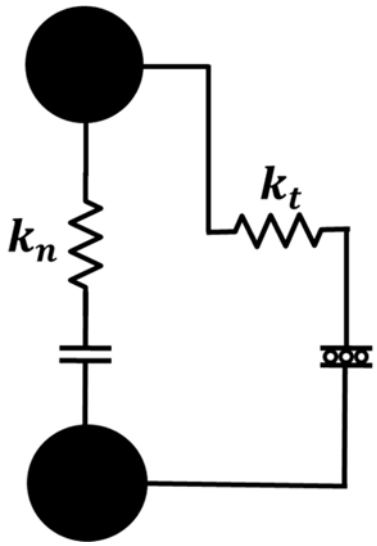

Fig. 3.3 DEM Linear spring contact model

3.3.2 Periodic Space Boundary

This study uses the periodic space boundary type provided in OVAL. In order to remove the effect of boundary on the specimen, the periodic boundary was introduced. Fig. 3.4 shows the corresponding periodic boundary of two- and three-dimensional space. Considering Fig.3.4 of two dimensional periodicity, a part of discs group *abcd*, located outside the left limit of the rectangular space, and reappearing at a corresponding point of the right limit. The part of spheres group *abcd* in three-dimension can be explained in a periodic box of three-dimension in Fig. 3.4. The periodic cell is surrounded by identical cells in two dimensions while the periodic box is surrounded by identical boxes in three-dimension. Particles, missed one side, reappear in the other side. Therefore, the specimen is borderless. Moreover, using the periodic boundary in DEM allows a small number of particles to be representative of the simulated sample.

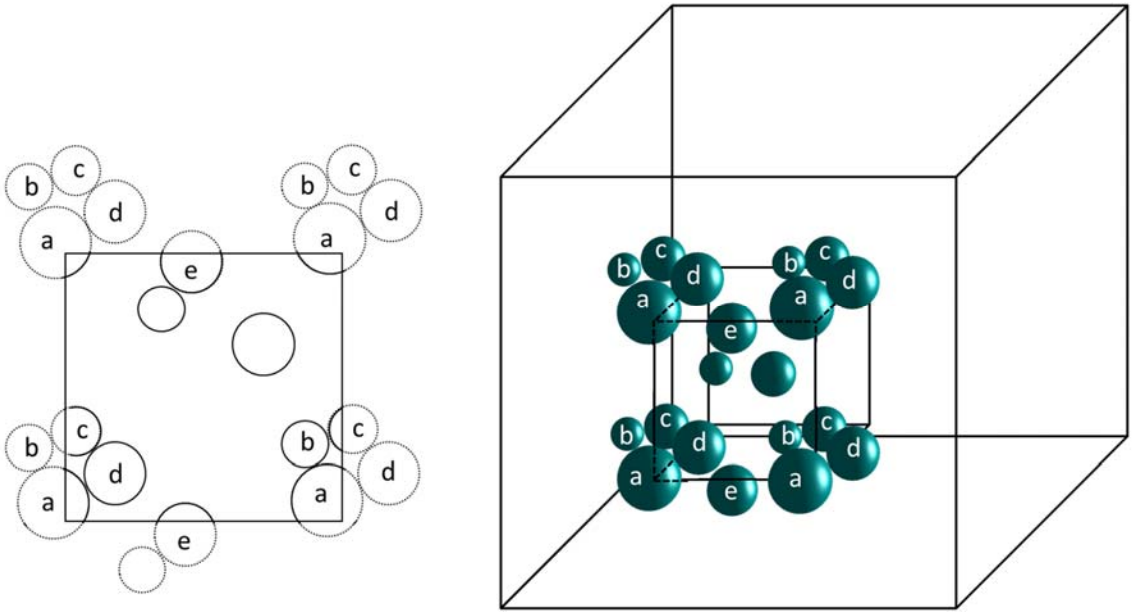

Fig. 3.4 Periodic Space Boundary (after Chantawarangul 1993)

3.3.3 Simulation Stability

In this study, the DEM simulation was stopped when the unbalanced force index I_{uf} was 1% (Kuhn 2006; Ng 2006). The unbalance force, I_{uf}, is described as follows:

$$I_{uf} = \sqrt{\frac{\sum_{p=1}^{N_p} (\text{unbalanced forces})^2 / N_p}{\sum_{c=1}^{N_c} (\text{contact forces})^2 / N_c}} \times 100\,(\%) \qquad (3.14)$$

where N_p and N_c represent the number of particles and contacts respectively. A small unbalanced force index indicates that the simulation was assumed to be close to a quasi-static condition (Kuhn 2006; Ng 2006). Moreover, in order to remain quasi-static and stable, the sample was sheared using a small stress rate to achieve a small strain rate and a small unbalanced force index (Suzuki and Kuhn 2013).

In order to maintain the small unbalanced force during simulation, the time step Δt plays an important role in the accurate numerical results. The critical time step Δt_c is the limit of the selected time step Δt. Δt_c as shown below:

$$\Delta t_c = 2 \times \sqrt{\frac{m_{min}}{k_{max}}} \tag{3.15}$$

where m_{min} is the minimum mass of particles in a granular assembly. k_{max} is the maximum contact stiffness. The method to select time step Δt can be used a fraction constant λ as follows:

$$\lambda = \frac{\Delta t}{\Delta t_c} \tag{3.16}$$

Different researches have been studied the value of λ. For example, Ng (2006) reported that λ should be smaller than 0.2 in order to keep the small unbalance force. O'Sullivan and Bray (2004) recommended that λ is 0.085 in the three-dimensional simulation. Normally, a small time step is appropriate for the stability of numerical simulations. However, it takes much time. The other parameter such as damping coefficient is also a significant factor affecting the unbalance force.

3.3.4 Damping scheme

OVAL provides two types of damping; mass damping and contact damping. This study used the mass damping which can be categorized into translational mass damping C_t and rotational mass damping C_r. The mass damping can be shown in Eq. 3.1 and 3.2.

$$m^A \ddot{x}_i^A = \sum F_i^A - C_t \dot{x}_i^A \tag{3.17}$$

$$I\ddot{\theta}^A = \sum M^A - C_r \dot{\theta}^A \tag{3.18}$$

To identify translational mass damping C_t and rotational mass damping C_r, the coefficient of viscosity for translational and rotational body damping, C_t' and C_r' are used by apply equations as follow:

$$C_t' = \frac{C_t}{C_t^{crit}} \tag{3.19}$$

$$C_r' = \frac{C_r}{C_r^{crit}} \tag{3.20}$$

where $C_t^{crit} = 2\sqrt{mk_n}$ and $C_r^{crit} = 2r\sqrt{mk_n}$ (Tu and Andrade 2008) (3.21)

3. 4 Method to input stress rates for changing stress direction

In order to simulate the granular materials to fulfill the objectives of this study, the method to input stress rates and strain rates is described here. As shown in Fig. 3.1, imposed stress rate is used for stress controlled while imposed strain rate is used for strain controlled method. One objective of this study is to study the macro behaviors and micro responses of granular materials under continuously varying *b* value and constant mean stress in generalized stress systems. The

stress controlled method is necessary in this study. The method to stress parameters in OVAL is explained as follow:

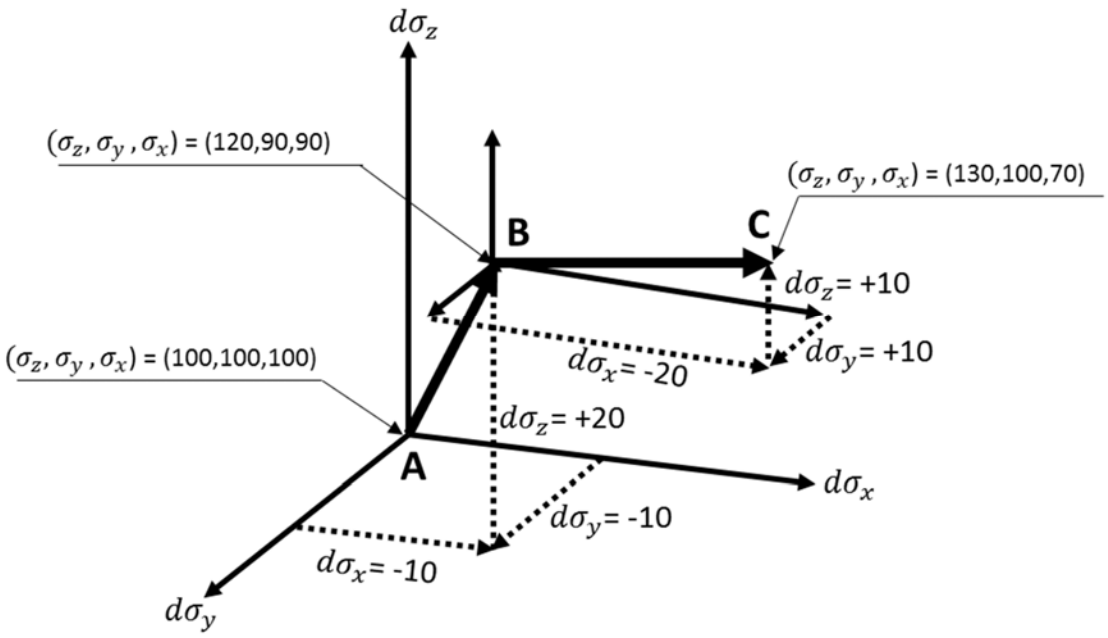

Fig. 3.5 Method to input stress rates for changing stress direction.

Fig. 3.5 shows the method to input stress rates for changing stress direction. The figure shows the applied stress rates in x, y and z directions. In Fig.3.5, the sample at point A has stresses σ_z, σ_y, σ_x = 100, 100, 100 kPa and b = 0 (using Eq.2.1). Next, the applied stress rates in x and y directions are extension 10 kPa at each direction and in z direction are compression 20 kPa. Thus, stresses at point B are σ_z, σ_y, σ_x = 120, 90, 90 kPa and b = 0.0. Therefore, b value is constant for stress path AB. Further from point B, the applied stress rates are changed to be extension 20 kPa in x direction and compression 10 kPa in y and z direction. The stress path moves from point B to C where σ_z, σ_y, σ_x = 130, 100, 70 kPa and b = 0.5. In the stress path BC, b value changes from 0.0 to 0.5. This indicates that b value continuously change. This method is used in chapter 4 for creating continuously varying b value stress paths.

Chapter 4 Macro-Micro Behavior under Continuously Varying *b* Value

4.1 Introduction

The intermediate principal stress σ_2 can significantly affect the stress-strain behavior of granular materials. A non-dimensional parameter b [= $(\sigma_2-\sigma_3)/(\sigma_1-\sigma_3)$] was introduced by Habib (1953) as a stress ratio to describe the influence of σ_2. Several experiments have been conducted to study the influence of σ_2 on the behavior of sand under different stress paths, with a constant b value (e.g., (Kumruzzaman and Yin 2012; Lade 2006; Lade and Duncan 1973; Matsuoka and Sun 1995; Rodriguez and Lade 2013; Sun et al. 2008; Suzuki and Yanagisawa 2006; Zhang et al. 2014). Most of these experiments examined the relationship between the b value and the angle of shearing resistance ϕ [= $\sin^{-1}((\sigma_1-\sigma_3)/(\sigma_1+\sigma_3))$] at peak strength. For instance, Ko and Scott (1967) and Yamada and Ishihara (1979)reported that ϕ increases from b = 0 to a certain value (nearly b = 0.5) and then decreases slowly when approaching unity. Similar result was reported recently by Kumruzzaman and Yin (2012)as well as Rodriguez and Lade (2013). However, Green and Bishop (1969)and Lade and Duncan (1973)reported different results. According to their studies, after certain values of b (nearly b = 0.2), ϕ remains almost constant or decreases or even increases with increasing b, before it decreases when approaching unity. Matsuoka and Nakai (1978)reported different findings than others; according to their study, after certain values of b (nearly b = 0.3), ϕ decreases with the increasing b value until b = 1. Further, Lade (2006)concluded that most experimental results on sand show that ϕ increases from b = 0, depending on a particular type of sand. Different relationships between ϕ and b indicate that type of sand, sample preparation and loading conditions may influence such relations. In order to explore the mechanical behavior rigorously and objectively, computer simulations can be used effectively, which is the motivation of the present study. Numerical simulations used in the

present study were based on the DEM approach – a well-recognized method for simulation of granular materials.

An experimental study can be quite challenging and expensive for such cases. DEM has been widely used for simulating granular materials and for investigating mechanical behavior of granular materials (Barreto and O'Sullivan 2012; Chantawarangul 1993; Kuhn 1999; Salot et al. 2009; Sazzad et al. 2012; Thornton 2000). Behavior of sand at the micro level in response to an applied load, including changing inter-particle friction angles and different *b* values, has been studied before. For example, Thornton (2000) using disc particles examined the effect of intermediate principle stress under constant mean stress condition, using Lade and Duncan's (1975) failure model. Ng (2004a) using oval particles reported the effect of intermediated principal stress and stress-strain behavior under constant *b* tests using the DEM and noted that the angle of shearing resistance ϕ from the DEM results supports the models of Lade (1977) and Ogawa et al. (1974) better than the models of Stake (1975) and Matsuoka and Nakai (1978). Further, Ng (2005) studied the effects of different densities under different stress paths of constant *b* test and concluded that the density of samples has no noticeable influence on the relationship between ϕ and *b*. In another study, Sazzad et al. (2011) used spherical particles of DEM to simulate the macro mechanical responses and to explore the micro characteristics of granular materials under constant *b* tests. The relationship between ϕ and *b* reported by Sazzad et al. (2011) was similar to that of the experiment of Ko and Scott (1968). According to Sazzad et al. (2011), the evolution of the principal deviatoric strains, directions of stress increment vector and strain increment vector as well as dilatency from the DEM results exhibit good consistency with the experimental observations, at least qualitatively. Comparing DEM simulations using spherical particles and experimental data, Barreto and O'Sullivan (2012) demonstrated that the *b* value can significantly influence the coefficient of inter-particle friction μ.

The aforementioned literature shows that DEM simulations have generally been conducted with a constant *b* value. In reality, however, the stress path changes its direction continuously in the stress space, which causes a change in the *b* value. Experimentally, the relationship between a strain increment and the stress increment direction, under more generalized stress paths, has

been performed (Matsuoka and Sun 1995; Nakai et al., 2003). However, to the authors' knowledge, DEM simulations of granular materials under a continuously varying *b* value have not been reported yet.

There were two main objectives of this research. The first objective was to develop a DEM model (specimen with discrete particles) and simulate the behavior of the specimen under truly triaxial generalized stress conditions, defined by continuously varying *b* values. The second objective was to explain the experimentally observed macro behavior using the micro response from the DEM simulations, and to examine the relationship between macro and micro behaviors. Both constant *b* tests and continuously varying *b* tests were simulated under a constant mean stress using the stress-controlled method. The principal stresses were set by changing the stress rates to increase or decrease stresses in the DEM. The results were analyzed in the following section, and the macro and micro behaviors were correlated.

4.2 Sample preparation and simulation program

A cubical sample was modeled three-dimensionally using 8,000 spheres of 16 different diameters (3 - 4.5 mm.), as presented by Sazzad et al. (2011). The periodic boundary was used as the boundary condition in the DEM simulation. Fig. 4.1(a) shows the initial model of the cubical sample with a length of 10.5 cm. After the spheres were placed in position, an isotropic compression force was applied. In order to create a dense sample, the inter-particle friction coefficient μ was set to zero in the isotropic compression state. A stress rate of 10^6 Pa/sec with a time increment of 10^{-6} sec was used until the isotropic compression reached 100 kPa. Fig. 4.1(b) shows the final model of the sample before shearing with a length of 7.1 cm and a void ratio of 0.57.

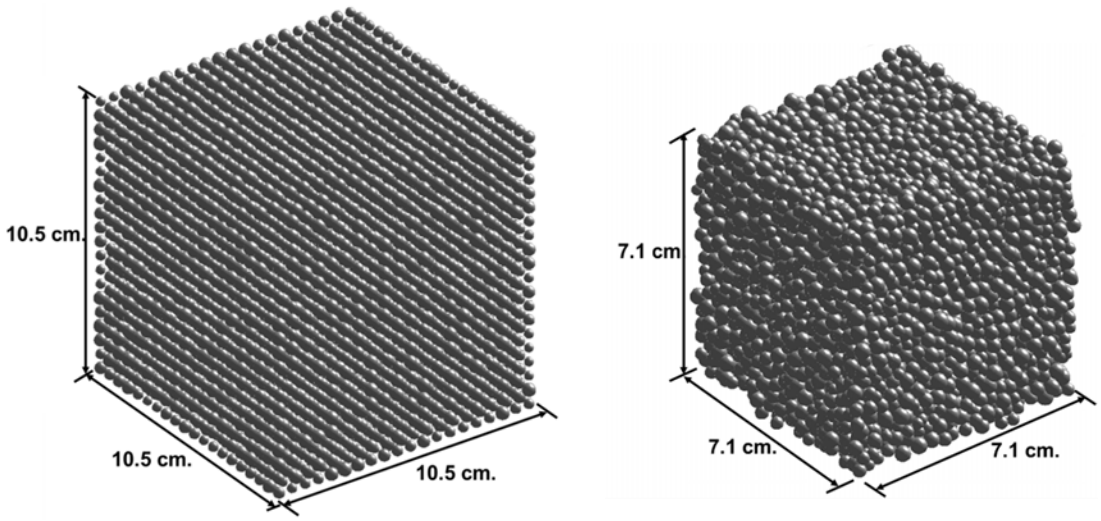

Fig. 4.1 Sample preparation and isotropic compression: (a) Before isotropic compression; (b) After isotropic compression

After isotropic compression, the sample was sheared under a truly triaxial condition for both constant *b* tests and continuously varying *b* tests using the stress-controlled method under a constant mean stress p = 100 kPa. A maximum stress rate of $2x10^7$ Pa/sec with a time increment of 10^{-6} sec was used for shearing. The DEM input parameters are summarized in Table 4.1. Two series of stress paths were used in the simulation. Figs. 4.2(a) and 4.2(b) show a projection of those stress paths on the π-plane, for different angles and *b* values. Fig. 2(a) shows the first set, called constant *b* tests, consisting of 5 selected stress paths, namely A0˚, A16˚, A30˚, A44˚, and A60˚ where b = 0, 0.3, 0.5, 0.7 and 1, respectively. The numbers after letter A indicate the angle between the stress paths and the direction of the major principal stress σ_1. Fig. 4.2(b) shows the second set, called continuously varying *b* tests, consisting of 6 selected stress paths of AB and AC series. The set AB is called AB30˚, AB60˚, AB90˚and the set AC is called AC30˚, AC60˚, and AC90˚. The numbers after AB and AC indicate the angle of deviation from the stress paths AB (anticlockwise) and AC (clockwise). These 11 stress paths start from point A where the major, intermediate, and minor stresses were 100 kPa and the principal deviatoric stresses were zero.

Specimens along all 11 stress paths were then sheared using the stress-controlled method. The constant *b* tests (Fig. 4.2(a)) were performed for loading state. The other 6 continuously varying *b* tests (Fig. 4.2(b)) were tested from point A to B with stresses (σ_1, σ_2, σ_3 = 148, 76, 76 kPa, respectively) and point A to C with stresses (σ_1, σ_2, σ_3 = 124, 124, 52 kPa, respectively), then following the different directions, as shown.

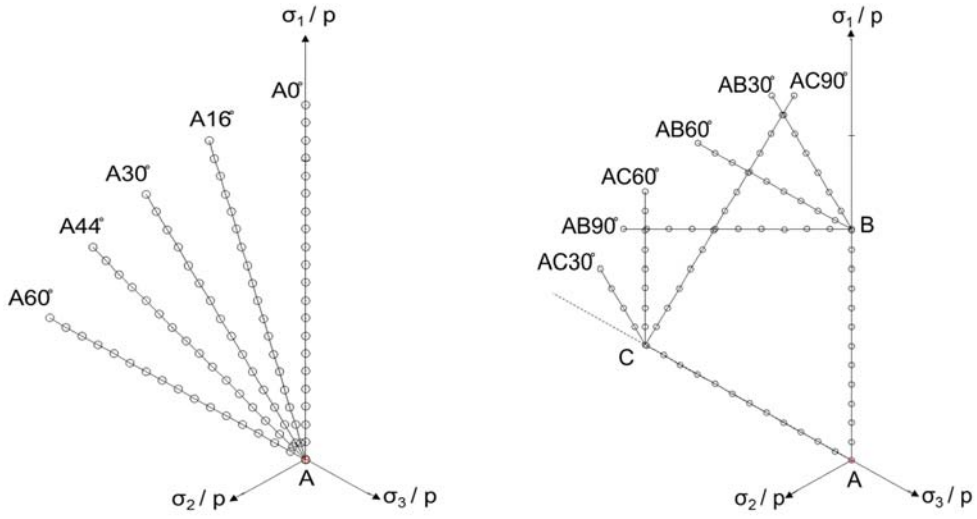

Fig. 4.2 Stress paths on the normalized π-plane: (a) Constant b tests; (b) Continuously varying b tests.

Figs. 4.3(a) and 4.3(b) shows the relationship between the *b* value and the equivalent deviatoric strain ε_d (%) of stress paths in Figs. 4.2(a) and 4.2(b), respectively. The equivalent deviatoric strain is defined as follows:

$$\varepsilon_d = \sqrt{\frac{2}{3}\left\{(\varepsilon_1 - \varepsilon_2)^2 + (\varepsilon_2 - \varepsilon_3)^2 + (\varepsilon_1 - \varepsilon_3)^2\right\}} \tag{4.1}$$

Fig. 4.3(a) indicates that the b value remains constant throughout the simulation for constant b tests. For continuously varying b tests, Fig. 4.3(b) shows that the b value is constant ($b = 0$) from point A to B, then, increases up to 0.22, 0.43 and 0.71 for AB30˚, AB60˚, and AB90˚, respectively, while the b value is constant ($b = 1$) from points A to C, but, decreases to 0.84, 0.63, and 0.32 for AC30˚, AC60˚, and AC90˚, respectively. The Figs show the b value ranging between 0 and 1 ($0 \leq b \leq 1$). In Fig. 4.4, it is seen that the mean stress p [$= (\sigma_1 + \sigma_2 + \sigma_3)/3$] was kept constant throughout the simulation for all tests, where q is the deviatoric stress defined as follows:

$$q = \sqrt{\frac{1}{2}\left\{(\sigma_1 - \sigma_2)^2 + (\sigma_2 - \sigma_3)^2 + (\sigma_1 - \sigma_3)^2\right\}} \tag{4.2}$$

In this study, the DEM simulation was stopped when the unbalanced force index I_{uf} (see Eq. 3.14) was 1% (Kuhn 2006; Ng 2006). A small unbalanced force index indicates that the simulation was assumed to be close to a quasi-static condition (Kuhn 2006; Ng 2006). Moreover, in order to remain quasi-static and stable, the sample was sheared using a small stress rate to achieve a small strain rate and a small unbalanced force index (Suzuki and Kuhn 2013). In this study, a positive value of stress represents compression, while a negative value of stress represents extension.

Table 4.1 Simulation Parameters for shearing

Parameters	Type or value
Mass density	2,650 kg/m^3
Stiffness	1×10^6 N/m
Damping	0.05
Increment of time step Δt	1×10^{-6} sec
Initial void ratio e_0	0.57
Inter-particle friction coefficient	
• Isotropic compression	0.0
• Shearing	0.5
Strain rate $\dot{\varepsilon}$ and Stress rate $\dot{\sigma}$	
• Isotropic compression	
- First stage $\dot{\varepsilon}_1$, $\dot{\varepsilon}_2$, $\dot{\varepsilon}_3$	100%/sec
- Second stage $\dot{\sigma}_1$, $\dot{\sigma}_2$, $\dot{\sigma}_3$	1×10^6 Pa/sec
• Shearing	
- Maximum stress rate	2×10^7 Pa/sec
- Minimum stress rate	-2×10^7 Pa/sec
Maximum stress rate $\Delta\sigma$	2×10^7 Pa/sec

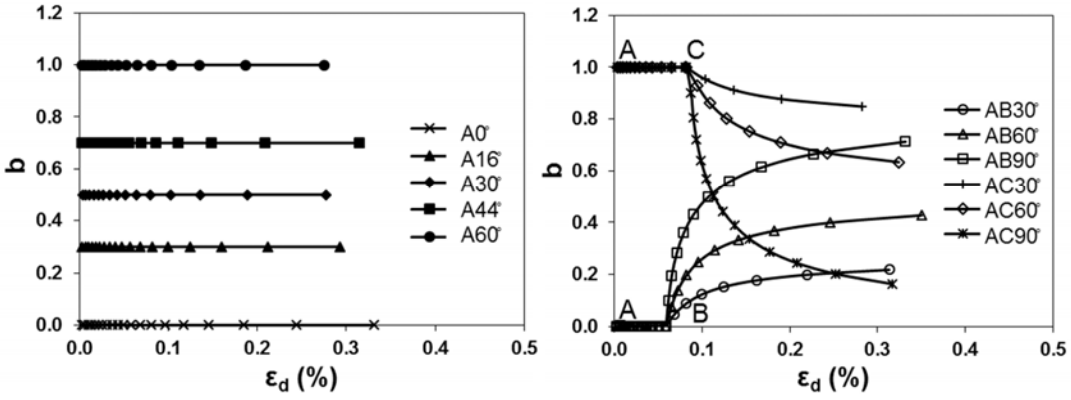

(a) (b)

Fig. 4.3 Relationship between b value and equivalent deviatoric strain: (a) Constant b tests; (b) Continuously varying b tests.

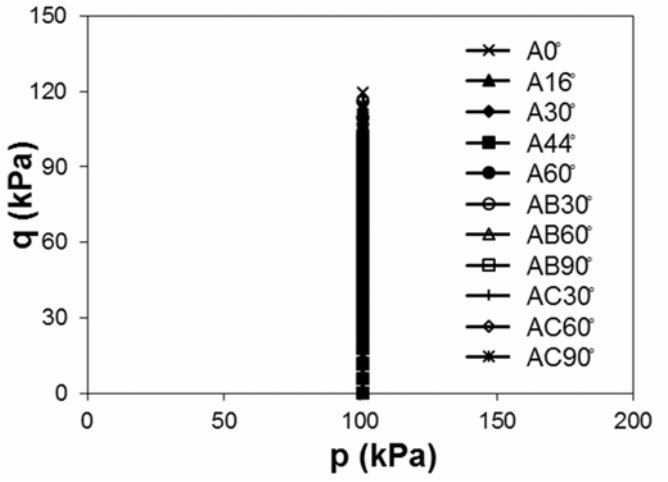

Fig. 4.4 *q-p* stress paths of all tests.

4.3 Results

4.3.1 Stress-strain relationship

Figs. 4.5(a) and 4.5(b) show the relationship between the stress ratio *q/p* and the equivalent deviatoric strain ε_d (%) for constant *b* tests and continuously varying *b* tests, respectively. These Figs indicate that the stress-strain curves are different depending on the type of test (constant *b* or continuously varying *b*). The results of constant *b* tests were previously reported by Suzuki and Yanagisawa (2006), based on laboratory tests on sands having different levels of inherent transverse isotropy, and by Thornton (2000) and Sazzad et al. (2011) using DEM simulations on a dense sample under monotonic loading. For continuously varying *b* tests, the finding was confirmed by the laboratory observations by Matsuoka and Sun (1995) using cemented sand. It is worth noting that the *b* value plays an important role in the stress ratio, linking to change in the macro behavior of granular materials. The relationship between the angle of shearing

resistance, ϕ, and the b value of the final points on the stress-strain curves in Figs. 4.5(a) and 4.5(b) is shown in Fig. 4.6. The Fig. shows that the angle of shearing resistance, ϕ, increases up to a certain value of b and then decreases when approaching to unity for both constant b and continuously varying b tests. It is evident that the b value has influence to the angle of shearing resistance. The relationship between ϕ and b in Fig. 4.6 is very close to the experimental results reported Kumruzzaman and Yin (2012) as well as Rodriguez and Lade (2013) and the DEM results reported by Sazzad et al. (2011) for constant b value tests.

In this section, the DEM simulation results from this study were validated with the results from the literature involving either experimental studies or simulation studies. Table 4.2 and Table 4.3 are summary of specific information from those literature, including material types, type of test, sample preparation method, and degree of saturation. It can be seen from Table 4.2 and Table 4.3 that there are differences in types of materials as well as type of tests between those in the literature and the simulation conducted in this study. These differences were not taken into account with respect to the degree of accuracy because only qualitatively comparisons could be made.

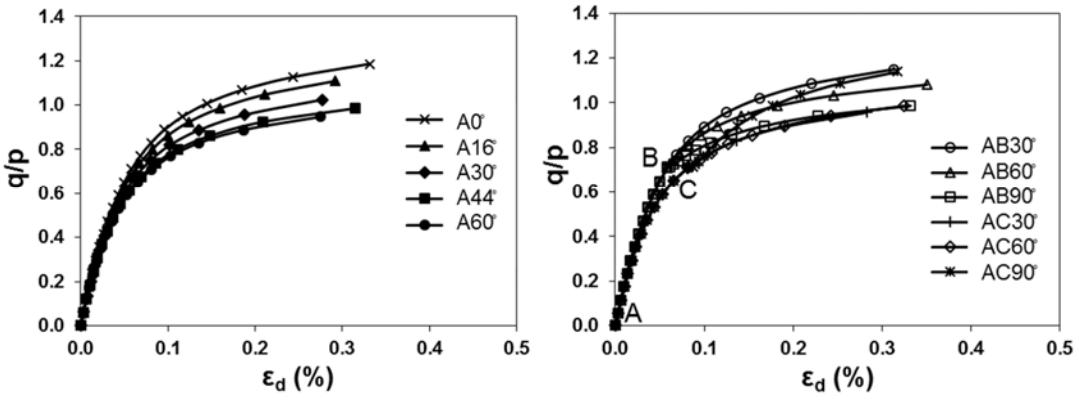

(a) (b)

Fig. 4.5 Stress-strain relationship: (a) Constant b tests; (b) Continuously varying b tests.

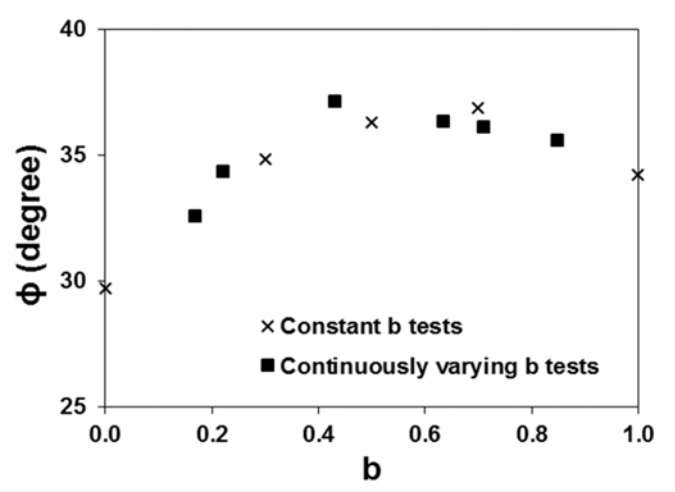

Fig. 4.6 Relationship between the angle of shearing resistance ϕ and the b value of the final points of stress-strain curves in Fig. 4.4.

4.3.2 Dilatancy behavior

Figs. 4.7(a) and 4.7(b) represent the nonlinear evolution of volumetric strain ε_v (%) and the major principle strain ε_1 (%) for constant *b* and continuously varying *b* tests, respectively. The volumetric strain can be defined as $\varepsilon_v = dv/v$ where *dv* is the change in volume and *v* is the initial volume at the beginning before shearing. Both tests show that the sample dilated while shearing, as expected. This dilation was typical, as observed in laboratory experiments on dense sand. Figs. 4.7(a) and 4.7(b) show that dilatancy differs depending on the type of test (i.e., constant *b* or continuously varying *b*). Similar results have been reported using the DEM simulations involving monotonic loading, under constant mean stress and constant *b* value by Thornton (2000) and Sazzad et al. (2011) using spheres particles under DEM simulation (see Table 4.3). It can be noted that continuously varying *b* value influences the volumetric strain. Specifically, the relationship between the dilatency index *DI* and the equivalent deviatoric strain ε_d (%) under constant *b* and continuously varying *b* tests is captured in Fig. 4.8. The dilatency index is defined

as $DI = -d\varepsilon_v / d\varepsilon_d$, where $d\varepsilon_v$ is the change in volumetric strain and $d\varepsilon_d$ is the increment of equivalent deviatoric strain. From Fig. 4.8, it is seen that the evolution of *DI* has relatively small influence on the *b* values. These results point to a unique relationship between *DI* and ε_d regardless of the difference in stress paths.

Table 4.2 Summary of the specific information of experimental literature for validating the results of DEM simulation in this study

Literature	Materials	Type of Test	Sample preparing method	Approximate degree of saturation
Matsuoka and Sun (1995)	C emented sand C-1 (Toyoura:Cement: Water=15:3:1)	Drained True Triaxial	Soil mixer	0%
Suzuki and Yanagizawa (2006)	Toyoura sand ($D_{50} = 0.17\ mm$)	Drained True Triaxial	Multiple-sieve pluviation	0 %
Sun et al. (2008)	Toyoura sand ($D_{50} = 0.18\ mm$)	Drained True Triaxial	Compacted in six layer	0 %
Kumruzzaman and Yin (2012)	Granite fill (sand content 62.5 %)	Drained True Triaxial	Compacted to 95 % of maximum dry density	Very small
Rodriguez and Lade (2013)	Fine Nevada sand ($D_{50} = 0.23\ mm$)	Drained True Triaxial	Pluviation, saturation and freezing	100%

Table 4.3 Summary of the specific information of experimental literature for validating the results of DEM simulation in this study

Literature	Materials	Type of Test	Sample after isotropic compression	Approximate degree of saturation
Sazzad et al. (2011) and **this study**	Sphere (diameter 3-4.5 mm)	True Triaxial Simulation	Dense	0 %
Ng (2004a) and Ng (2004b)	Ellipsoids	True Triaxial Simulation	Dense	0 %
Antony (2004)	Oval and circular (diameter 0.45-1.65 unit)	Bi-axial Simulation	Dense	0 %
Ng (2000)	Spheres (diameter 0.135-0.40 mm)	True Triaxial Simulation	Dense	0 %

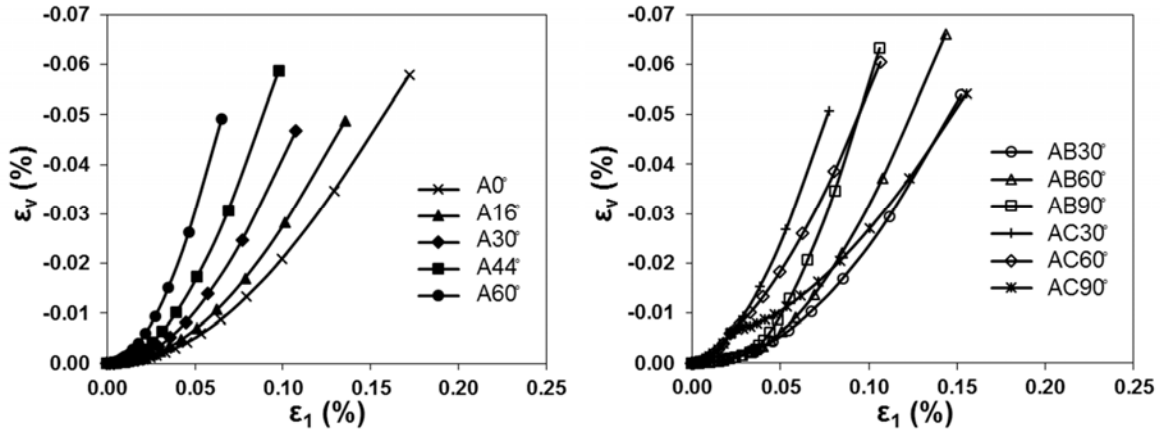

(a) (b)

Fig. 4.7 Relationship between volumetric strain and the major principle strain: (a) Constant b tests; (b) Continuously varying b tests.

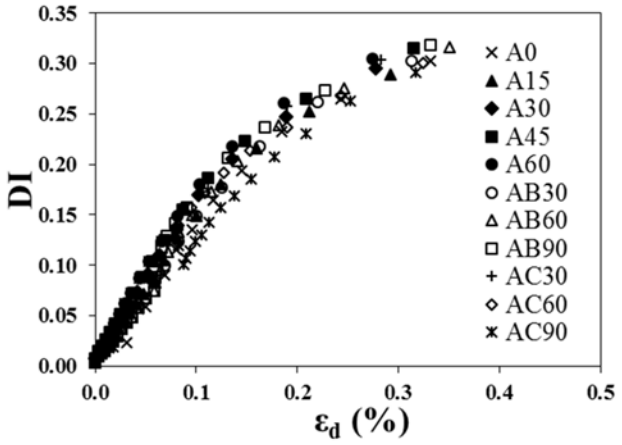

Fig. 4.8 Relationship between dilatency index and the equivalent deviatoric strain of all tests.

4.3.3 Principal Strain and Principal Deviatoric Strain

Figs. 4.9(a) through 4.9(f) show the relationship between ε_3 versus ε_1, ε_2 versus ε_1, e_3 versus e_1, and e_2 versus e_1, based on the DEM results, where e_1, e_2 and e_3 represent major, intermediate, and minor principal deviatoric strains, respectively, and ε_1, ε_2 and ε_3 represent major, intermediate, and minor principal strains, respectively. The principal deviatoric strains were calculated from the principal strains as $e_1 = \varepsilon_1 - \varepsilon_m$, $e_2 = \varepsilon_2 - \varepsilon_m$, and $e_3 = \varepsilon_3 - \varepsilon_m$, where $\varepsilon_m = (\varepsilon_1+\varepsilon_2+\varepsilon_3)/3$. From these Figs, the DEM results exhibit a nonlinear relationship between ε_3 and ε_2, also with ε_1, for both constant b and continuously varying b tests. Comparatively, a similar relationship between the principal deviatoric strains is almost linear. Similar results (Fig. 4.9(a)) have been reported previously by Suzuki and Yanagisawa (2006) based on laboratory tests and by Sazzad et al. (2011) based on DEM simulations, both involving constant b value.

4.3.4 Failure Surface, Stress Increment Vector and Strain Increment Vector

The directions of the principal strain increment vectors superimposed on the normalized π-plane for constant b and continuously varying b tests are shown in Figs. 4.10(a) and 4.10(c), respectively. For a qualitative comparison, the experimental results of truly triaxial tests on cemented sand C-1 (see Table 4.2) by Matsuoka and Sun (1995) are shown in Figs. 4.10(b) and 4.10(d). Overall, the directions of the principal strain increment vectors show a good consistency between the DEM results and the experimental results under the similar pattern of stress paths as shown in Figs. 4.10(a) and 4.10(b) as well as Figs. 4.10(c) and 4.10(d). Considering point G in Fig. 4.10(c), the direction of the principal strain increment vectors along the stress path AB60˚ is different from that along the stress path AC90˚, which can also be seen from the experimental results in Fig. 4.10(d). This is an evident that the direction of the principal strain increment vectors depends on the stress paths and DEM simulation using granular materials gives the same conclusion with the experiment of Matsuoka and Sun (1995). For further study, it is important to compare the simulated results with the experimental data quantitatively.

Moreover, Fig. 4.11(a) shows the principal strain increment vectors superimposed on the failure surface on the normalized π-plane at the final points of stress-strain curves for constant *b* and continuously varying *b* tests (refer to Fig. 4.5(a)). The Fig. also includes the failure surface proposed by Lade and Duncan (1975) for comparison with the DEM results. It is seen that the failure surface based on the DEM results is convex and is in good agreement with that of the Lade and Duncan (1975). Additionally, Fig. 4.11(b) explains the directions of the principal strain increment vectors of the stress paths AC90˚ and AC′90˚. The stress path AC′90˚ was created to compare the direction of the principal strain increment vectors between AC90˚ and AC′90˚, for stress ratios (*q/p*) of 0.7 and 0.5, respectively. Interestingly, the directions of the principal strain increment vectors for stress paths AC90˚ and AC′90˚ are different even though the directions of the principal stress increment are the same. A stress ratio than *q/p* = 0.7 at point C indicates that the stress path AC90˚ is closer to the failure surface than AC′90˚ and thus affects the directions of the principal strain increment vectors. Therefore, the direction of the principal strain increment vectors is not only dependent on the direction of the stress increment vectors but on the approximate failure surface.

Furthermore, the angle θ_σ is between the principal stress vectors and the maximum principal stress axis. The DEM results can be estimated using the general relationship between the principal stress increment vector and the principal strain increment vector on the normalized π-plane (or π_σ), as shown in Fig. 4.12. The corresponding Eq. can be expressed by Suzuki and Yanagisawa (2006) as follows:

$$\theta_\sigma = \tan^{-1}\left(\frac{\sqrt{3}b}{2-b}\right) \tag{4.3}$$

The relative magnitude of the intermediate principal stress increment is given as

$$b_{d\sigma} = \frac{d\sigma_2 - d\sigma_3}{d\sigma_1 - d\sigma_3} \tag{4.4}$$

In Eq. (4.5), the $b_{d\sigma}$ value is related to the $\theta_{d\sigma}$ as follows:

$$\theta_{d\sigma} = \tan^{-1}\left(\frac{\sqrt{3}b_{d\sigma}}{2-b_{d\sigma}}\right) \tag{4.5}$$

Similarly, the angle between the principal strain increment vector and the maximum strain increment axis can be expressed as

$$\theta_{d\varepsilon} = \tan^{-1}\left(\frac{\sqrt{3}b_{d\varepsilon}}{2-b_{d\varepsilon}}\right) \tag{4.6}$$

where

$$b_{d\varepsilon} = \frac{d\varepsilon_2 - d\varepsilon_3}{d\varepsilon_1 - d\varepsilon_3} \tag{4.7}$$

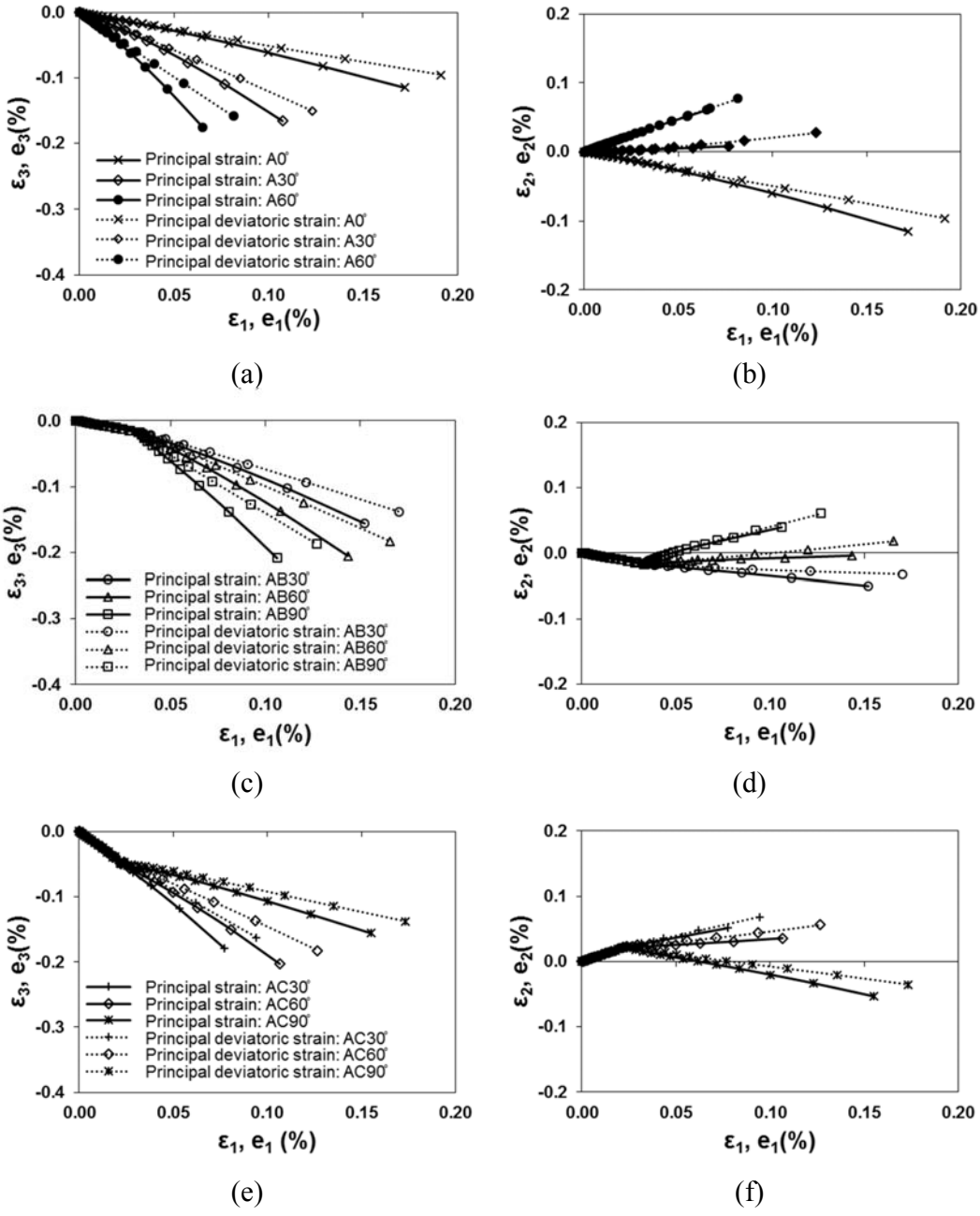

Fig. 4.9 Relationships among the principal strains and principal deviatoric strains of all tests: (a), (c) and (e) ε_3, e_3 versus ε_1, e_1; (b), (d) and (f) ε_2, e_2 versus ε_1, e_1.

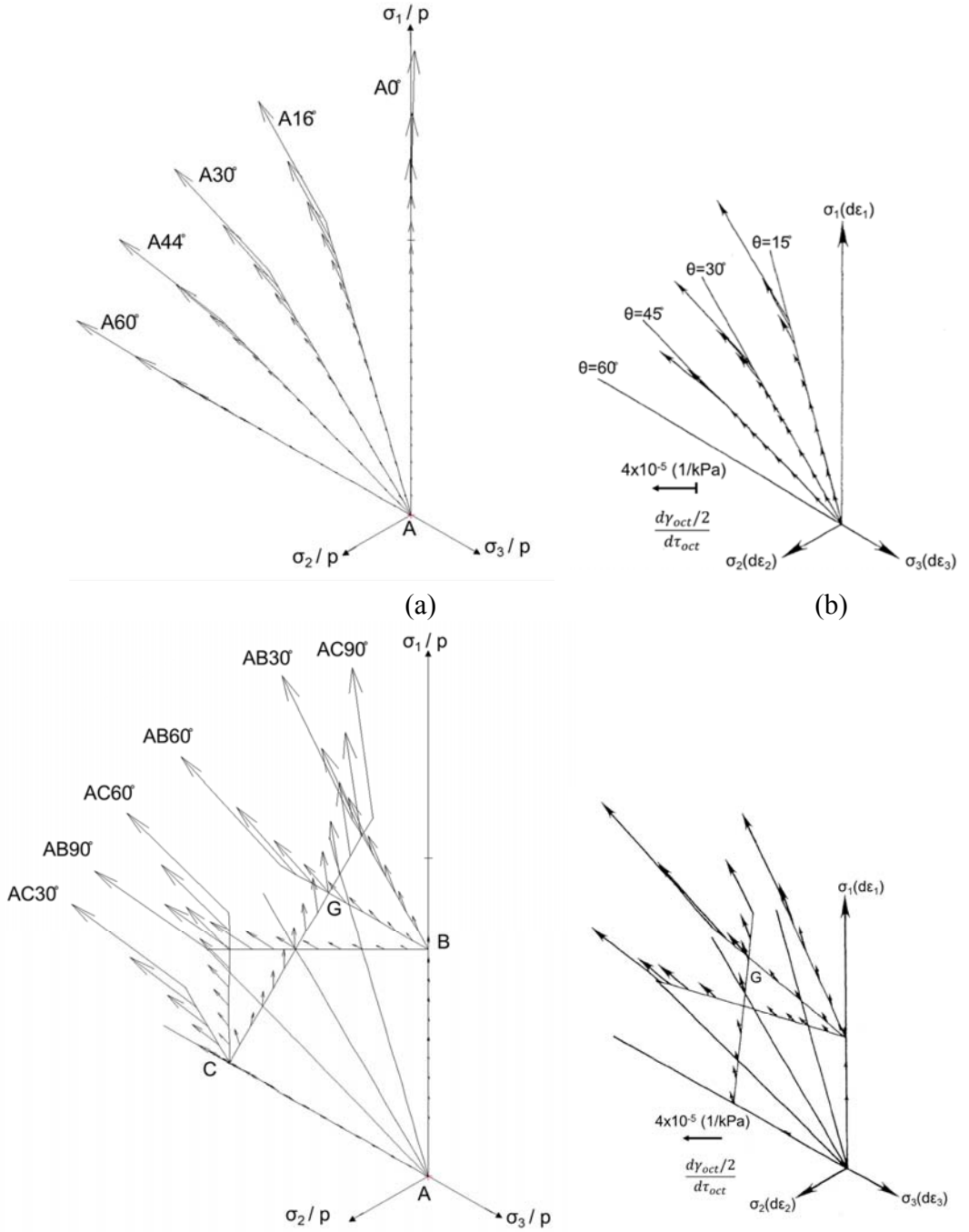

Fig. 4.10 Directions of strain increments superimposed on the normalized π plane: (a) Constant *b* tests; (c) Continuous variable *b* tests; (b) and (d) true triaxial tests on cemented sand C-I (after Matsuoka and Sun 1995).

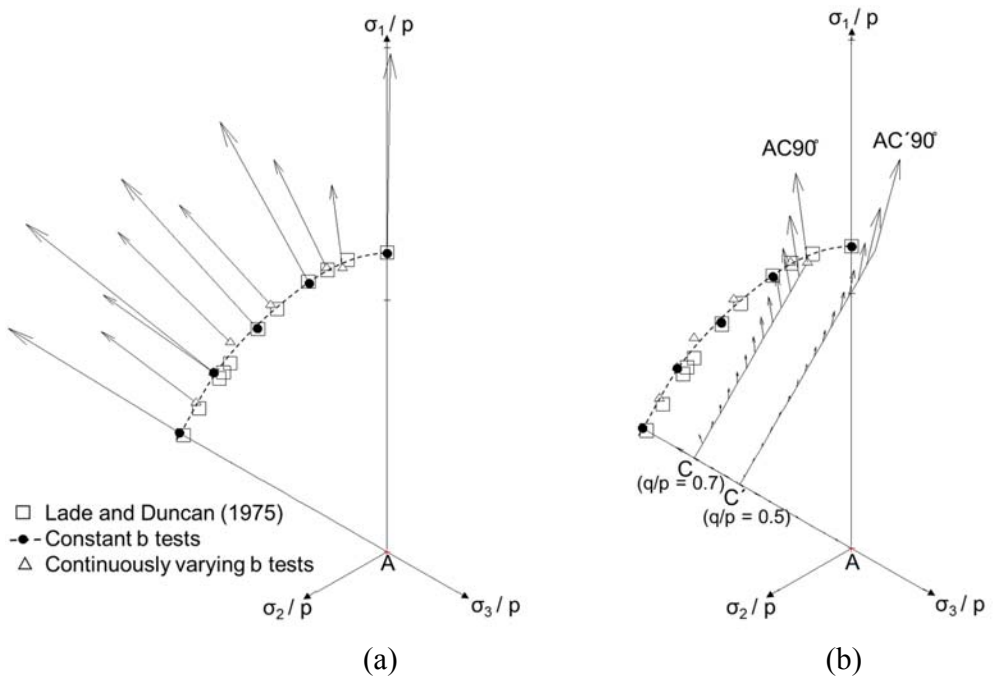

Fig. 4.11 Directions of strain increments superimposed on the failure surface from DEM results and Lade and Duncan (1975) criteria: (a) the final point of stress-strain curves in Fig. 4; (b) the stress paths AC90˚and AC´90˚.

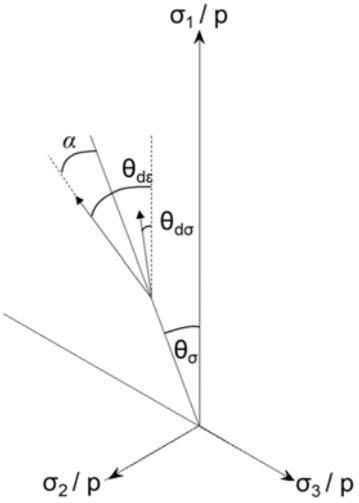

Fig. 4.12 General relationship of the principal stress increment vector and the principal strain increment vector on the normalized π plane (after Suzuki and Yanagizawa, 2006)

The evolution of $\theta_{d\sigma}$ and $\theta_{d\varepsilon}$ with the equivalent deviatoric strain ε_d is shown in Figs. 4.13(a) and 4.13(b) for constant b tests and in Figs. 4.13(c) through 4.13(f) for continuously varying b tests, respectively. It is seen from Figs. 4.13(a) and 4.13(b) that $\theta_{d\sigma}$ and $\theta_{d\varepsilon}$ remain almost constant for the stress paths A0˚ and A60˚, where $b = 0$ and 1, respectively. However, $\theta_{d\varepsilon}$ deviates from $\theta_{d\sigma}$ as ε_d increases. This deviation between $\theta_{d\varepsilon}$ and $\theta_{d\sigma}$ was confirmed in the experimental results reported by Sun et al. (2008) and Suzuki and Yanagisawa (2006), and in the DEM results reported Sazzad et al. (2011). In addition, it is evident from Figs. 4.13(c) through 4.13(f) that $\theta_{d\varepsilon}$ deviates rapidly from $\theta_{d\sigma}$ and gradually becomes constant when the ε_d increases under continuously varying b tests from points B and C. The results from Figs. 4.13(a) and 4.13(b) correspond to the DEM results in Fig. 4.10(a) and the experimental results in Fig. 4.10(b) for constant b tests. Also, the results from Figs. 4.13(c) and 4.13(f) correspond to the DEM results in Fig. 4.10(c) as well as the experimental results in Fig. 4.10(d) for continuously varying b tests. It is seen that the general relationships between θ_σ, $\theta_{d\sigma}$, $\theta_{d\varepsilon}$ and the b_σ, $b_{d\sigma}$, $b_{d\varepsilon}$ values, as represented by Eq.s (4.4) through (4.8), respectively, exhibit good consistency with the experimental results. Further, the deviation of $\theta_{d\varepsilon}$ from $\theta_{d\sigma}$ can be defined by the expression

$\alpha = \theta_{d\varepsilon} - \theta_{\sigma}$. Fig. 4.14 illustrates the relationship between α and the b values for all tests at the final points of the stress-strain curves in Figs. 4.5(a) and 4.5(b). Therefore, from these results one can conclude that α is dependent on the b values.

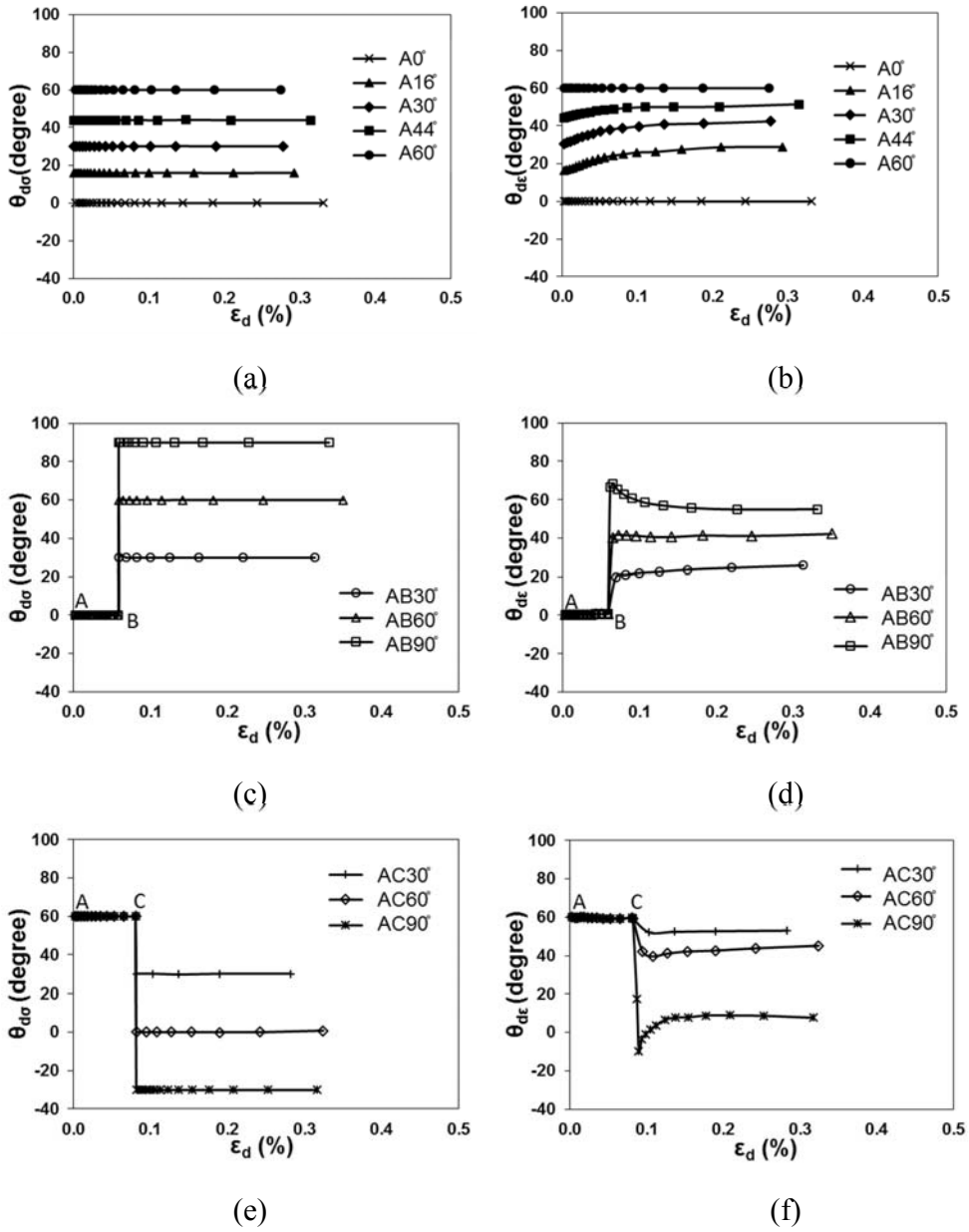

Fig. 4.13 Evolution $\theta_{d\sigma}$ and $\theta_{d\varepsilon}$ with the equivalent deviatoric strain of all tests.

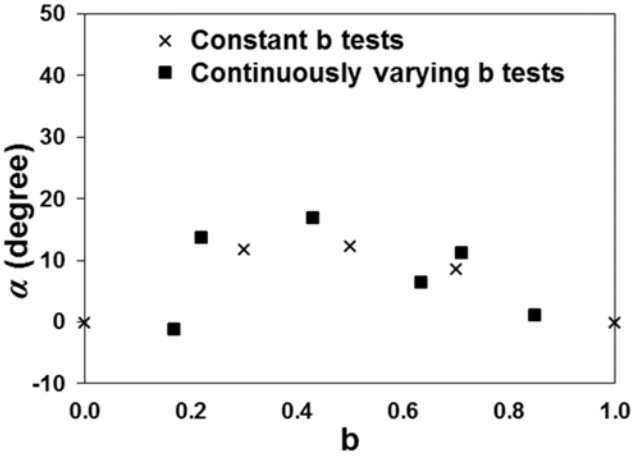

Fig. 4.14 Relationship between α and the b value of all tests.

4.3.5 Microscopic Evolution

Fig. 4.15 shows the evolution of the coordination number with the equivalent deviatoric strain ε_d (%) for constant b and continuously varying b tests. The Fig. shows that coordination number is not dependent on the stress paths. Fig. 4.16 shows the evolution of the sliding contact fraction with the equivalent deviatoric strain for continuously varying b tests. The sliding contact fraction shows the deviation under continuously varying b tests. It is noticed that the sliding contact fractions of the stress paths AB90˚and AC90˚decrease suddenly after points B and C, then, gradually increases. The reason is that when changing the directions of stress paths at point B and C, some sliding particles were break because the previous loading directions of stress path A to B as well as A to C are removed . Then, they slide again because of the new loading directions of stress path after point B and C, respectively. This result is similar to Phusing and Suzuki (2015) using DEM under unconventional triaxial cyclic loading tests.

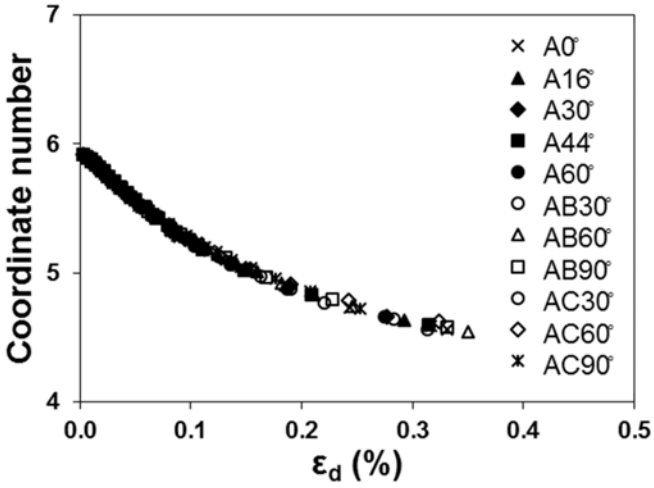

Fig. 4.15 Relationship between coordinate number and the equivalent deviatoric strain of all tests.

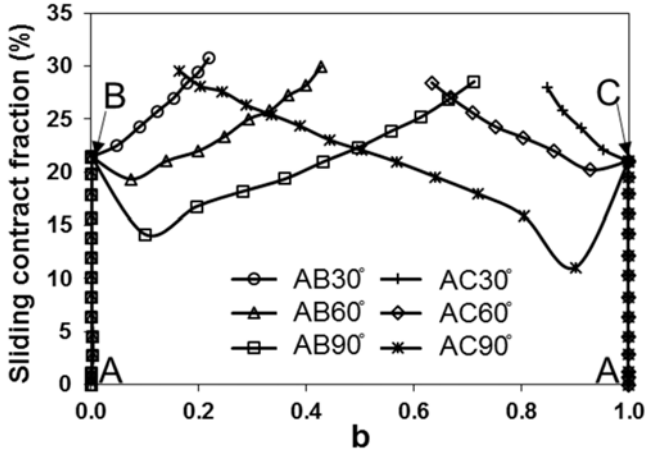

Fig. 4.16 Relationship between sliding contract fraction and the *b* value of continuously varying *b* tests.

4.3.6 Macro and Micro Relationship

Identifying the relationship between macro behavior and microscopic data under continuously varying b value is one of the main objectives of this study. Relationships between the macro and micro behavior have been explored previously using several approaches. For instance, Antony et al. (2004) (see Table 4.3.) reported the correlation between the macroscopic shear stress q/p and a single parameter related to the contact normal vector, pertaining to strong contacts between oval and circular particles in DEM simulations under a bi-axial compression test. Subsequently, Ng (2004b) showed that the principal stress ratio (σ_1/σ_3) could be correlated with the contact normal force more than the unit contact normal under different stress paths, under constant b value. Additionally, Sazzad et al. (2011) concluded the macro and micro relationships were not unique when considering all contacts, however, it became unique when considering the strong contacts. In the present study, a single parameter of a unit normal vector was used, as used by Antony et al. (2004) and Sazzad et al. (2011).

Figs. 4.17(a) through 4.17(d) represent the macro behavior using q/p and the micro response using the deviatoric fabrics of all contacts ($F_{11} - F_{33}$) (see Eq. 2.4) and of the strong contacts ($F_{11}^s - F_{33}^s$) (see Eq. 2.5) under constant b and continuously varying b tests, respectively. The macro and micro relationship in all contacts shows no specific trend for all tests in Figs. 4.17(a) and 4.17(c). The macro behavior changes along with the micro response. Similar results for constant b tests were reported by Antony et al. (2004) and Sazzad et al. (2011). Comparatively, good correlation is observed when only the strong contacts are considered in Figs. 4.17(b) and 4.17(d). The strong contacts seem not be influenced by the stress ratio. In addition, it is seen from Fig. 4.17(c) that the deviatoric fabric tensors for all contacts are rotated toward the directions of the stress paths at points B and C. It is evident that new fabric contacts in the direction of the maximum compression stress are formed at points B and C. These new contacts formed in a new column-like loading path in the direction of the stress increment, and are linked to stress-induced anisotropy (Oda et al., 1985).

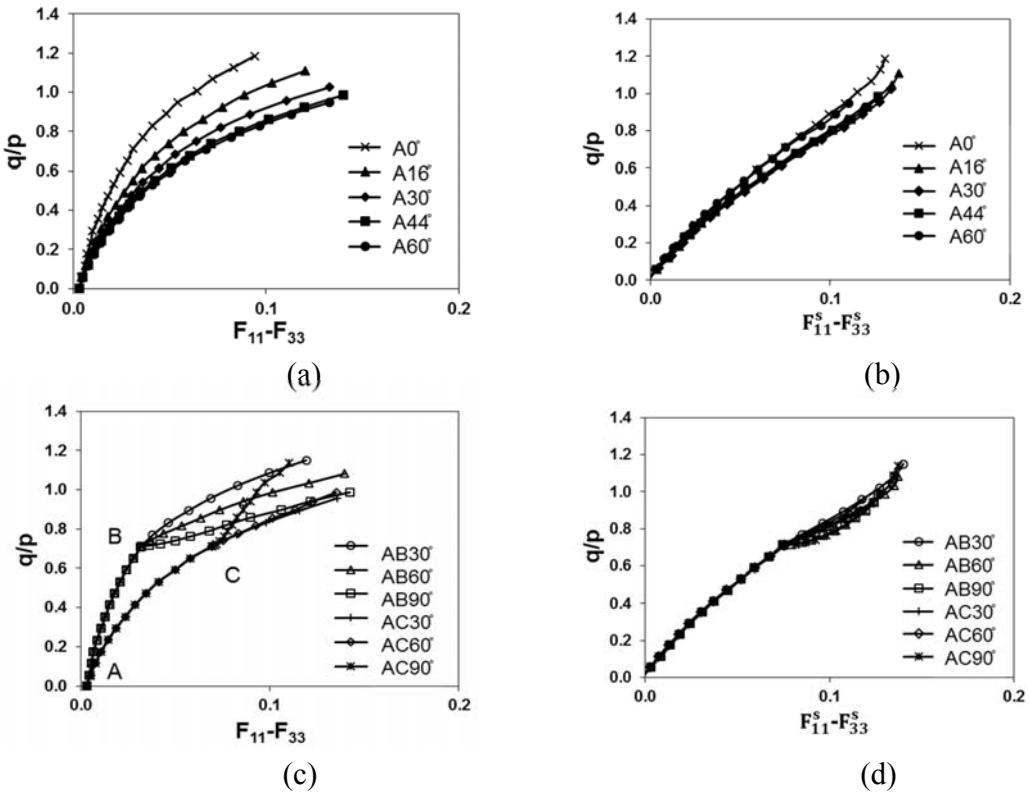

Fig. 4.17 Macro and micro relationship considering all contacts (F_{11}-F_{33}) and strong contacts ($F_{11}^{s} - F_{33}^{s}$) of all tests.

Chapter 5 Stress-Force-Fabric Evolutions of Granular Materials under Continuously Varying *b* Value

5.1 Introduction

Granular materials such as sand or gravel are a setup of discrete particles which have contact forces interacting at the contact points between them when shearing is applied. In particular, shearing deformation of the granular assembly causes a change in the magnitude of contact forces, in the number of load carrying contacts, distribution of contact forces, and contact orientation at the particle level. The micromechanical aspects from microscopic parameters to macroscopic behaviors have been researched to describe the particle mechanism with physical model experiments (Dantu, 1957; De Joeeslin de Jong and Verruijt, 1969) as well as with the numerical simulations using Discrete Element Method (DEM) (Cundall and Strack, 1978; Chantawarangul, 1993; Sitharam, 1999; Sitharam, 2002).

A non-dimensional parameter $b = (\sigma_2 - \sigma_3)/(\sigma_1 - \sigma_3)$ created by Habib (1953) where σ_1 σ_2, and σ_3 are major, intermediate and minor stresses, respectively. The b value is an intermediate stress ratio describing the influence of intermediate stress σ_2 in the general stress system. Several experiments and simulations had been conducted to study the influence of σ_2 on the macro behavior of sand among different stress paths. It was concluded that the macro behavior differs depending on the b value. (e.g., Matsuoka and Sun 1995; Suzuki and Yanagisawa 2006; Chantawarangul 1993; Sazzad et al. 2011; Phusing et al. 2015). For example, Matsuoka and Sun (1995) tested on sands under continuously varying b value stress paths and explained that the direction of strain increment vectors was influenced by the stress increment direction. Furthermore, Suzuki and Yanagisawa (2006) experimented on sands having different levels of inherent transverse isotropy under constant b value stress paths. They explained that strain increment direction deviates stress increment direction while increasing equivalent deviatoric strain.

The study of micromechanical response under constant b values had been studied using the discrete element method (DEM) by Chantawarangul (1993). Chantawarangul (1993) researched on the micromechanical responses of granular materials using spheres under monotonic loading stress paths with five constant b values (b = 0.0, 0.25, 0.5, 0.75, and 1.0). He reports that the deviator stress resistance of the assembly, indicating the macro behavior, can be expressed by anisotropy coefficients from micro scale level when $\sigma_1 \neq \sigma_2 \neq \sigma_3$ and b value is constant. The anisotropy coefficients are dependent on the b value. The anisotropic coefficient of contact normal forces decreases with the increase of b value which is in contrast to the anisotropic coefficient of contact orientation. Furthermore, the anisotropic coefficient of contact normal forces shows significant role in defining the shear resistance of granular materials.

The literature above illustrates that DEM simulations of the micromechanical responses had generally been conducted with a constant b value. Nevertheless, actually, the stress path normally changes the direction in the stress space, which causes the change in b value. The study of macro behaviors and macro-micro relationship of granular materials under continuously varying b value stress paths have been studied by Phusing et al. (2015). They described that the direction of strain increment vector depends on the direction of stress increment vector and on the approximate failure surface. Additionally, the direction of strain increment vector is influenced by b value, under continuously varying b stress path. Regarding the macro-micro relationship, Phusing et al. (2015) found that the unique relationship between macro and micro behaviors was found only when the strong contacts were under continuously varying b stress paths.

Even though, the macro-micro relationship was researched, the micromechanical behaviors of granular materials under continuously varying b value stress paths had been rarely reported. Therefore, the micromechanical behavior and the anisotropic coefficients at micro level of granular materials under continuously varying b value stress paths need to be explained more deeply for the geotechnical engineering. Hereafter, Constant b Value stress path and continuously Varying b value Stress paths are abbreviated to be CbV and VbS.

There are two objectives in this paper. Firstly, we investigated the development of anisotropic coefficients of contact orientation, normal contact forces, tangential contact forces and microscopic processes of three-dimensional assemblies under continuously varying b value

stress paths (VbS). Second, we investigated the relationships between stress, strain and the parameters, obtained by DEM, that characterize microstructure and applied stresses under continuously varying *b* value stress paths (VbS). To fulfill the objectives, 8,000 spheres were used for simulations under VbS. An open-source DEM software, called Oval (Kuhn, 2006), was used. The simulation was made by a constant mean stress of 100 kPa using stress-controlled method. The principal stresses were set by changing the stress rate to increase or decrease stress in the simulation. The method to input stress rates is explained in Phusing and Suzuki (2015). The micromechanical behaviors and development of microscopic parameters under VbS were both analyzed. Moreover, we made a qualitative comparison between the stress-strain relationship from DEM, and the one from the stress-force-fabric (Rothenburg 1980) under VbS.

5.2 Sample preparation and simulation program

A sample was modeled using 8,000 spheres of different diameters between 3 - 4.5 mm. The initial configuration of the sample is a 10.5×10.5× 10.5 cm^3size. After isotropic compression of 100 kPa, the sample size was reduced to 7.1×7.1× 7.1 cm^3 and had a void ratio of 0.57, indicating the medium dense assembly. During isotropic compression, the interparticle friction angle is equal to 0.3. The stress-controlled method under a constant mean stress p = 100 kPa was used. The constant mean stress condition was set because the different mean stresses under different stress paths could probably affect the results. The input parameters are summarized in Table 5.1.

After the isotropic compression, the sample was sheared under five constant *b* values (CbS) (b = 0.0, 0.3, 0.5, 0.7, and 1) and three continuously varying *b* values stress paths (VbS) named AB30°, AB60°, and AB90°. The numbers after AB show the angle of deviation measuring from the major principal stress σ_1 in an anticlockwise direction. Fig. 5.1 shows the projection of those eight stress paths on the normalized π-plane. These eight stress paths start from point A where σ_1, σ_2, and σ_3 are 100 kPa and the stress ratio q/p are zero. The five CbS were performed for the monotonic loading. The other three VbS were tested from point A to B where q/p =0.42. Each follows the different direction, as shown in Fig. 5.1.

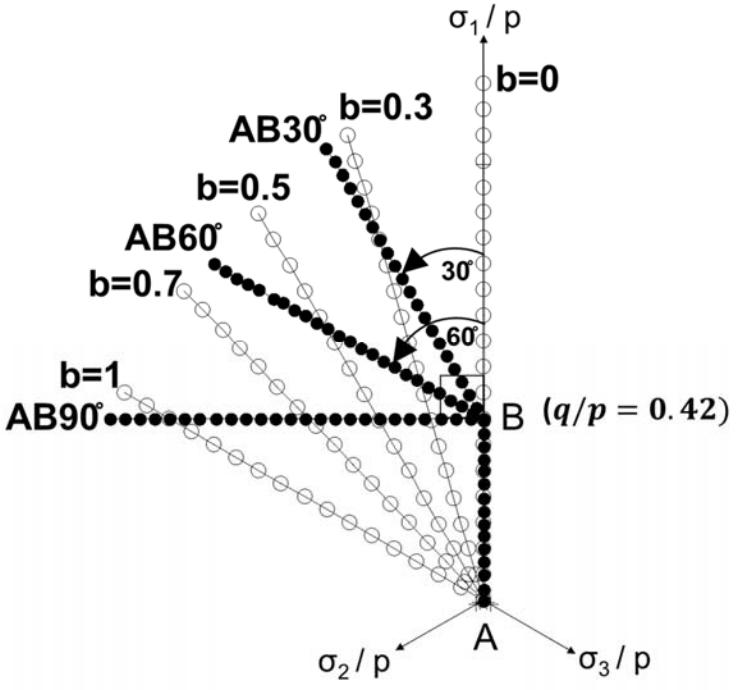

Fig. 5.1 Simulating stress paths on the normalized π-plane

Fig. 5.2 shows that the mean stress p was constant during the simulation in all tests, where the equivalent deviatoric stress q increases.

Fig. 5.3 shows the relationship between the intermediate stress ratio b value and the equivalent deviatoric strain $\varepsilon_d(\%)$ of stress paths in Fig. 5.1. Fig. 5.3 shows that b value remains constant throughout CbS simulation. Speaking of VbS, Fig. 5.3 shows that b value is constant ($b = 0$) from point A to B, then, increases up to 0.33, 0.63 and 1.10 for AB30°, AB60°, and AB90°. The final b value of AB90° is greater than 1.0 because the σ_2 at the final point of stress path AB90° is higher than σ_1 and σ_3. As a result, this study conducted the varying b values from $b = 0$ to $b = 1.1$. The method to change each stress rate for these directions is used in Phusing and Suzuki (2015). In order to remain quasi-static and stable, the simulation was terminated when the unbalanced force index I_{uf} reached 1% (Kuhn 2006; Ng 2006). In this study, positive value represents the compression of stress and strain, while a negative value represents the tension of stress and strain dilation.

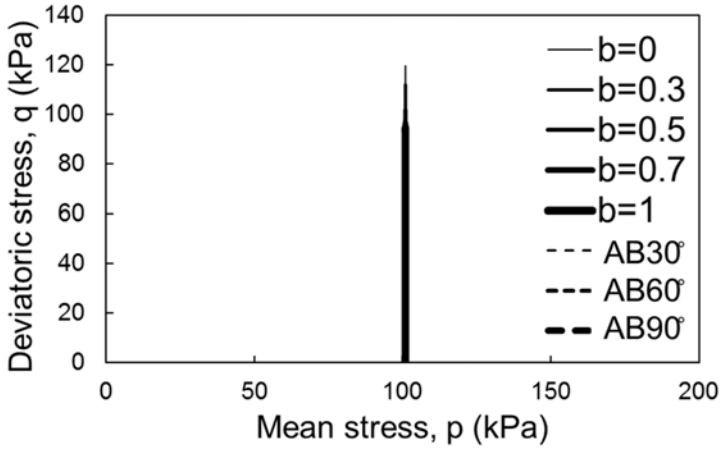

Fig. 5.2 *q-p* stress paths of all tests

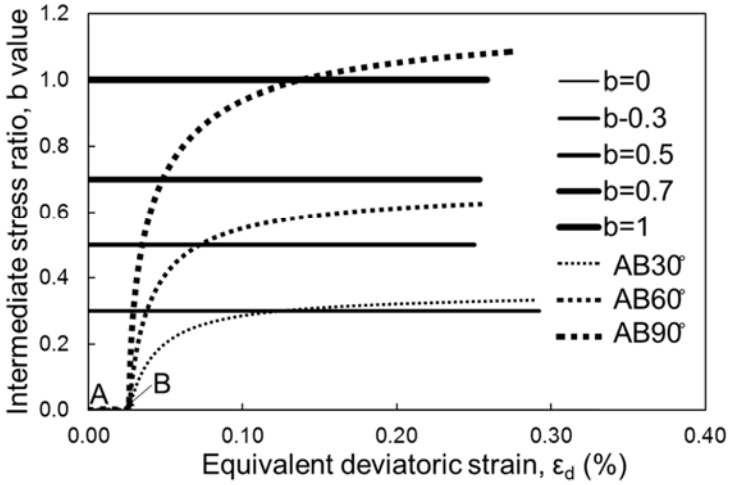

Fig. 5.3 Relationship between *b* value and equivalent deviatoric strain $\varepsilon_d(\%)$ of all tests.

5.3 Results

5.3.1 Stress-strain-dilation

Figs 5.5(a) and (b) show the relationship between stress, strain, and dilation of CbS and VbS. The Figs show that the stress-strain-dilation curves vary depending on stress paths on π-plane. The stress path b = 0 in CbS gave the maximum stress ratio q/p with the minimum dilation when ε_d increases. However, at last, dilation is maximum under stress path b = 0. In contrast, b = 1 contrasts. The result is similar to the experiment on sand under different levels of inherent transverse isotropy with CbS in Suzuki and Yanagisawa (2006). As for DEM simulations on a dense sample under CbS, Thornton (2000), Sazzad et al. (2011) and Phusing et al. (2015) concluded similarly. Then, VbS finding is verified by the laboratory observations of Matsuoka and Sun (1995) who used cemented sand. It is worth noting that the intermediate stress σ_2 regarding b value is one of main factors relating to the change in macro behavior of granular materials in stress-strain-dilation relation.

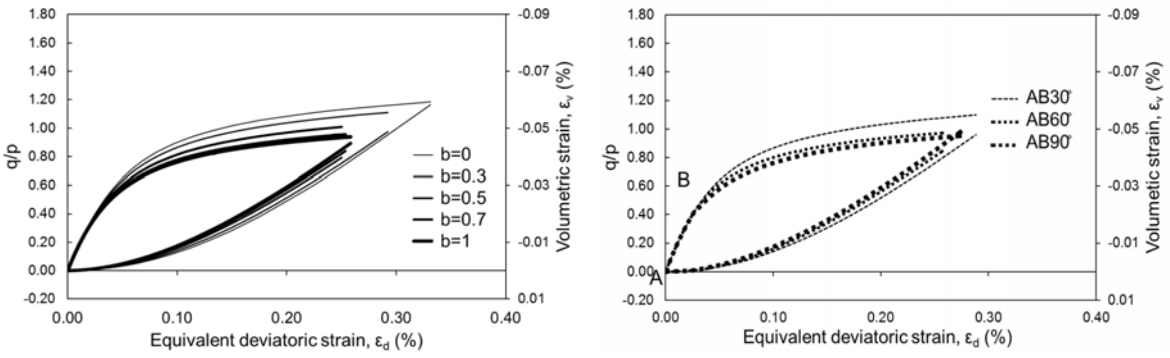

(a) (b)

Fig. 5.4 Stress-strain-dilation relationship under: (a) CbS and (b) VbS

The relationship between the angle of shearing resistance $\phi = \sin^{-1}\{(\sigma_{11} - \sigma_{33})/(\sigma_{11} + \sigma_{33})\}$ and b value of the final points on the stress-strain curves in Figs 5.5(a) and 5. (b) is shown in Fig. 5.6. The Fig. shows that the angle of shearing resistance ϕ is minimum when $b = 0$ but increases up to a certain value of b and then decreases when b approaches $b = 1$. The dot line in Fig. 5.6 indicates the general tendency of ϕ regarding the b value which is similar to the experimental results reported by Kumruzzaman and Yin (2012) as well as Rodriguez and Lade (2013) and DEM results by Sazzad et al. (2011) and Phusing et al. (2015) for CbS. The ϕ of final points of AB30° and AB60° in Fig. 6 come to an end on the dotted line. Additionally, the ϕ of final points of AB90° where $b = 1.1$ can be used to approximate the ϕ when $b > 1.0$. It is evident that the angle of shearing resistance ϕ at peak stress ratio does not depend on the changing direction of stress paths.

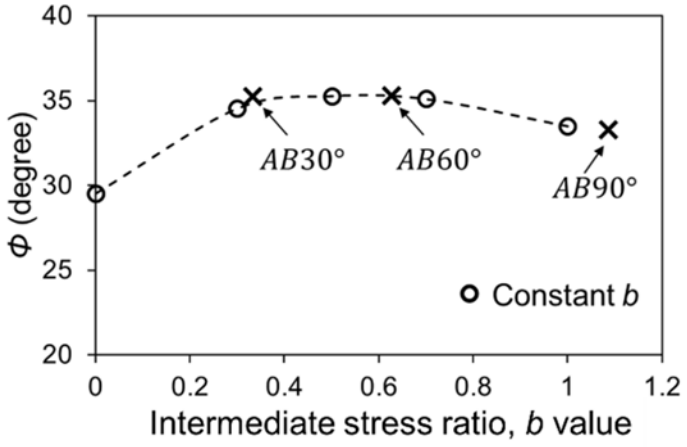

Fig. 5.5 The relationship between ϕ and b value

5.3.2 Micromechanical behaviors

Figs 5.7(a) and (b) show the development of coordination number and sliding contact fraction, with the equivalent deviatoric strain $\varepsilon_d(\%)$. They are the average micromechanical behaviors. Fig. 5.7(a) shows that the coordination number is maximum at the initial state and decreases once the increase of the equivalent deviatoric strain occurs. This shows the contacts loss while shearing because of the dilation. Seemingly, Fig. 5.7(a) shows that the coordination number is not dependent on the difference of stress paths in the dense sample. In Fig. 5.7(b), the sliding contact fraction shows a sudden drop under VbS, especially at point **B** of AB90°. At point **B**, some sliding particles stop sliding because of the missing of previous applied stresses in the direction of b = 0. Then, they start sliding again due to the new direction of applied stresses after point **B**. This result was reported previously by Phusing et al. (2015) using DEM with monotonic loading under VbS and Phusing and Suzuki (2015) under cyclic VbS.

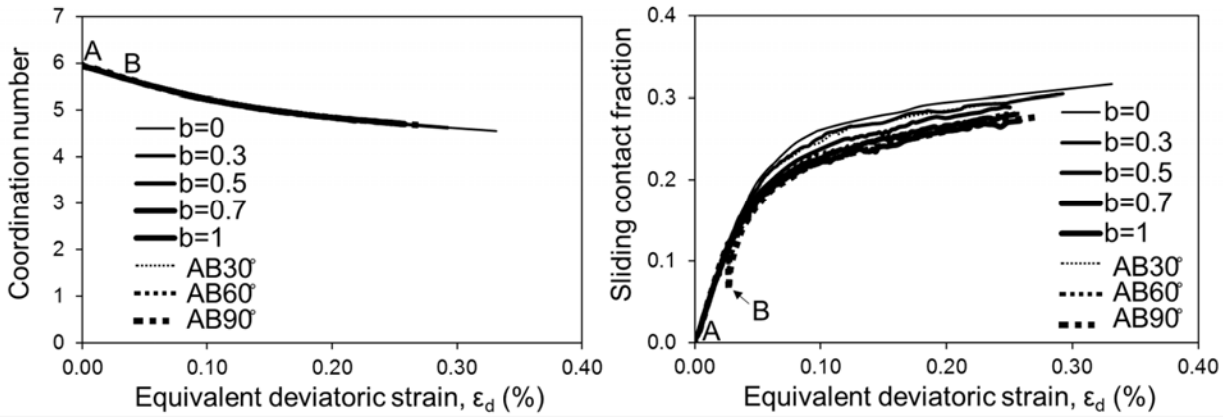

(a) (b)

Fig. 5.6 The relationship of CbS and VbS between (a) Coordination number and $\varepsilon_d(\%)$; (b) Sliding contact fraction and $\varepsilon_d(\%)$.

5.3.3 Stress-Force-Fabric Relationship

Figs 5.8(a) and (b) show the macroscopic stress ratio q/p and from stress–force–fabric relationship (Eq. 2.13) versus the equivalent deviatoric strain $\varepsilon_d(\%)$ under CbS and VbS. The Figs show a similar tendency between the macroscopic stress ratio obtained from the applied boundary stress using DEM (see Figs 5.5(a) and (b)). The quantity differences of q/p between DEM result in Figs 5.5(a) and (b) probably caused by using the average values of contact normals (fabric), normal contacts and tangential contacts in Eq. (2.13) instead of the actual values of those contacts. Possibly, there remains a problem.

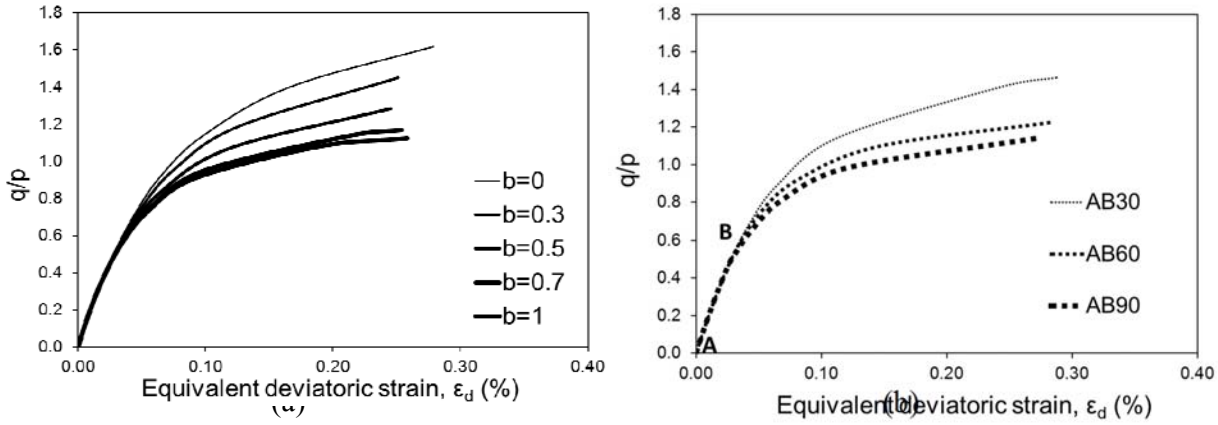

Fig. 5.7 The relationship between q/p and $\varepsilon_d(\%)$ from Stress-force-fabric relationship (Eq. 2.13): (a) CbS and (b) VbS.

5.3.4 Stress-Force-Fabric Evolutions

The stress-force-fabric evolutions of three dimensions have been reported by Bathurst (1985), Chantawarangul (1993), Sitharam (2002) that the distribution diagrams of average contact normals (fabric) and average normal contact forces are *spherical* distributions at the hydrostatic stress condition using Eq. (2.14) and (2.18) whereas the average tangential contact forces is approximately zero. Furthermore, while increasing the deviatoric stress, there is an increase in contact normal orientation and normal contact forces anisotropy. Chantawarangul (1993) showed the distribution diagrams of average contact normals (fabric) and average normal contact forces change from *spherical* to *peanut* shape distribution for stress path b = 0, and change to *donut without a hole* shape distribution for stress path b = 1. As for the distributions of the tangential contact forces, Chantawarangul (1993) reported that it develops in approximately 45° from the maximum stress in stress paths b = 0. The distribution shape looks like a *dumbbell*. In addition, the magnitude of tangential contact force is small compared to contact normal and normal contact force anisotropy (Chantawarangul 1993; Sitharam 2002). This study found the same result as shown in Figs. 5.8(a) and (b) for b = 0 as well as in Figs. 5.9(a) and (b) for b = 1. In Fig. 5.8(a), the distribution diagrams of average contact normals (fabric), average normal contact forces and average tangential contact forces are correspond to points **a** to **e** of stress path b = 0 in Fig. 5.8(b).

Regarding the result of VbS, Fig. 5.9(a) shows the distribution diagrams of average contact normals (fabric), average normal contacts and average tangential contacts corresponding to points **A** to **e** of stress path AB90° shown in Figs 5.9(b). It can be seen in the Figs that the distribution of average contact normals (fabric) and average normal contacts looks like *capsule* distributions at point **B**, then, start to become *donut (without a hole)* when b value varies from 0 (point **B**) to 1.1 (point **e**). Furthermore in Figs 5.9(a) and (b), the distribution of average tangential contact force develops approximately 45° from the maximum stress σ_1 at point **B** (b = 0) and shows a *dumbbell* in the vertical direction. Then, this distribution gradually changes to *dumbbell* in the horizontal direction at point ***e*** (b = 1.1) where the maximum stress is σ_2. This can

be concluded that changing the direction of the stress path causes not only changing the direction of the maximum stress but also the increment directions of those distribution diagrams.

From Figs 5.10(a) to (c), it shows the distributions of average contact normals, average normal contact forces and average tangential contact forces at peak of CbS and VbS stress paths. It can be seen in Figs 5.10(a), (b) and (c) that the distribution shapes at peak of average contact normals, average normal contact forces and tangential contact forces under VbS stress paths show the developments in the same trend to those distributions under CbS. This can be concluded that the distributions at the peak stress of average contact normals, average normal contact forces and average tangential contact forces do not depend on the stress path.

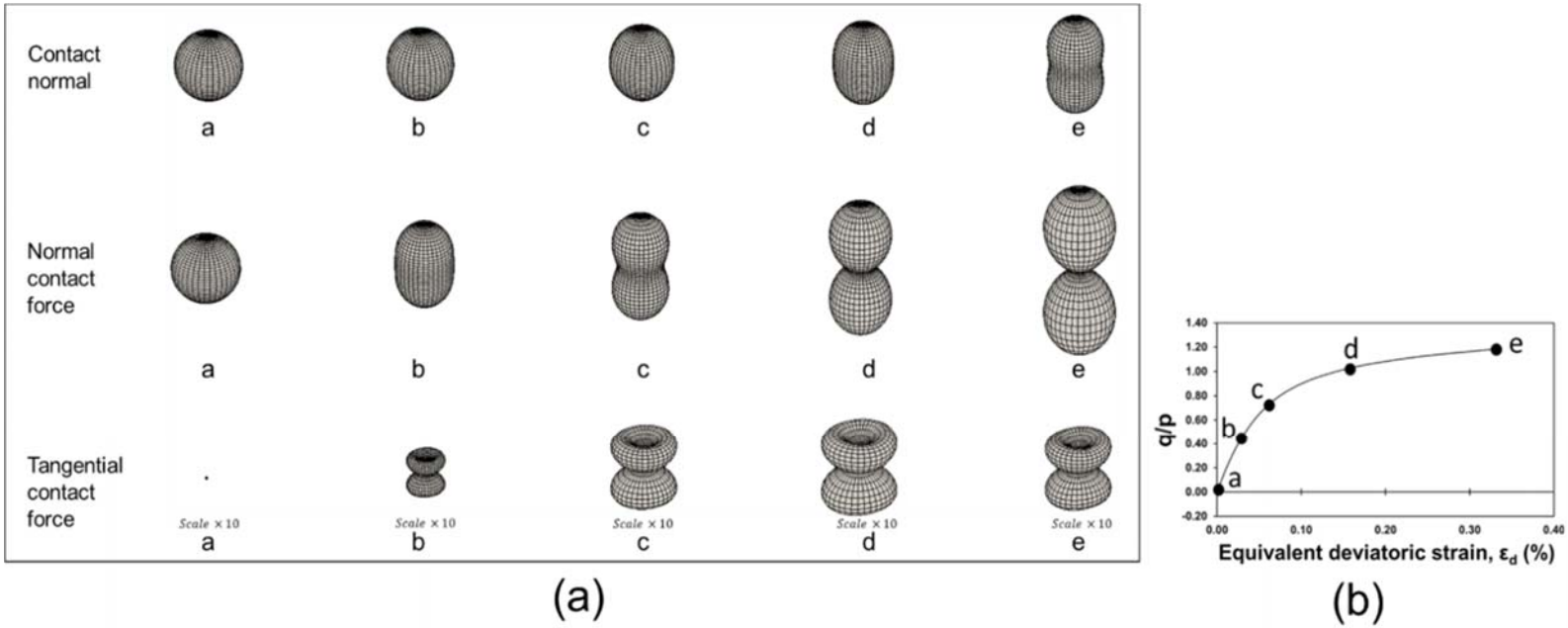

Fig. 5.8 (a) Distribution diagrams of average contact normals, average normal contact forces and average tangential contact forces corresponding (b) different stages of stress path b =0.

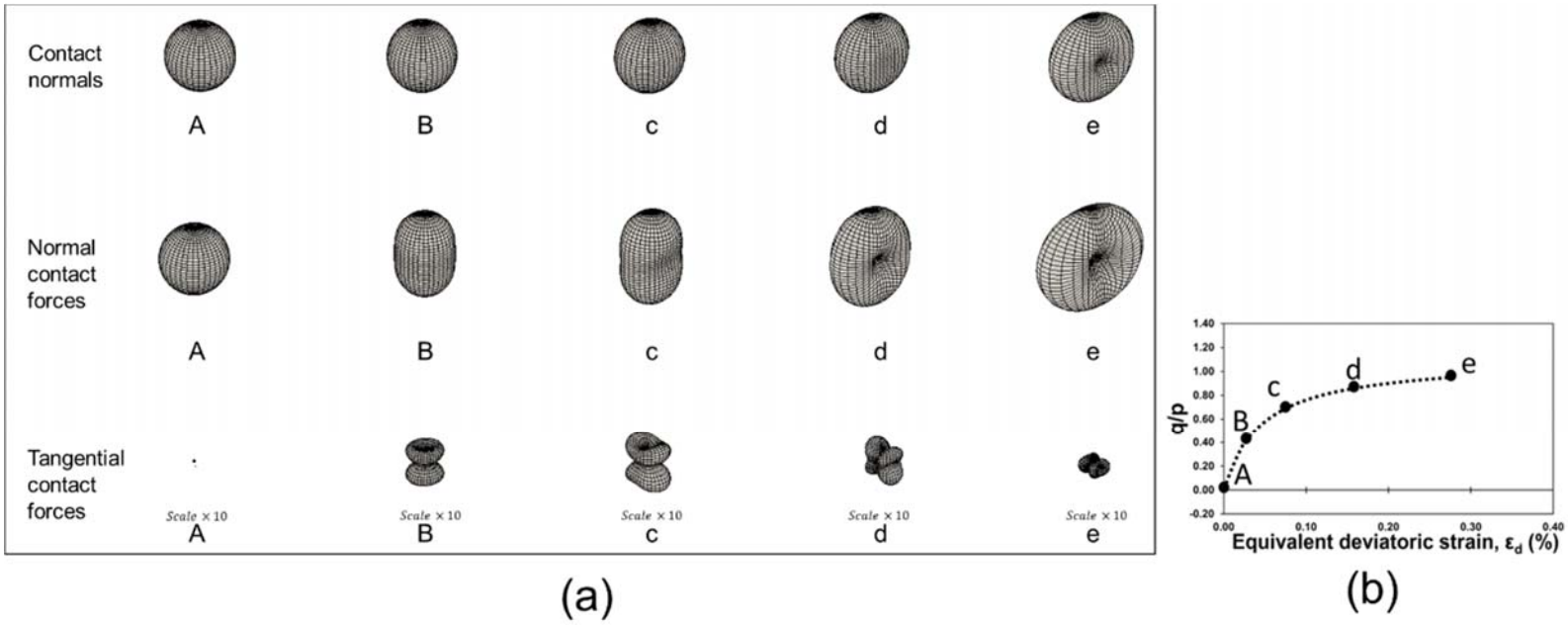

Fig. 5.9 (a) Distribution diagrams of average contact normals, average normal contact forces and average tangential contact forces corresponding (b) different stages of stress path AB90°.

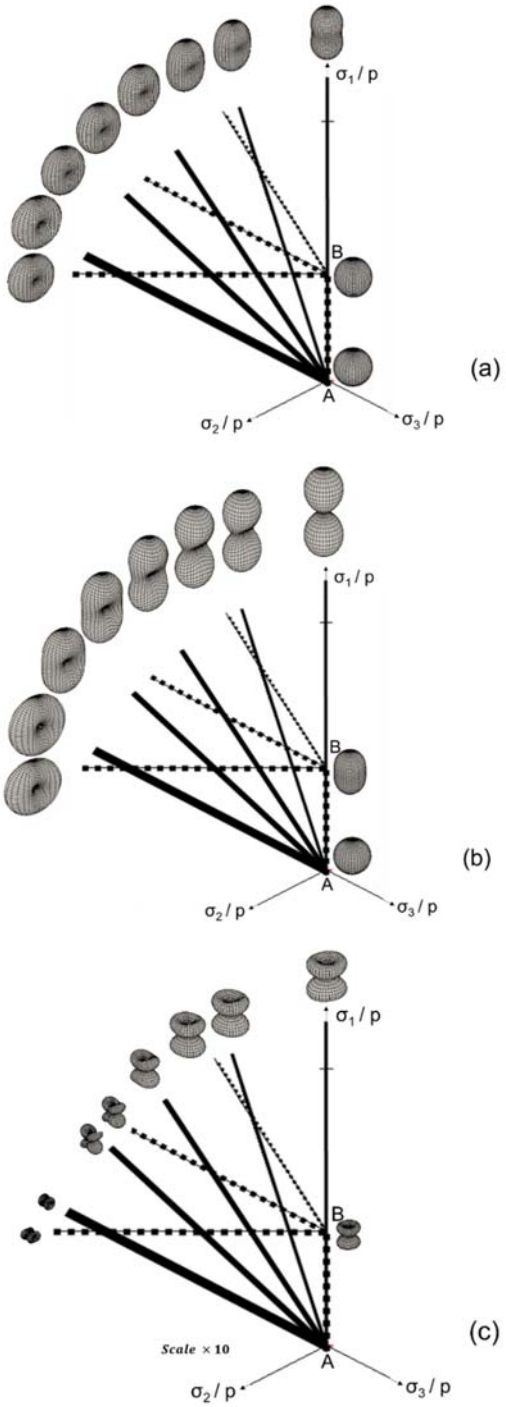

Fig. 5.10 The distribution diagrams at peak stress ratios of all stress parts: (a) average contact normals, (b) average normal contact forces and (c) average tangential contact forces.

5.3.4 Increment Vectors of Strain and Anisotropy Coefficients

Figs 5.11(a) - (d) show strain increment vectors and increment vectors of anisotropy coefficients of contact normals a_{ij}^{r}, normal contact forces a_{ij}^{n}, and tangential contact forces a_{ij}^{t}, superimposed on CbS and VbS stress paths. The Figs show that strain increment vectors and the increment vectors of those anisotropy coefficients differ depending on the location of stress path. The dependency of strain increment vectors on the stress path was reported by the experiment on sand of Matsuoka and Sun (1995) and DEM results of Phusing et al. (2015). Considering the increment vectors of those three anisotropy coefficients under VbS in Figs 5.11(b), (c) and (d), the increment vectors of those three anisotropy coefficients have changed their directions at point **B**. These changes is caused by the change of stress increment directions of at point **B** of stress path AB30°, AB60°, and AB90°. This indicates that changing the direction of stress paths changes not only the direction of stress increment vector and strain increment vector but also the increment vectors of contact normals (fabric), normal contact forces, and tangential contact forces.

5.3.5 Deviatoric Anisotropy Coefficient Evolutions

Figs 5.12(a) - (f) show the plot of induced deviatoric anisotropy coefficients a^{r}, a^{n}, and a^{t} (see Eq. 2.25) versus the equivalent deviatoric strain $\varepsilon_d(\%)$ regarding the b value under CbS and VbS. Fig. 5.13 shows the plot of a_r, a_n, and a_t versus b value at peak of CbS and VbS stress paths from Figs 5.12(a) - (f). In Fig. 5.13, the dotted lines show the variation of those coefficients with the levels of b value of five CbS while the points show those of the other three VbS. In Figs 5.12(a) and (b), the deviatoric coefficient of contact normal anisotropy a^{r} develops gradually to the maximum value. Further, the deviatoric coefficients of normal contact force anisotropy a^{n} and tangential contact force anisotropy a^{t} increase monotonically with the equivalent deviatoric strain in Figs 5.12(b) - (f) in both CbS and VbS. Additionally, the deviatoric normal contact force anisotropy a_n has a great influence on the stress ratio because

it shows the similar tendency with stress-strain relationship regarding b value (see Figs 5.5(a) and 5.5(b)). The deviatoric tangential contact force anisotropy a^t increases rapidly at low levels of equivalent deviatoric strain. Its effect is minor at higher levels. These Figs highlights the evolutions of induced anisotropy coefficients on the strength of granular assembly.

Considering the evolution of a^r regarding the different b value in Fig. 5.12(a), the peak deviatoric coefficients of fabric anisotropy a^r increase together with b value. This indicates that b value has an effect to the particle orientations. The small value of a^r indicates less reorientation of particles whereas the large one indicates more. When increasing in deviatoric stress under stress path b = 0, the vertical principal stress $\sigma_1$is increased while the other two horizontal σ_2 and σ_3 are decreased. The contact normal vectors and normal contact force vectors in σ_1 direction increase where those in σ_2 and σ_3 directions has been lost. This corresponds to the *peanut* shape distribution of contact normals and normal contacts shown in Fig. 5.8(a). In Fig. 5.12(b), the stress path b = 0 has higher deviatoric coefficient of normal contact force anisotropy a^n than the other CbS as well as VbS at all levels of ε_d. This implies that the assembly under stress path b = 0 carries a higher magnitude of deviatoric normal contact force a^n at all levels of ε_d. In contrast, the deviatoric contact normals (fabric) anisotropy a^r of stress path b = 0 shows the smaller number. This indicates the less reorientation of the particles in the assembly.

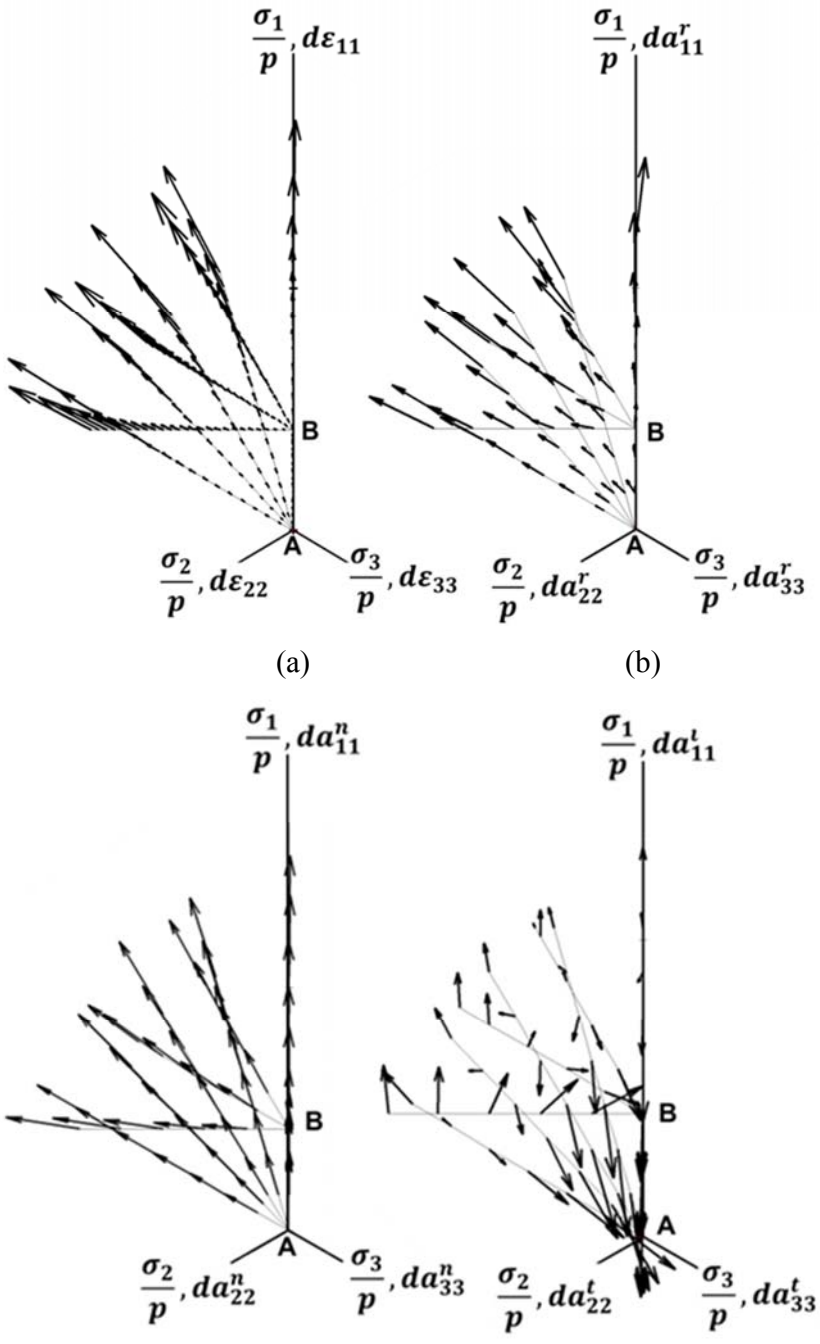

Fig. 5.11 Directions of increment vectors on the normalized π-planes of; (a) strain increment, (b) da^r_{ij}, (c) da^n_{ij} and (d) da^t_{ij}.

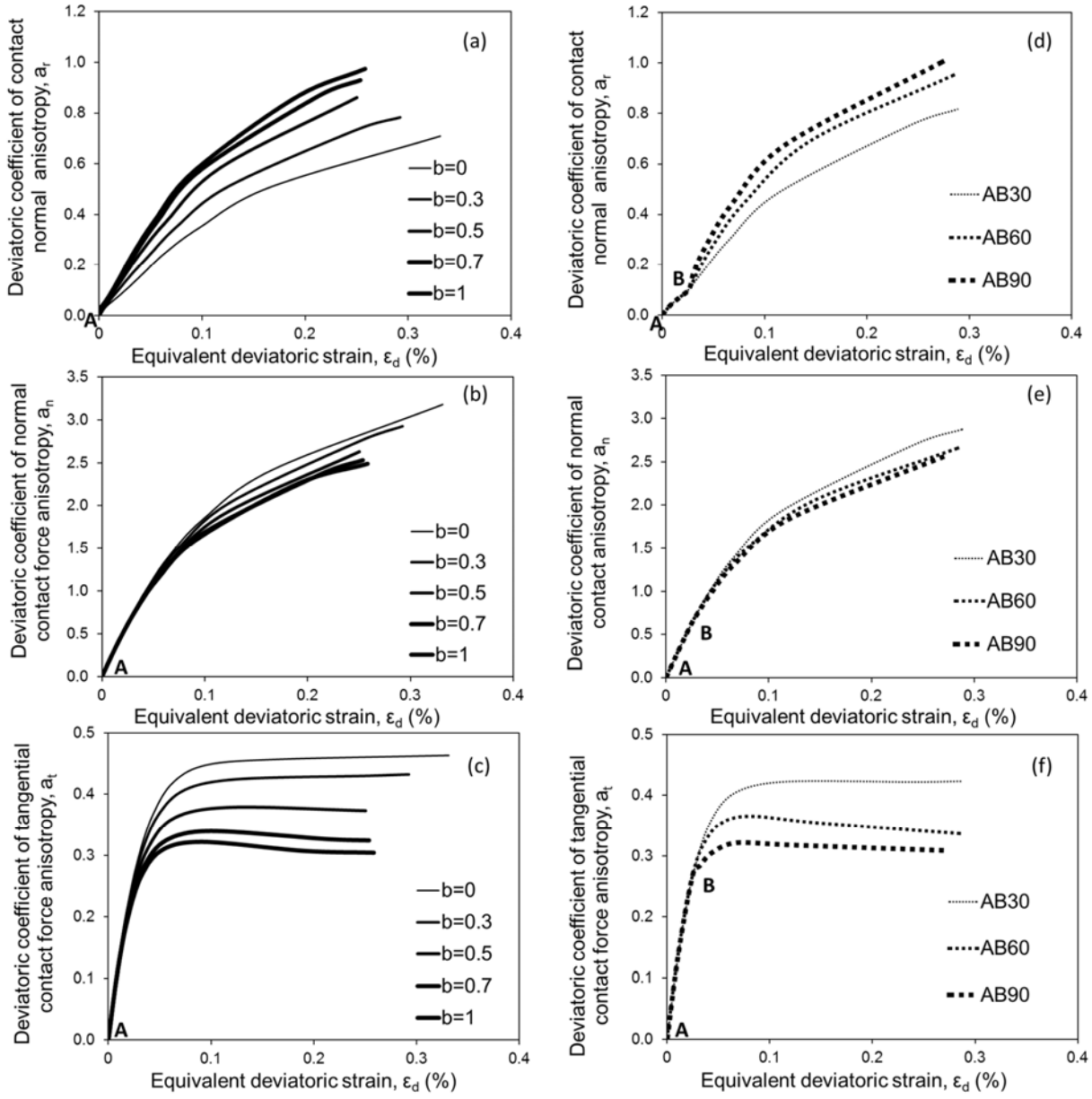

Fig. 5.12 The relationship between a_{ij}^r, a_{ij}^n, a_{ij}^t and ε_d(%) under CbS and VbS

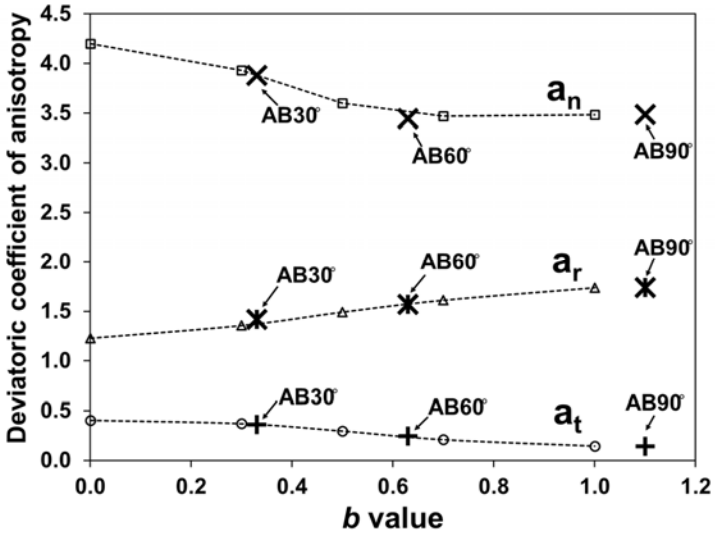

Fig. 5.13 The relationship between the deviatoric coefficients of anisotropy and *b* value

Regarding the results of VbS in Fig. 5.12(d) - (e), the directions of increment vectors of a^r, a^n and a^t changed at point **B**, corresponding to the degree of changing direction of stress path AB30°, AB60°, AB90°. However in Fig. 5.13, it can be seen that a^r, a^n and a^t of AB30°, and AB60° exactly come to an end on the dotted lines of CbS. Also, the points of the a^r, a^n and a^t of AB90° can be assumed on the extended dotted line. It is worth noting that the degree of changing direction of stress paths has influence on the increment vectors of anisotropy coefficients of contact normals, normal contact forces and tangential contact forces and on increment vectors of strains in experiments as well. However, the degree of anisotropy coefficients of those anisotropy coefficients do not depend on the stress path at peak stress.

Chapter 6 Cyclic Behaviors of Granular Materials under Generalized Stress Condition

6.1 Introduction

The mechanical behaviors of granular materials under cyclic loading tests have been investigated by many experimental tests as well as numerical simulation methods. (Tatsuoka & Ishihara 1974; Nakai et al., 1996; Nakai et al., 2001; Nakai et al., 2003). As for the experimental results, Tatsuoka and Ishihara (1974) applied cyclic triaxial compression and extension with constant stress amplitude on loose and dense sand and found that the hysteresis loop in the first cycle is the greatest, but later it becomes smaller indicating that the sand has ranged an elastic deformation stage. Furthermore, Nakai et al. (1996), Nakai (2001) and Nakai et al. (2003) tested under cyclic loading on medium dense Toyoura sand with various stress amplitudes as well as various stress paths. They concluded that dilative characteristics of sand during cyclic loading depend heavily on the initial stress ratio, even though its amplitude and number of cycles are the same.

Using DEM, many cyclic loading tests of granular materials have been performed to investigate mechanical behaviors such as the macro behavior and the micromechanical response (Hu et al., 2010; Sitharam 2003; Sitharam et al., 2002; Thornton & Antony 1998). For example, Hu et al. (2010) reported that the amplitude of the cyclic loading can influence the strain accumulation as well as the evolution of an anisotropic fabric in the soil. Furthermore, Sitharam (2003) reported that during cyclic loading compression and extension of a shear stress, the nearly total loss of resistance to shear, with remaining small number of contact forces (e.g. coordination number), led to a large decrease of the volume of granular materials. In addition, Thornton and Antony (1998) reported on the compression and extension simulations on a soft particle system and found that the shear strength was mainly due to strong force fabric structure, and the weak fabric structure's influence to shear strength was very small.

According to the DEM simulation under cyclic loading, most of the behaviors of granular materials have been proposed under limit conditions of stress paths such as a triaxial compression and extension cyclic loading. The macro behavior and the micromechanical response of granular materials under cyclic loadings in more comprehensive stress conditions are not well understood. The present study aims to know how granular materials behave under the various cyclic stress paths in the generalized stress condition. This paper have two objectives. The first is to ensure the ability of the Discrete Element Method (DEM) to simulate the macro behavior of granular materials under various cyclic stress paths in the generalized stress condition. The second is to explore the micromechanical responses of those granular materials. A DEM software, named Oval (Kuhn, 2006), is used as a numerical simulation for this purpose. This study conducts four different cyclic loading stress paths under generalized stress simulations with constant mean stress and the stress-controlled method. Experimental results are used for qualitative comparison with the results of DEM. The results are analyzed. Finally, the macro-micro relationship is explained.

6.2 Sample preparation and isotropic compression

A cubical sample was formed in three-dimensional space with three directions of principal stresses ($\sigma_1, \sigma_2, \sigma_3$) as shown in Fig. 6.1. In this study, σ_1 and ε_1 indicate the vertical direction of the stress and strain, respectively whereas σ_2, σ_3 and $\varepsilon_2, \varepsilon_3$ indicate those in the horizontal directions. In Fig. 6.2(a), the 8,000 spheres of 16 different sizes of diameters 3-4.5 mm. were randomly placed within the cubical sample. The Fig. shows that the distance between each sphere is 5 mm. and the initial cubical sample is a size of 10.5× 10.5× 10.5 cm^3. The sample preparation in this study followed the sample preparation of Sazzad et al. (2011). The periodic boundary was used as the boundary condition in order to eliminate the effects of boundary on the sample to use a small number of particles as a representative (O'Sullivan, 2011). In Fig. 6.2(b), the isotropic compression was applied. In this study, a positive value of stress and strain indicates compression, while a negative value indicates extension.

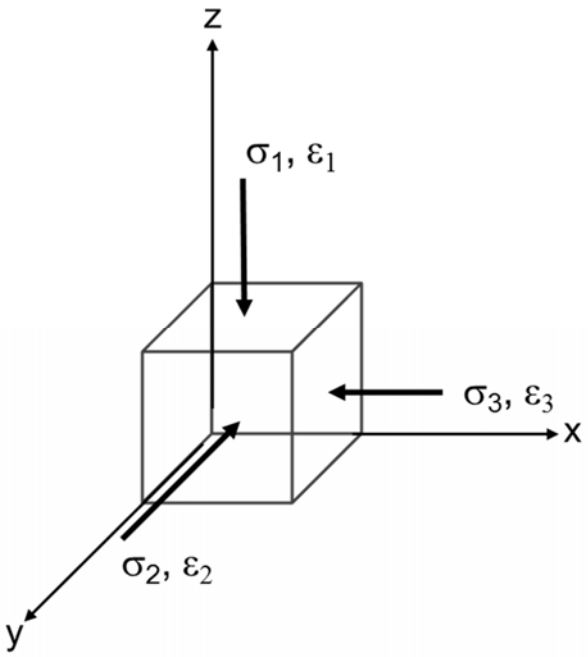

Fig. 6.1 A cubical sample with three principal stresses

For isotropic compression, a strain- and a stress-controlled are used as first and second stages , respectively (see strain ε̇ and stress rate σ̇ in Table 6.1). The strain-controlled loading method was first used for getting particles quickly close to each other and generate enough number of contacts to form the fabric structure. Using purely stress-controlled loading, the number of contacts was generated very slowly and the simulation was terminated during first stage of isotropic compression because of not enough number of contacts.

Therefore, in first stage, principal strain rates $\dot{\varepsilon}_1$, $\dot{\varepsilon}_2$ and $\dot{\varepsilon}_3$ of 100%/sec each were applied until the principal stress σ_1, σ_2, and σ_3 were 13 kPa. Then, the second stage, principal stress rates $\dot{\sigma}_1$, $\dot{\sigma}_2$ and $\dot{\sigma}_3$, of 10^6 Pa/sec each were used until the principal stress σ_1, σ_2, and σ_3 were 100 kPa. The inter-particle friction coefficient μ in isotropic compression was set at 0.2. A time increment of 10^{-6} sec was used in both stages. The DEM input parameters for isotropic compression can be seen in Table 6.1. Finally, the sample before shearing had a void ratio e_0 = 0.67, coordination number = 4.88, and the size of 7.2× 7.2× 7.2 cm^3 as shown in Fig. 6.2(c).

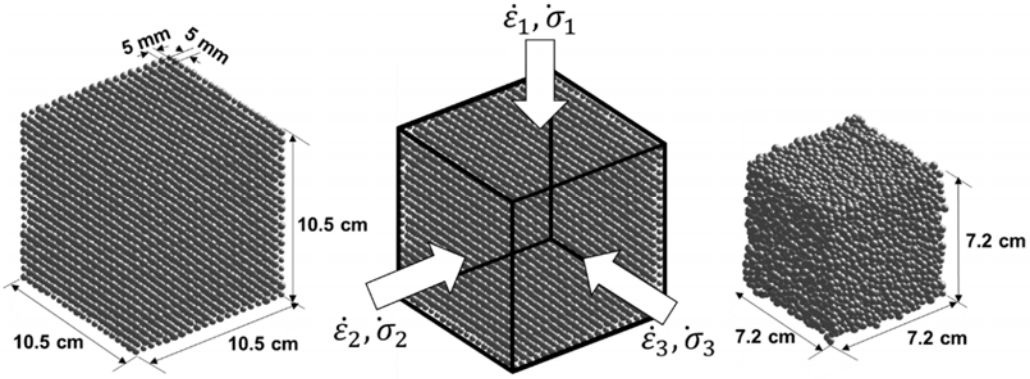

(a) Before isotropic compression

(b) During isotropic compression

(c) After isotropic compression

Fig. 6.2 Sample preparation and isotropic compression

6.3 Simulation Program

After isotropic compression, the sample were sheared under four cyclic stress paths on the Π plane, named Test 1, Test 2, Test 3, and Test 4, using the stress-controlled method under a constant mean stress p = 100 kPa as shown in Figs. 6.3(a)- 6.3(d), respectively. All stress paths start from point A where $\sigma_1, \sigma_2, \sigma_3$ = 100, 100, 100 kPa (after isotropic compression) following the directions and maximum stress amplitude is σ_1/σ_3 = 1.63. The simulation program in this study follows a part of an experimental program of Nakai et al. (2003). For Test 1, the sample was sheared under the triaxial compression and extension cyclic loading following stage ① and②, respectively (see Fig. 6.3(a)). In Test 2, the cyclic stress path is also the triaxial compression and extension loading, however, the major principal stress was changed from σ_1 to σ_2, and later $\sigma_2$to σ_3 following stage ①to ⑥(see Fig. 6.3(b)). For Test 3 (Fig. 6.3(c)), the unconventional cyclic stress path in a shape of a triangle following stage ①to ④ in the

anticlockwise direction was used. Finally, Test 4 is another unconventional cyclic stress path which similar to a shape of Mohr-Coulomb's criterion following stage ① to ⑦ in the anticlockwise direction (see Fig. 6.3(d)). All tests were repeated for 5 cycles. The 5 cycles was choose following the experimental results of Nakai et al. (2003).

Furthermore in Figs. 6.3(a) - 6.3(d), the direction of stress increments $\theta_{\dot{\sigma}}$ of each test are shown. Initially, Suzuki & Yanagizawa (2006) reported that the $\theta_{\dot{\sigma}}$ can be measured from the major principal stress σ_1 in an anticlockwise direction in one-sixth regions of the Π plane where $0^{\circ} \leq \theta_{\dot{\sigma}} \leq 60^{\circ}$ (see Fig. 6.4(a)).

In this study, the $\theta_{\dot{\sigma}}$ in all regions on the Π plane needs to be defined. This study found that the $\theta_{\dot{\sigma}}$ defined by Eq. (4.6) can be used also in the other regions of the Π plane. However, the Π plane has to be divided into four regions as shown in Fig. 6.4(b). Furthermore in Fig. 6.4(b), the $\theta_{\dot{\sigma}}$ can be measured from $+\boldsymbol{Y}'$ or $-\boldsymbol{Y}'$ axes where $0^{\circ} \leq \theta_{\dot{\sigma}} \leq 90^{\circ}$ in the anticlockwise direction in region One and Three, and $0^{\circ} \geq \theta_{\dot{\sigma}} \geq -90^{\circ}$ in the clockwise direction in region Two and Four.

For the simulation program in this study, the directions of stress increment $\theta_{\dot{\sigma}}$ on the Π plane in Figs. 6.3(a) - 6.3(d) were set using Eq. (4.6) and the diagram in Fig. 6.4(b). Table 6.2 shows the input stress rates ($\dot{\sigma}_1$, $\dot{\sigma}_2$, $\dot{\sigma}_3$) of all stages of all tests of four simulation programs regarding the stress paths in Figs. 6.3(a) - 6.3(d). For example, the input stress rate in stage ① of Test 1 is set as a compression stress rate $\dot{\sigma}_1 = +2 \times 10^6$ Pa and extension stress rates $\dot{\sigma}_2 = \dot{\sigma}_3 = -1 \times 10^6$ Pa (see Table 6.2). These stress rates contribute $b_{\dot{\sigma}} = 0$ and $\theta_{\dot{\sigma}} = 0^{\circ}$ by Eq. (4.6). Later, using the diagram in Fig. 6.4(b), when $\dot{\sigma}_1 > \dot{\sigma}_2 = \dot{\sigma}_3$ and $\theta_{\dot{\sigma}} = 0^{\circ}$, the stress path is in the direction of $+\boldsymbol{Y}'$ axis for compression loading. Then, in stage ② of Test 1, the $\dot{\sigma}_1 < \dot{\sigma}_2 = \dot{\sigma}_3$ generates $b_{\dot{\sigma}} = 0$ and $\theta_{\dot{\sigma}} = 0^{\circ}$ which contribute the stress path is in the direction of $-\boldsymbol{Y}'$ for extension loading. Another example is Test 3 (See Fig. 6.3(c)). The $\theta_{\dot{\sigma}} = -30^{\circ}$ in stage ②of Test 3 in Table 2 is measured from $-\boldsymbol{Y}'$ axis where $\dot{\sigma}_2 > \dot{\sigma}_3 > \dot{\sigma}_1$ in region Two in Fig. 6.4(b). The other stages of the other tests are also distributed by the same method. Fig. 6.5 shows that the simulated mean stress p is constant for all tests.

Table 6.1 Stress Rates for Shearing

Test	Stage	$d\sigma_1$ (Pa)	$d\sigma_2$ (Pa)	$d\sigma_3$ (Pa)	$b_{d\sigma} = \frac{d\sigma_2 - d\sigma_3}{d\sigma_1 - d\sigma_3}$	$\theta_{d\sigma}$ (degree)
1	1	$+2 \times 10^6$	-1×10^6	-1×10^6	0	0
	2	-2×10^6	$+1 \times 10^6$	$+1 \times 10^6$	0	0
2	1	$+2 \times 10^6$	-1×10^6	-1×10^6	0	0
	2	-2×10^6	$+1 \times 10^6$	$+1 \times 10^6$	0	0
	3	-1×10^6	$+2 \times 10^6$	-1×10^6	∞	-60
	4	$+1 \times 10^6$	-2×10^6	$+1 \times 10^6$	∞	-60
	5	$+1 \times 10^6$	$+1 \times 10^6$	-2×10^6	1	60
	6	-1×10^6	-1×10^6	$+2 \times 10^6$	1	60
3	1	$+2 \times 10^6$	-1×10^6	-1×10^6	0	0
	2	-2×10^6	$+2 \times 10^6$	0	-1	-30
	3	0	-2×10^6	$+2 \times 10^6$	2	90
	4	$+2 \times 10^6$	0	-2×10^6	0.5	30
4	1	$+2 \times 10^6$	-1×10^6	-1×10^6	0	0
	2	-1×10^6	$+1.25 \times 10^6$	-0.25×10^6	-2	-40
	3	-1.25×10^6	$+1 \times 10^6$	$+0.25 \times 10^6$	-0.5	-20
	4	-0.25×10^6	-1×10^6	$+1.25 \times 10^6$	1.5	80
	5	$+0.25 \times 10^6$	-1.25×10^6	$+1 \times 10^6$	3	-80
	6	$+1.25 \times 10^6$	-0.25×10^6	-1×10^6	0.33	20
	7	$+1 \times 10^6$	$+0.25 \times 10^6$	-1.25×10^6	0.67	40

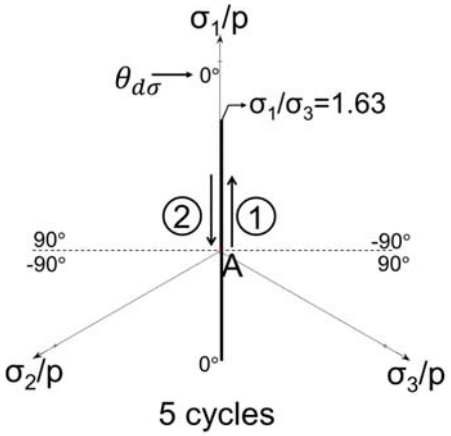

(a) Test 1

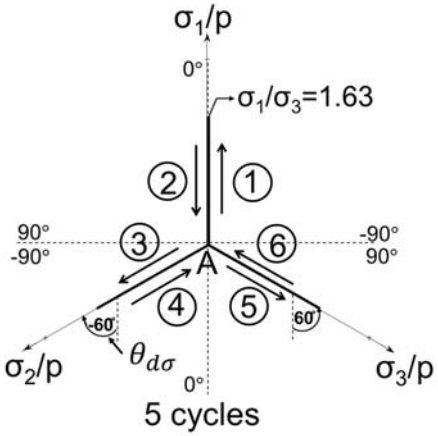

(b) Test 2

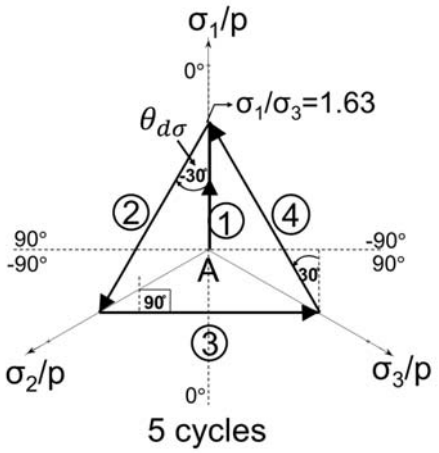

(c) Test 3

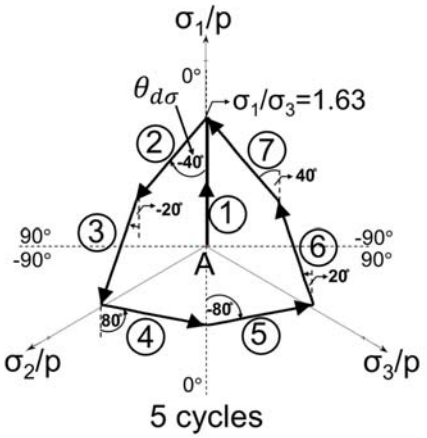

(d) Test 4

Fig. 6.3 Simulation program

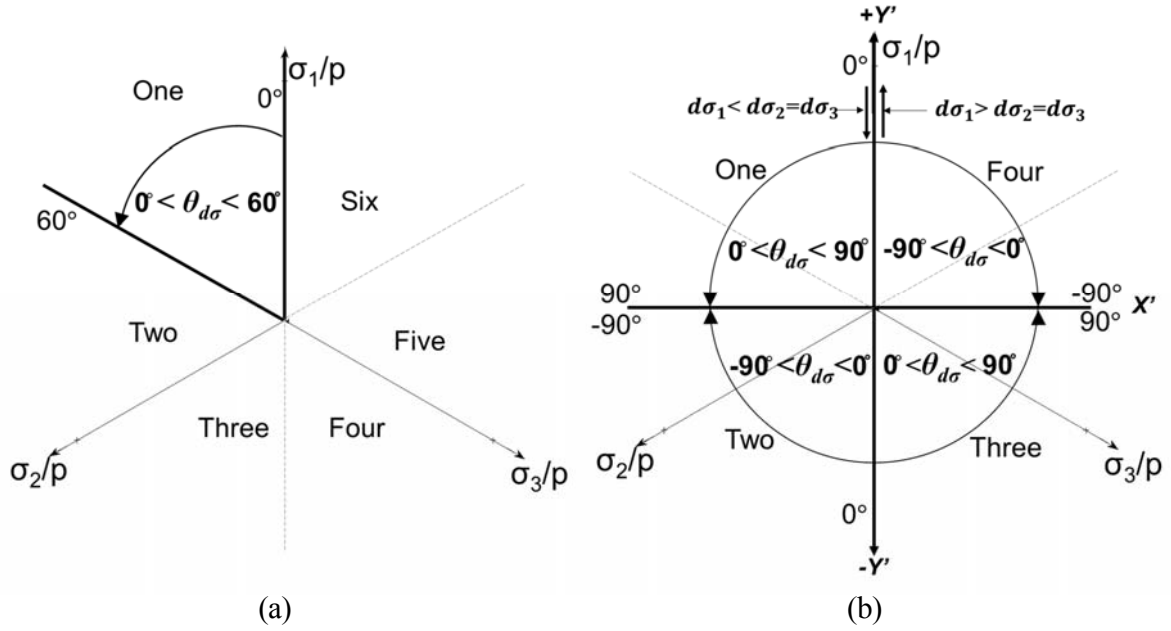

(a) (b)

Fig. 6.4 Direction of stress increment $\theta_{d\sigma}$ of: (a) one-sixth regions on the Π plane (after Suzuki & Yanagizawa, 2006); (b) all regions on the Π plane in this study.

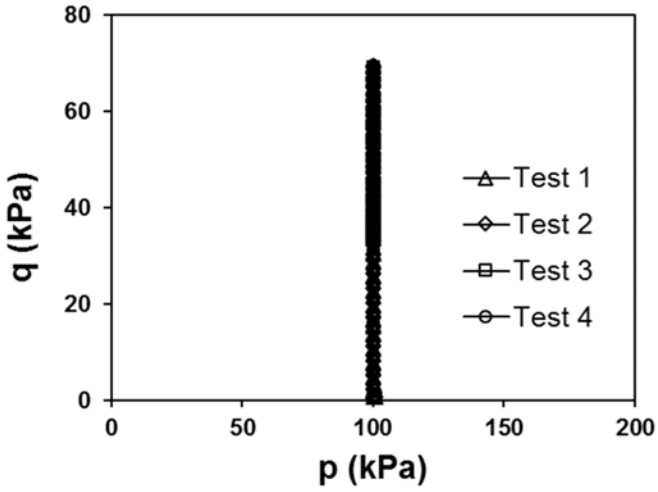

Fig. 6.5 *q-p* stress paths of all tests.

6.4 Results

6.4.1 Stress-Strain-Dilation

Figs. 6.6(a)-(d), 6.7(a)-(d), and 6.8(a)-(d) show the relationship of the stress ratio *q/p* versus the equivalent deviatoric strain ε_d (%), the normalized deviatoric stress $(\sigma_1 - \sigma_3)/p$ versus the deviatoric strain$(\varepsilon_1 - \varepsilon_3)$(%), the volumetric strain ε_v (%) versus the deviatoric strain $(\varepsilon_1 - \varepsilon_3)$ (%) and the volumetric strain ε_v (%) versus the stress ratio σ_1/σ_3 of Test 1 to Test 4, respectively.

In Figs. 6.7(a) and 6.8(a), the simulated stress-strain-dilation of Test 1 show generally observed from the experiments of triaxial compression and extension cyclic loading qualitatively (Tatsuoka & Ishihara 1974; Nakai et al., 2001; Wang 2005).

To validate the DEM results, the result of the volumetric strain ε_v(%) versus stress ratio σ_1/σ_3 on medium dense Toyoura sand (d_{50}=0.2mm, e_0=0.661, G_s=2.65, D_r = 73%) under drained triaxial compression and extension cyclic loading 5 cycles (similar stress path with Test 1) with stress amplitude σ_1/σ_3 = 3, constant mean stress p=196 kPa, and stress-controlled method by Nakai et al. (2001) is shown in Fig. 6.11. The Fig. shows that the volumetric strain ε_v shows a small dilation in the 1st loading stress. Then, a continuous compression is shown in the following cycles and become almost stable state after a few cycles (Nakai et al. 2001). Comparison between Fig. 6.8(a) and Fig. 6.10 indicate that the tendency of the numerical result of stress-strain-dilation is consistent with the experiment for a medium dense sand.

Figs. 6.6(a)-(d), 6.7(a)-(d), and 6.8(a)-(d) illustrate that the different cyclic stress paths shows the different relationships of the stress-strain-dilation. Furthermore in Figs. 6.7(a)-(d), the different cyclic stress paths also affects the width of cyclic loop. The stress path in Test 4 contributes wider cyclic loop of the stress-strain plot than the other tests (see Fig. 6.7(d)). The probable reason is that there is more energy dissipated in granular system under stress path of Test 4 than the other tests. Additionally, the cyclic stress path of Test 4 contains the high stress ratio continuously in 5 cycles (see Fig. 6.6(d)), which make the particles slide in a high degree

continuously, that dissipate the high degree of energy inside the granular system. The number of sliding particles in each test is explained later.

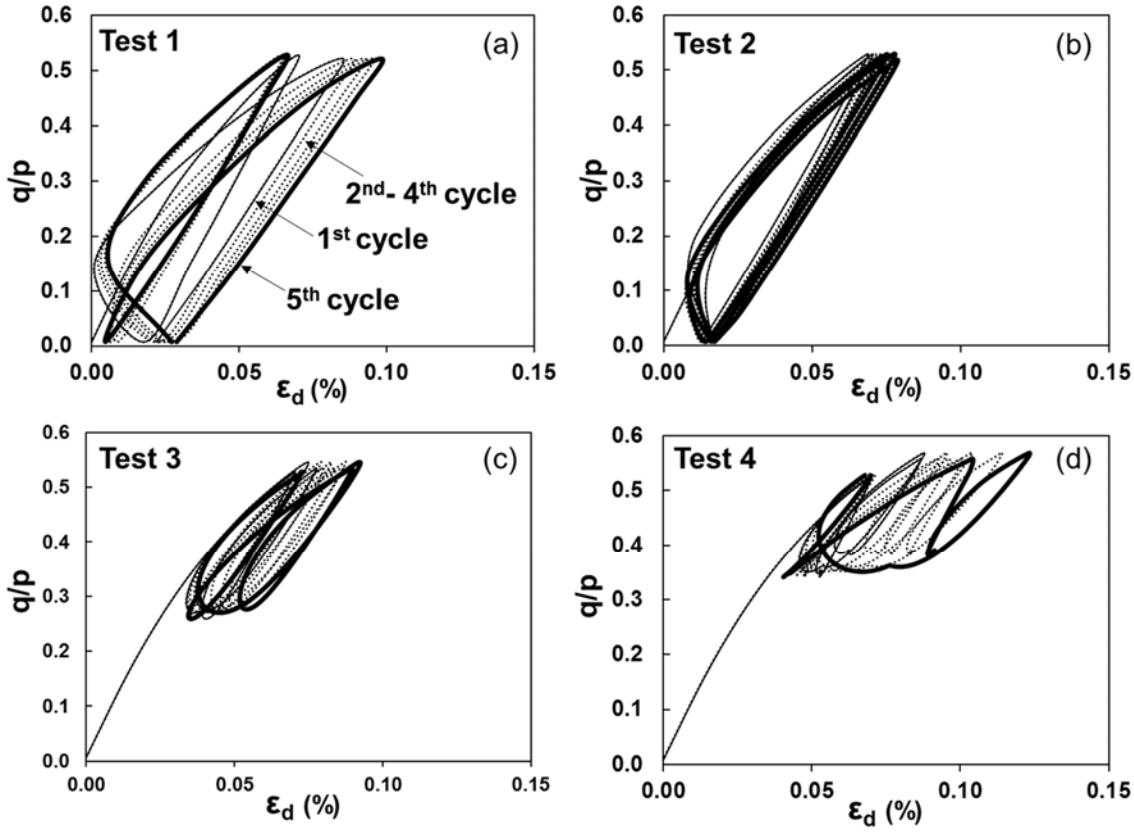

Fig. 6.6 Stress ratio *q/p* versus the equivaent deviatoric strain ε_d (%) of all tests.

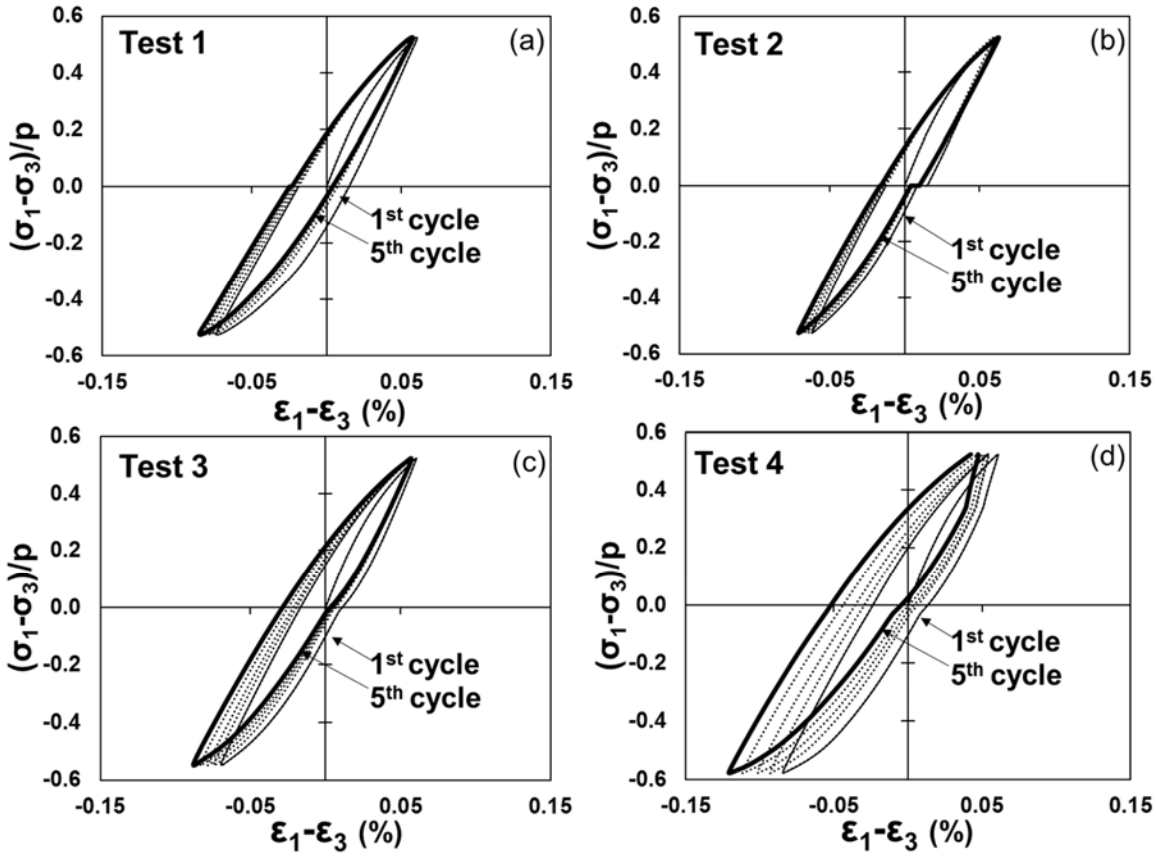

Fig. 6.7 Normalized deviatoric stress $(\sigma_1 - \sigma_3)/p$ versus the deviatoric strain $(\varepsilon_1 - \varepsilon_3)$ (%) of all tests.

It can be seen from Figs. 6.8(a)-(d) that the volumetric strain ε_v, indicated dilation characteristic, is influenced by the different cyclic stress paths, even though the maximum stress amplitudes of the stress path given in each test are the same ($\sigma_1/\sigma_3 = 1.63$). Furthermore in Fig. 6.8(d), Test 4 shows more effect in the extension side of the deviatoric strain $(\varepsilon_1 - \varepsilon_3)$(%). This result indicates that the deviatoric strain is strong enough on the compression side to resist the cyclic stress, but it accumulates in the extension side. This result is similar to the result of Sitharam (2003) using DEM under the cyclic compression and extension loading using stress controlled method with 2-dimentional disc assemblage.

Fig. 6.9 shows all stress paths on one Π plane and the approximate failure surface. The Fig. shows that most of the parts of cyclic stress paths of Test 1, 2, and 3 is contained in the stress

path of Test 4 which close to the approximate failure surface more than the other tests. We can also say from Fig. 6.9 that Test 4 has more unconventional cyclic stress path than the other tests because of the more change of the stress directions. The degree of the distance from the failure surface and the degree of unconventional cyclic loading may probable reason of the deviatoric strain in the extension side and the volume expansion. The unconventional cyclic loading causing volume expansion of sand was reported by Nakai et al. (1996) using the experimental results of sand under eccentric cyclic loadings with various stress amplitudes.

We can concluded that stress-strain-dilation depends not only on the characteristic of cyclic stress paths but also on the stress amplitudes as well as on how close the failure surface of those stress paths is.

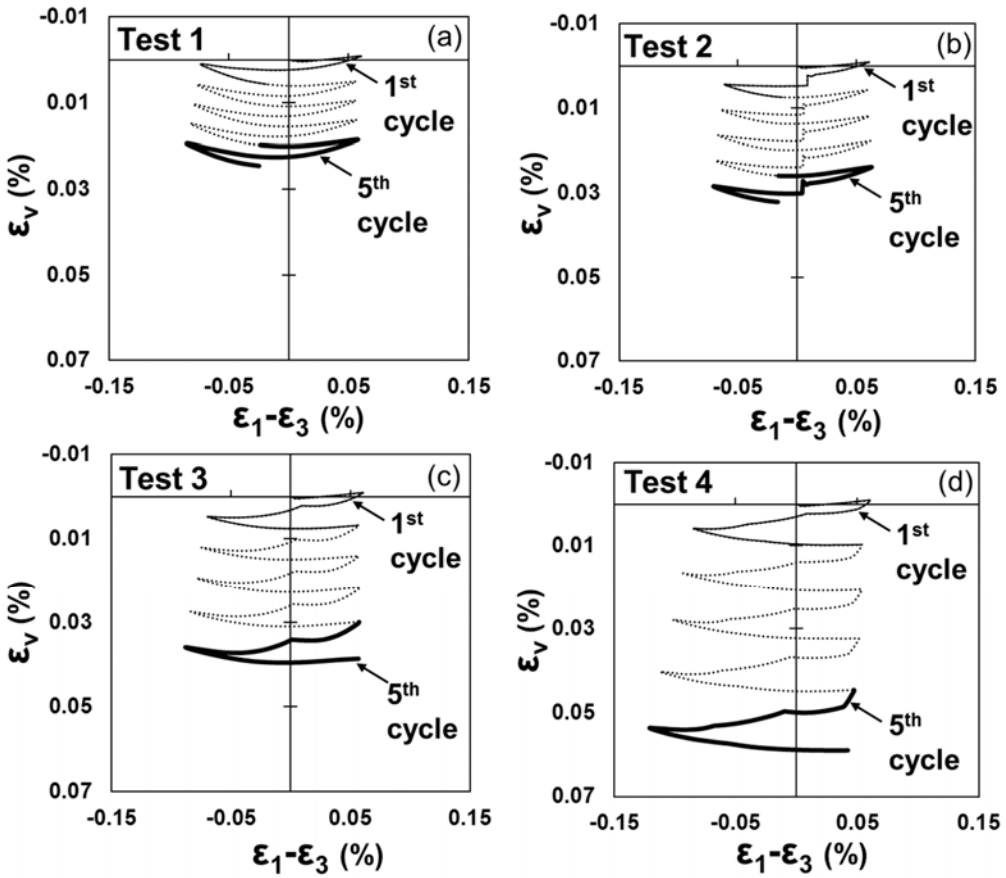

Fig. 6.8 Volumetric strain ε_v (%) versus the deviatoric strain $(\varepsilon_1 - \varepsilon_3)$ (%) of all tests.

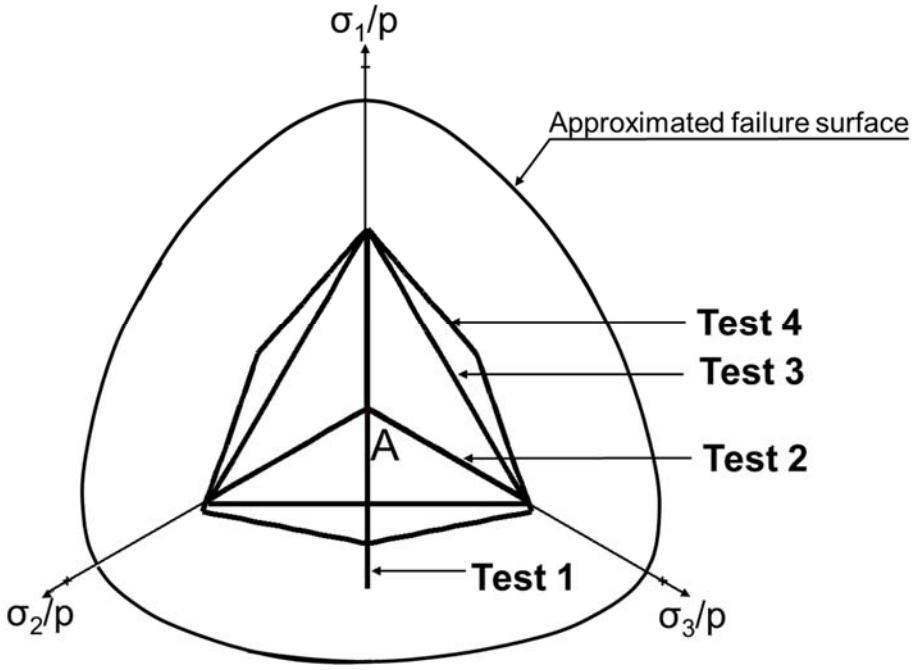

Fig. 6.9 All four cyclic stress paths containing on one Π plane.

6.5.2 Direction of Principal Strain Increment Vectors

The directions of the 1st and the 5th cycle of the principal strain increment vectors superimpose on the stress path on the normalized Π plane of Test 1 to Test 4 are shown from Figs. 6.10(a)-(d), respectively. It can clearly be seen that the direction of the principal strain increment vectors depends very much on the direction of the stress path. However, it is not influenced by the number of cycles. This conclusion was reported before by Nakai et al. (2003) using the experimental results of the medium dense Toyoura sand under cyclic loading tests.

In Fig. 6.11(a), the 1st cycle of the principal strain increment vectors superimpose on the stress path of Test 4 is shown with those of the stress path **ABC** (the maximum $\sigma_1/\sigma_3 = 2.28$) and with those of the failure surface (the maximum $\sigma_1/\sigma_3 = 2.68$). This failure surface and its strain

increment vectors was created by the five stress paths of constant b values (b = 0, 0.3, 0.5, 0.7, and 1) where $b = (\sigma_2 - \sigma_3)/(\sigma_1 - \sigma_3)$ (Habib, 1953) following the simulation method of Phusing et al. (2015). For qualitative comparison, the experimental result of the medium Toyoura dense sand under cyclic loading tests of Nakai et al. (2003) is shown in Fig. 6.11(b). We can see from Figs. 6.11(a) and 6.11(b) that the simulated directions of the principal strain increment vectors show better consistency between the experiment under stress path **bc** (Fig. 6.11(b)), and the DEM results under stress path **BC** (Fig. 6.11(a)). It can be noted that the direction of the principal strain increment vectors depends on not only the stress path, but also on the stress amplitude and the degree of the distance from the failure surface. The dependency of the degree of the distance from the failure surface to the directions of the principal strain increment vector was reported before by Phusing et al. (2015)using DEM with monotonic loading simulations.

6.5.4 Micromechanical Response

One objective of the study is to clarify the micromechanical response of granular materials. DEM simulation has been used to investigate the micromechanical response of granular materials under cyclic loading tests. For instance, Sitharam (2003) simulated the micromechanical behavior of granular materials under stress controlled method and constant mean stress on an assembly of loose, medium dense and dense systems using DEM. The study showed that the DEM can simulate the cyclic behavior of sands very adequately. It also showed that, medium dense sample is liquefied due to the continuous loss of coordination number and reorientation of fabric in the reversal of cyclic loading.

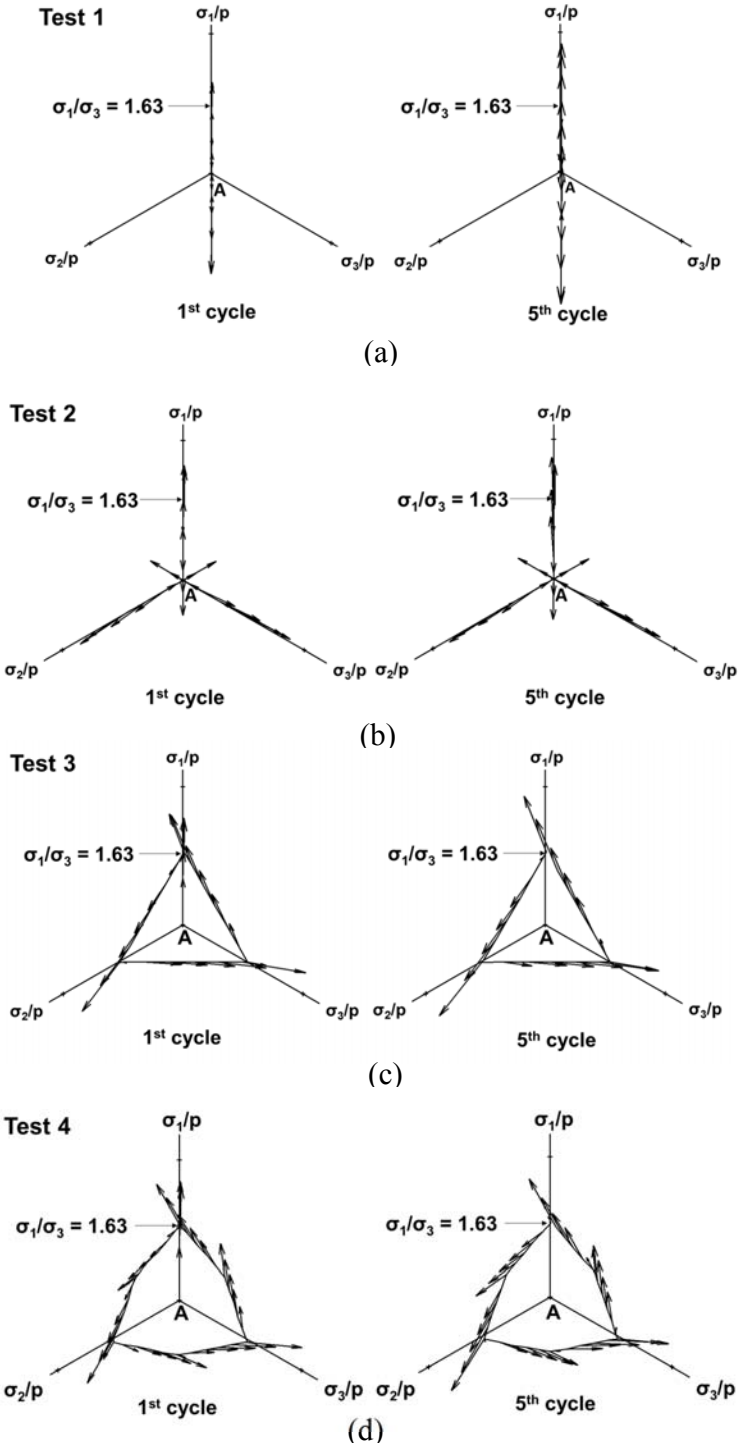

Fig. 6.10 Directions of principal strain increment vectors of the 1st and 5th cycle superimposed on the stress paths of Test 1 to 4.

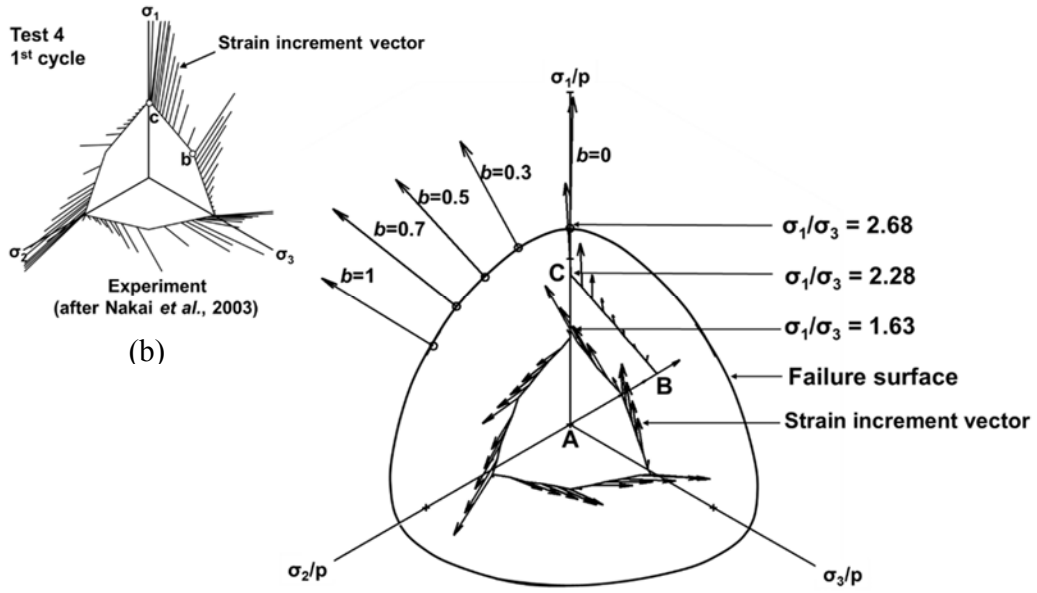

Fig. 6.11 Directions of strain increment vectors of: (a) the 1st cycle of Test 4, stress path **ABC** and the failure surface; (b) the experiment of medium dense sand under cyclic loading (after Nakai et al. 2003)

Fig. 6.12(a) shows the enlargement of Fig. 6.8(a) which is the result of the triaxial compression and extension of cyclic stress path Test 1. Figs. 6.12(a)- (c) include plots of the volumetric strain ε_v (%) versus deviatoric strain $(\varepsilon_1 - \varepsilon_3)$ (%) (Fig. 6.12(a)), corresponding with the coordination number (Fig. 6.12(b)), and sliding contact fraction (%) (Fig. 6.14(c)) of all 5 cycles, respectively. In Fig. 6.12(a), the annotations "dilate" means the sample dilates comparing with the previous loading while "comp." means the sample compresses. For example, in Fig. 6.12(a), the sample dilates at point **2** comparing with **1** which is a short period consideration. However, the overall the samples undergo overall compression. Figs. 6.12(a) and 6.12(b) show that the coordination number decreases with the dilation of the volumetric strain,

and increases with the compression. The similar result was reported by Sitharam (2003) simulating a medium dense sample using DEM. In Fig. 6.12(c), the sliding contact fraction shows increases with the dilation and a sudden drop when changing the direction of the stress path from loading to unloading, for example, at point **3** in Figs. 6.12(a)- (c). The reason of the sudden drop is that some sliding particles under the loading direction were stop sliding because the loading direction is removed. Later, they start to slide again because of the new direction of loading.

Figs. 6.13(a) and 6.13(b) show the relationships between the coordination number and the sliding contact fraction at the end of each cycle of all tests. The figures show that the coordination number decreases with increasing the number of cycles whereas the sliding contact fraction seeming remains constant. Furthermore in the figures, the stress path of Test 4 gives the minimum coordination number and the maximum sliding contact fraction with increasing the number of cycles. This explains that the stress path of Test 4, containing continuously high stress ratios, forces the granular materials to lose their normal contacts and to produce sliding contacts more than in the other tests.

6.5.4 Macro-Micro Relationship

The relationship between the macro behavior and micromechanical data under cyclic loadings with various stress amplitudes is one of the objectives of this study. The studies on the macro-micro relationship were performed by several approaches. Thornton and Antony (1998) using 2-dimentional simulation reported the compression and extension simulations on a soft particle system and found that shear strength was mainly due to strong force network and the weak network's contribution to shear strength was very small. Ng (2004) also used 2-dimentional simulation and showed that the principal stress ratio σ_1/σ_3 correlates with the contact normal force more than with the unit contact normal force under different stress paths. In this study, the correlation between the macro-scale, represented by the stress ratio q/p, and a single parameter, related to the contact normal vector, is used to describe the macro-micro relationship (Antony

et al. 2004; Sazzad et al. 2011). The contact normal vectors are represented by all contacts in major, intermediate, and minor directions (F_{11}, F_{22}, and F_{33}, respectively) and by the strong contacts (F_{11}^{s}, F_{22}^{s}, and F_{33}^{s}, respectively).

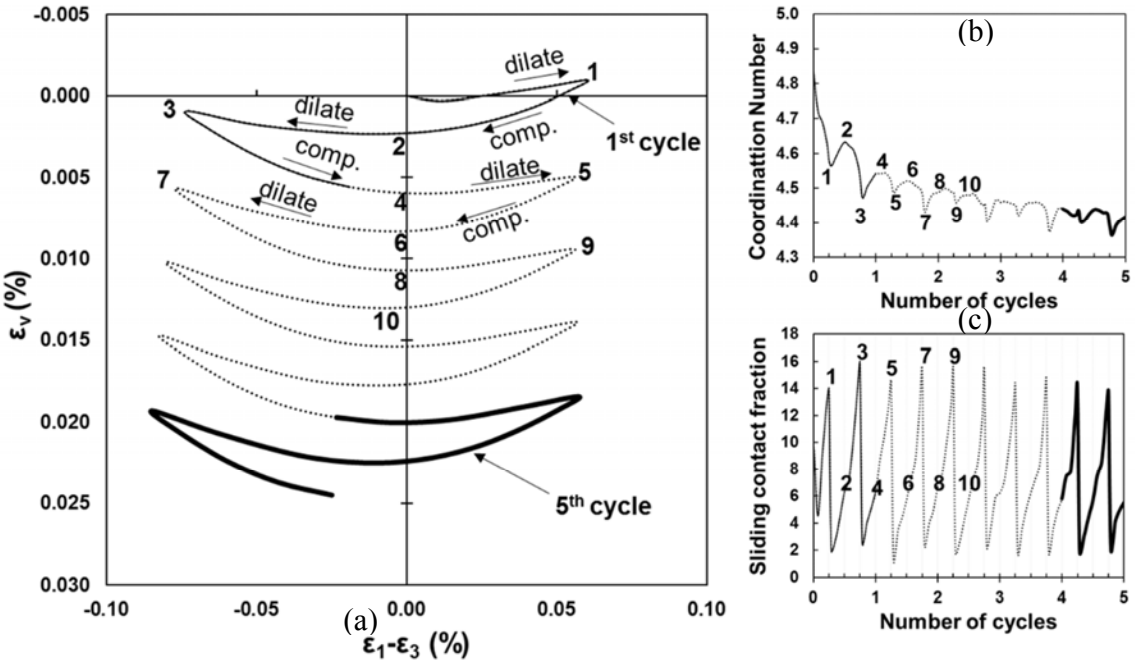

Fig. 6.12 Results of Test 1: (a) ε_v (%) versus $(\varepsilon_1 - \varepsilon_3)$ (%); (b) coordination number versus number of cycles; (c) sliding contact fraction (%) versus number of cycles.

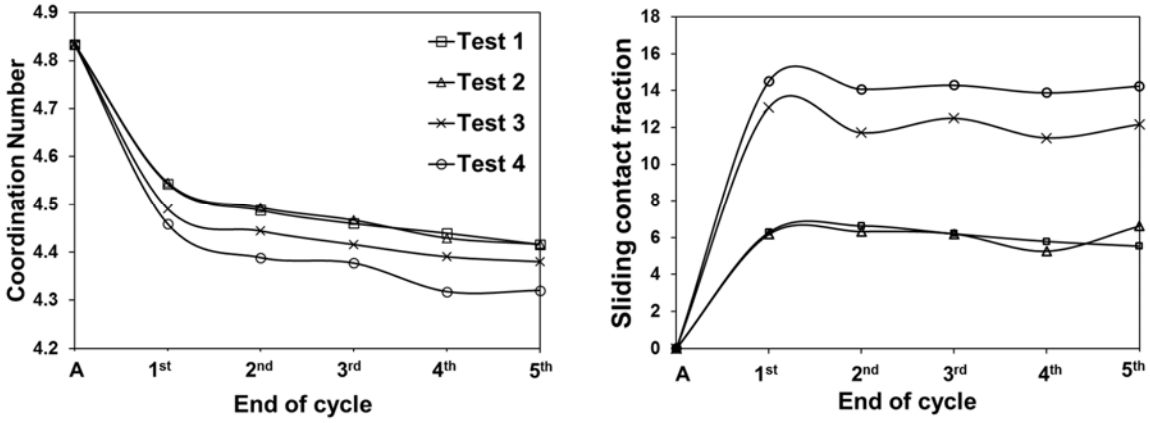

Fig. 6.13 Results of all tests: (a) Coordinate number at the end of each cycle; (b) sliding contact fraction at the end of each cycle.

Figs. 6.14(a)- (d) and 6.15(a)- (d) present the macro-micro relationship of 5 cycles between the macro behavior, indicated by stress ratio *q/p,* and the micromechanical response, indicated by the deviatoric fabrics ratio of all contacts F_d/F_m and of strong contacts F_d^s/F_m^s, respectively. F_d and F_d^s are the equivalent deviatoric fabrics of all contacts and of strong contacts (see Eq. 2.7 and 2.8). F_{m} and F_m^s is are the mean fabrics of all contacts and of strong contacts (see Eq. 2.9 and 2.10). In Figs. 6.14(a)-(d) and 6.15(a)-(d), the coefficient of determination or R-squared value is used to show the uniqueness of the macro-micro relationship. Figs. 6.14(a)-(d) show that R-squared values of the macro-micro relationship of all tests are different when considering all contacts, however, they show almost similar values when considering strong contacts in Figs. 6.15(a)-(d). Therefore, the uniqueness of the macro-micro relationship is shown when considering only strong contacts. Furthermore, this uniqueness is independent on the degree of the unconventional cyclic stress paths and on the number of cycles. The linking between the macro behavior and the micro responses shows in this study may lead to develop micromechanical parameters for constitutive models in the future study.

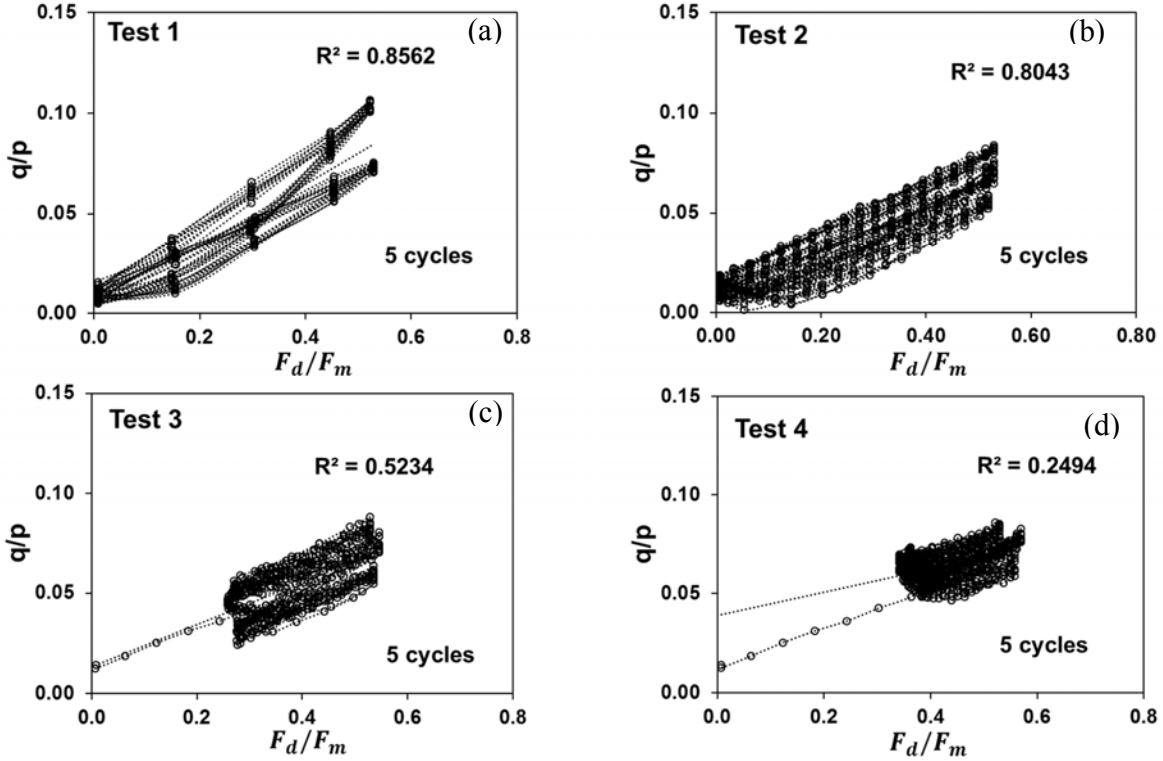

Fig. 6.14 Macro-micro relationship between stress ratio *q/p,* and the deviatoric fabrics ratio of all contacts $\boldsymbol{F_d/F_m}$.

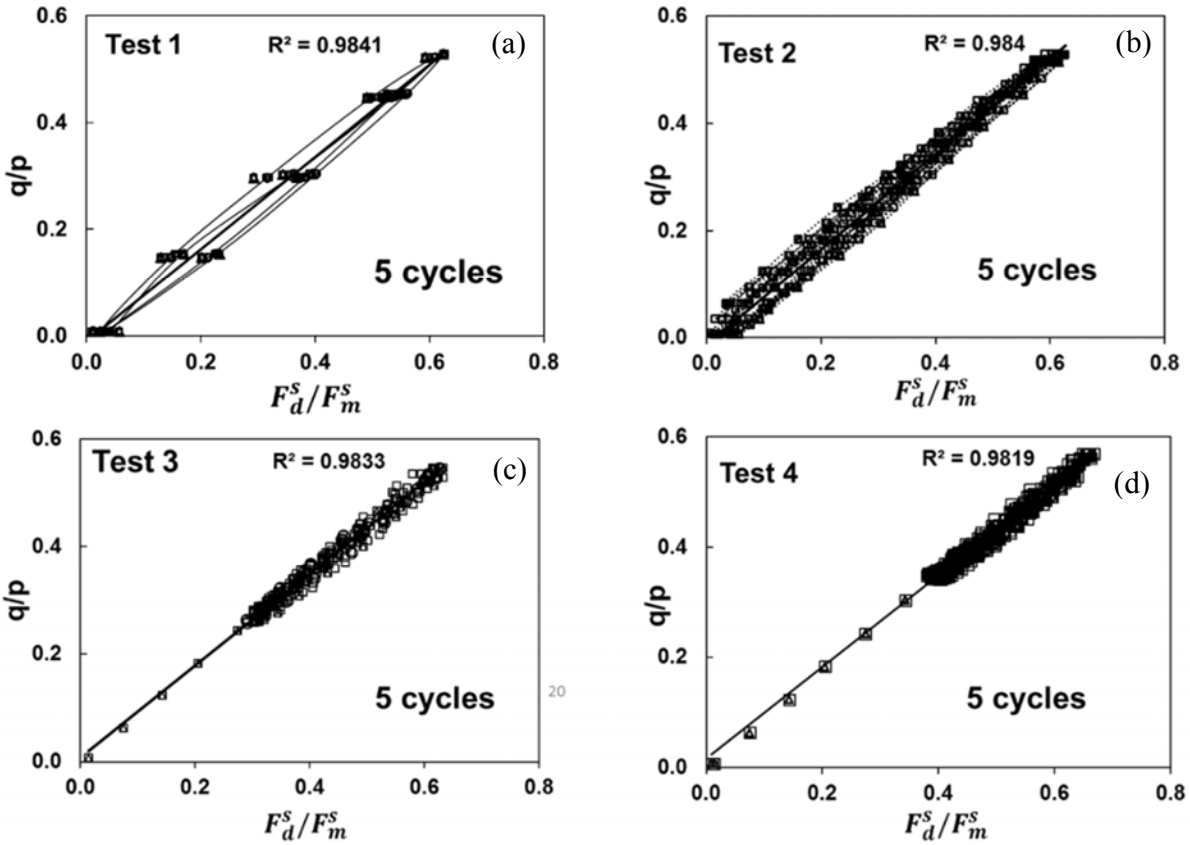

Fig. 6.15 Macro-micro relationship between stress ratio *q/p,* and the deviatoric fabrics ratio of strong contacts F_d^s/F_m^s.

Chapter 7 Conclusions and Recommendations

7.1 Introduction

Mechanical behaviors of granular materials were evaluated under generalized stress conditions specified by continuously varying *b* values using the Discrete Element Method (DEM). Specifically, the true triaxial simulations under constant *b* and continuously varying *b* were conducted using the DEM. Some differences in evolution of stress-strain relationships, including the relationship between principal normal strains, principal deviatoric strains, and evolution of stress and strain increment vectors under more generalized states of stress were carried on. Below is some conclusions.

7.2 Conclusions

This research focused on the mechanical behavior of granular materials under generalized stress system where the major, intermediate and minor principal stresses σ_1, σ_2 and σ_3 change continuously. The influence of intermediate stress ratio, specified by the *b* value [= $(\sigma_2-\sigma_3)/(\sigma_1-\sigma_3)$] (Habib 1953), is a key parameter in this research. The granular materials under constant *b* value stress paths have been studied in several researches. This study analyzes the granular materials under continuously varying *b* value stress paths. So, the stress path can change the direction at any place on the π-plane. The macro behaviors and micro data have been explored. Discrete Element Method (DEM), known as a powerful method for studying granular materials, was used in this study. Based on the results in the dissertation, further summaries are as followed described.

- The direction of stress increment vector $\theta_{d\sigma}$ and strain increment vector $\theta_{d\varepsilon}$ as well as stress-dilatancy results obtained from the DEM simulations qualitatively show good consistencies with the experimental data found in the literature on true triaxial tests under generalized stress conditions, defined by continuously varying b values. It was seen that modeling features available in DEM simulations are quite powerful in capturing both micro and macro behavior of granular materials.

- The DEM results showed that the shearing resistance angle ϕ is independent of the stress paths (i.e., not influenced by b values).

- The DEM results showed that the direction of strain increment $\theta_{d\varepsilon}$ is not only dependent on the direction of stress increment $\theta_{d\sigma}$ but also on the approximate failure surface.

- The direction of strain increment vector $\theta_{d\varepsilon}$ is influenced by the intermediate stress ratio of b, under continuously varying b test. The immediate change in the direction of strain increment vector occurs when the stress increment changes direction.

- The sliding contact fraction changes rapidly when the direction of stress increment changes under continuously varying b tests, indicating that the direction of stress path influences the sliding contact fraction.

- The relationships between macro (defined by stress ratio q/p) and micro (defined by deviatoric fabric tensor) behavior were consistent for both constant b tests and continuously varying b tests. In both cases, consistent relationship between macro and micro behaviors was found when considering only in the strong contacts (defined by deviatoric strong fabric tensor).

Further study in this research was related to the micro data. The mechanical behavior of granular materials was evaluated under more generalized stress conditions with five constant and three continuously varying b values. The assembly of sphere under 3-dimentional principal stresses of various stress paths was conducted under the constant mean stress and the stress-controlled method. The macro behaviors of granular materials using the stress-strain-dilation relationship was described. The micromechanical parameters consists of contact normals (fabric), normal contact forces, and tangential contact forces a_{ij}^{r}, a_{ij}^{n} and a_{ij}^{t}. They were evaluated. Their significance to the macro behaviors regarding the varying b value was explained as well. Main findings can be summarized for an initial isotropic material using sphere particles as follows:

- At peak, both the distributions and the degree of anisotropy of contact normal (fabric), normal contact forces, and tangential contact forces do not depend on the stress path.
- The increment vectors of contact normal (fabric), normal contact forces, and tangential contact forces depend on the location of stress paths as well as the degree of changing directions of those stress paths under constant and continuously varying b value stress paths.
- Changing the direction of stress paths causes not only changing the direction of maximum stress but also changing the incremental vectors of contact normal (fabric), normal contact forces, and tangential contact forces.

This research further studied the behavior of granular materials under more generalized cyclic loading tests. The more generalized cyclic stress condition in this study is identified as the unconventional cyclic loading with various stress amplitudes in 3-dimentional directions of principal stresses. Five different characteristics of cyclic shapes have been set. Cyclic loading simulations were conducted under constant mean stress and stress-controlled method. Here explained the macro behaviors of granular materials using the stress-strain-

dilation relationship and the directions of principal strain increment vectors and the micromechanical response as well as the macro-micro relationship were explained. Main findings can be described below.

- The direction of principal strain increment vectors from DEM results shows good consistency with the actual behavior of sand under cyclic loading in more generalized stress condition.

- The direction of the principal strain increment vectors depends on not only the stress path, but also on the stress amplitude and the degree of the distance of that stress path from the failure surface. However, it is not influenced by the number of cycles.

- DEM result shows that the more unconventional cyclic stress path with a continuously high degree of stress amplitude is applied, the more effect of volumetric strain in the extension side and volume expansion.

- This unique macro-micro relationship does not depend on the more generalized cyclic stress paths, and on the number of cycles.

7.3 Recommendations

To increase knowledge in the behavior of granular materials in geotechnical engineering, the following are some suggestions for further researches.

- To explore the fabric distributions and contact force diagrams of granular materials under cyclic loading tests in general stress systems.

- To study the effect of shapes of granular materials (e.g. ellipsoids, bumpy particles) under continuously varying b value stress paths and compare their micromechanical behaviors.

- To study the mechanical behaviors of granular materials having a cross anisotropy under continuously varying *b* value stress paths.
- To study macro and micro behaviors of granular materials under undrained tests and continuously varying *b* value stress paths.

References

Antony, S. J., Momoh, R. O., and Kuhn, M. R. (2004). "Micromechanical modelling of oval particulates subjected to bi-axial compression." *Comput. Mater. Sci.,* 29(4), 494–498.

Barreto, D., and O'Sullivan, C. (2012). "The influence of inter-particle friction and the intermediate stress ratio on soil response under generalised stress conditions." *Granular Matter*, 14(4), 505–521.

Bathurst, R. J. (1985). "A study of stress and anisotropy in idealized granular assemblies." Ph.D. Thesis, Queen's University, Kingston, Canada.

Chantawarangul, K. (1993). "Numerical simulations of three dimensional granular assemblies." Ph.D. Thesis, University of Waterloo, Waterloo, Ontario, Canada.

Cundall, P. A., and Strack, O. D. L. (1979). "A discrete numerical model for granular assemblies." *Géotechnique*, 29(1), 47–65.

Cundall, P. A., and Strack, O. D. L. (1983). "Modeling of microscopic mechanisms in granular material." *Studies in Applied Mechanics*, Mechanics of Granular Materials New Models and Constitutive Relations, M. Satake and J. T. Jenkins, eds., Elsevier, Amsterdam, 137–149.

Dantu, P. (1957). "Contribution à l'étude mécanique et géométrique des milieux pulvérulents." *Proc. of the 4th Int. Conf. on Soil Mech. and Found. Eng.*, London, 144–148.

Ergun, M. U. (1981). "Evaluation of three-dimensional shear testing." *Soil Mechanics and Foundation Engineering, Tenth International Conference: Proceedings of the Tenth International Conference on Soil Mechanics and Foundation Engineering, Stockholm 15-19 June 1981*, Balkema, 593–596.

Green, G. E., and Bishop, A. W. (1969). "A note on the drained strength of sand under generalized strain conditions." *Géotechnique*, 19(1), 144–149.

De Josselin de Jong, G. (1969). “Etude photo elastique d’un empilement de disques.” *Cahiers du Groupe Française de Rhéologie*, 2, 73–86.

Ko, H.-Y., and Scott, R. F. (1967). “A new Soil Testing Apparatus.” *Géotechnique*, 17(1), 40–57.

Konishi, J., Oda, M., and Nemat-Nasser, S. (1983). “Induced anisotropy in assemblies of oval cross-section rod in biaxial compression.” *Mechanics of Granular Materials: New Models and Constitutive Relations*, J. T. Jenkins and M. Satake, eds., Elsevier, Amsterdam, 31–39.

Kruyt, N. P., and Rothenburg, L. (2006). “Shear strength, dilatancy, energy and dissipation in quasi-static deformation of granular materials.” *J. Stat. Mech.*, 2006(07), P07021.

Kuhn, M. R. (1999). “Structured deformation in granular materials.” *Mech. Mater.*, 31(6), 407–429.

Kuhn, M. R. (2006). “OVAL and OVALPLOT: Programs for analyzing dense particle assemblies with the discrete element method.” <http://faculty.up.edu/kuhn/oval/doc/oval_0618.pdf> (May 12, 2015).

Kumruzzaman, M., and Yin, J.-H. (2012). “Influence of the intermediate principal stress on the stress–strain–strength behaviour of a completely decomposed granite soil.” *Géotechnique*, 62(3), 275–280.

Lade, P. V. (2006). “Assessment of test data for selection of 3-D failure criterion for sand.” *Int. J. Numer. Anal. Meth. Geomech.*, 30(4), 307–333.

Lade, P. V., and Duncan, J. M. (1973). “Cubical Triaxial Tests on Cohesionless Soil.” *J. Soil Mech. Found. Div. ASCE*, 99(10), 793–812.

Lade, P. V., and Duncan, J. M. (1975). “Elastoplastic stress-strain theory for cohesionless soil.” *Journal of the Geotechnical Engineering Division*, 101(10), 1037–1053.

Madhusudhan, B. N., and Kumar, J. (2010). "Effect of relative density and confining pressure on Poisson ratio from bender and extender elements tests." *Géotechnique*, 60(7), 561–567.

Matsuoka, H., and Nakai, T. (1978). "A generalized frictional law of soil shear deformation." *Proc., U.S.-Japan Seminar on Continuum-Mechanical and Statistical Approaches in Mechanics of Granular Materials*, Tokyo, 138–154.

Matsuoka, H., and Sun, D. (1995). "Extension of spatially mobilized plane (SMP) to frictional and cohesive materials and its application to cemented sands." *Soils Found.*, 35(4), 63–72.

Nakai, T., Korenaga, Y., Hinokio, M., and Nagai, H. (2003). "Shear behavior of sand under cyclic loading in general stress systems." *Deformation Characteristics of Geomaterials / Comportement Des Sols Et Des Roches Tendres*, Taylor & Francis, 1087–1094.

Ng, T.-T. (2005). "Behavior of gravity deposited granular material under different stress paths." *Can. Geotech. J.*, 42(6), 1644–1655.

Ng, T.-T. (2006). "Input parameters of discrete element methods." *J. Eng. Mech.*, 132(7), 723–729.

Oda, M., Koishikawa, I., and Higuchi, T. (1978). "Experimental study of anisotropic shear strength of sand by plane strain test." *Soils Found.*, 18(1), 25–38.

Oda, M., and Konishi, J. (1974). "Microscopic deformation mechanism of granular material in simple shear test." *Soils Found.*, 14(4), 25–38.

Oger, L., Savage, S. B., Corriveau, D., and Sayed, M. (1998). "Yield and deformation of an assembly of disks subjected to a deviatoric stress loading." *Mech. Mater.*, 27(4), 189–210.

O'Sullivan, C., and Bray, J. D. (2004). "Selecting a suitable time step for discrete element simulations that use the central difference time integration scheme." *Eng. Comput.*, 21(2/3/4), 278–303.

Phusing, D., and Suzuki, K. (2015). “Cyclic behaviors of granular materials under generalized stress condition using DEM.” *J. Eng. Mech.*, 04015034:1–12.

Phusing, D., Suzuki, K., and Zaman, M. (2015). “Mechanical Behavior of Granular Materials under Continuously Varying b Values Using DEM.” *International Journal of Geomechanics*, 04015027.

Procter, D. C., and Barton, R. R. (1974). “Measurements of the angle of interparticle friction.” *Géotechnique*, 24(4), 581–604.

Rodriguez, N., and Lade, P. (2013). “True Triaxial Tests on Cross-Anisotropic Deposits of Fine Nevada Sand.” *Int. J. Geomech.*, 13(6), 779–793.

Roscoe, K. H., Schofield, A. N., and Wroth, C. P. (1958). “On the yielding of soils.” *Géotechnique*, 8(1), 22–53.

Rothenburg, L. (1980). “Micromechanics of idealized granular systems.” Ph.D. Thesis, Carleton University, Ottawa,. Ontario, Canada.

Rothenburg, L., and Bathurst, R. J. (1989). “Analytical study of induced anisotropy in idealized granular materials.” *Géotechnique*, 39(4), 601–614.

Rothenburg, L., and Bathurst, R. J. (1992). “Micromechanical features of granular assemblies with planar elliptical particles.” *Geotechnique*, 42(1), 79–95.

Rothenburg, L., and Kruyt, N. P. (2004). “Critical state and evolution of coordination number in simulated granular materials.” *Int. J. Solids and Struct.*, Granular Mechanics, 41(21), 5763–5774.

Salot, C., Gotteland, P., and Villard, P. (2009). “Influence of relative density on granular materials behavior: DEM simulations of triaxial tests.” *Granular Matter*, 11(4), 221–236.

Sazzad, M. (2011). “Numerical study on macro and micro mechanical behavior of granular materials using DEM.” Ph.D. Thesis, Saitama University, Saitama, Japan.

Sazzad, M. M., and Suzuki, K. (2013). “Density dependent macro-micro behavior of granular materials in general triaxial loading for varying intermediate principal stress using DEM.” *Granular Matter*, 15(5), 583–593.

Sazzad, M., and Suzuki, K. (2011). “Effect of Interparticle Friction on the Cyclic Behavior of Granular Materials Using 2D DEM.” *Journal of Geotechnical and Geoenvironmental Engineering*, 137(5), 545–549.

Sazzad, M., Suzuki, K., and Modaressi-Farahmand-Razavi, A. (2012). “Macro-Micro Responses of Granular Materials under Different b Values Using DEM.” *Int. J. Geomech.*, 12(3), 220–228.

Sitharam, T. G. (2003). “Discrete element modelling of cyclic behaviour of granular materials.” *Geotech. Geolog. Engng*, 21(4), 297–329.

Sitharam, T. G., Dinesh, S. V., and Srinivasa Murthy, B. R. (2004). “Critical state behaviour of granular materials using three dimensional discrete element modelling.” *Granular materials: fundamentals and applications*, S. J. Antony, W. Hoyle, and Y. Ding, eds., RSC, London, 135–156.

Skinner, A. E. (1969). “A note on the influence of interparticle friction on the shearing strength of a random assembly of spherical particles.” *Geotechnique*, 19(1), 150–157.

Suiker, A. S. J., and Fleck, N. A. (2004). “Frictional collapse of granular assemblies.” *J. Appl. Mech.*, 71(3), 350–358.

Sun, D., Huang, W., and Yao, Y. (2008). “An experimental study of failure and softening in sand under three-dimensional stress condition.” *Granular Matter*, 10(3), 187–195.

Suzuki, K., and Yanagisawa, E. (2006). “Principal deviatoric strain increment ratios for sand having inherent transverse isotropy.” *Int. J. Geomech.*, 6(5), 356–366.

Thornton, C. (2000). “Numerical simulations of deviatoric shear deformation of granular media.” *Géotechnique*, 50(1), 43–53.

Thornton, D. C., and Barnes, D. D. J. (1986). “Computer simulated deformation of compact granular assemblies.” *Acta Mechanica*, 64(1-2), 45–61.

Tu, X., and Andrade, J. E. (2008). “Criteria for static equilibrium in particulate mechanics computations.” *Int. J. Numer. Meth. Engng.*, 75(13), 1581–1606.

Wang, Q., and Lade, P. V. (2001). “Shear banding in true triaxial tests and its effect on failure in sand.” *J. Eng. Mech.*, 127(8), 754–761.

Yamada, Y., and Ishihara, K. (1979). “Anisotropic deformation characteristics of sand under three dimensional stress conditions.” *Soils Found.*, 19(2), 79–94.

Zhang, Y., Deng, S., Le, V., and Sun, y. (2014). “Micro-mechanism of the intermediate principal stress effect on the strength of granular materials.” *Soil Behavior and Geomechanics*, ASCE, 465–475.